PHOTONEUTRON STUDIES IN MEDIUM-WEIGHT ELEMENTS

A thesis submitted to
The Australian National University
for the degree of

Doctor of Philosophy

by

Graeme Ernest Coote

October, 1961.

PREFACE

The experiments described in this thesis were carried out on the 1.2 MeV Cockcroft-Walton set and the 33 MeV electron synchrotron of the Australian National University.

The experiment described in chapter 2 was carried out jointly with Mr. I. F. Wright, and that of chapter 3 with Mr. Wright and Dr. W. E. Turchinetz, with the work shared equally in each case. The isomer experiment of chapter 5 was performed jointly with Dr. J. H. Carver, though most of the experimental work and data analysis was done by myself. Mr. T. R. Sherwood assisted with some of the early experimental work and analyzed some of the decay curves. The gallium experiment of chapter 4 was done independently.

The experiments of chapter 2 and 3 were described in the following paper:

"Cross Sections for the (γ,n) reaction in Cu^{63}, Cu^{65}, Zn^{64}, Sb^{121} and Pr^{141}, measured with monochromatic gamma rays"
G. E. Coote, W. E. Turchinetz and I. F. Wright,
Nuclear Physics 23, 468, 1961

Two papers on the experiments of chapter 4 and chapter 5 are in preparation.

No part of this thesis has been submitted for a degree at any other university.

G. E. Coote

ACKNOWLEDGEMENTS

Many people gave practical help or advice during the course of this work but I wish to single out those mentioned below.

Mr. N. F. Bowkett gave excellent service in maintenance of the H.T. set and associated equipment, and Mr. J. Gower did the same for the electron-synchrotron.

Mr. M. J. Vernon carried out several chemical operations and made some radioactive sources.

In the maintenance of electronic equipment, Mr. Dick Graf was particularly long-suffering and patient.

Mr. I. V. Mitchell gave valuable assistance with recalibration and operation of the synchrotron at a critical stage of the work.

I am grateful to Dr. J. H. Carver, who gave helpful advice during work on the synchrotron and on preparation of a paper for publication. Useful discussions on recent developments in photonuclear theory were held with Dr. D. C. Peaslee, and Professor K. J. Le Couteur gave valuable advice on interpretation of experimental results.

The work was carried out during the tenure of a Research Scholarship, awarded by the Australian National University.

PHOTONEUTRON STUDIES IN MEDIUM-WEIGHT ELEMENTS

SUMMARY

This thesis describes four experiments on photoneutron reactions in medium-weight nuclei, the first two carried out with gamma radiation from (p,γ) reactions and the third and fourth with bremsstrahlung from a 33 MeV electron synchrotron.

In chapter 1 is presented a brief review of photonuclear reactions in the giant resonance region. Discussion is mainly devoted to photon absorption, models for the giant resonance and decay of the excited nucleus. Recent developments in photonuclear theory are treated in more detail.

Chapter 2 describes a study, by the activation method, of the (γ,n) excitation function of Cu^{63}, made with gamma rays of energies 12.2, 14.8, 16.7 and 17.6 MeV from the $Li^{7}(p,\gamma)$ and $B^{11}(p,\gamma)$ reactions. Residual activity and gamma ray intensity were measured with NaI(Tl) scintillation spectrometers. The object was to check the shape and absolute normalization of this excitation function, which is often used as a standard but about which conflicting reports have been made. The shape of the curve obtained in this way is in good agreement with bremsstrahlung measurements, but the present absolute cross sections are about 30% lower. The discrepancy is attributed

to difficulties in absolute β-counting and in measurement of X-ray intensities.

An extension of this work is described in chapter 3. It consisted of measurement, with the $Li^7(p,\gamma)$ resonance radiation, of the (γ,n) cross sections of four other nuclei relative to that of Cu^{63}. Comparison with bremsstrahlung data is made using the experimental intensity ratio of the 14.8 and 17.6 MeV components of the radiation. It is shown that early measurements using β-counting of thick samples were sometimes in error by as much as a factor of 2, but that recent experiments utilizing 4π β-counting of thin samples are much more accurate.

In chapter 4 is described a measurement of competition between the (γ,n) and $(\gamma,2n)$ reactions in Ga^{69}. From determination of the yield curves by activation methods the excitation functions σ_1 and σ_2 for these reactions were obtained from their thresholds to 31 MeV. The absorption cross section $\sigma_1 + \sigma_2$ has its maximum at about 16.2 MeV and a width Γ of 9 MeV; both results are consistent with the known systematics of the photonuclear process. The total integrated cross section to 30 MeV is 2.2 ± 0.4 times that of the $Cu^{63}(\gamma,n)$ reaction. Determination of the energy at which σ_1 and σ_2 are equal shows that for excitation by gamma rays of 25 MeV the first neutron emitted from Ga^{69}

has a median energy of $\sim$ 5.5 MeV, twice as high as can be explained by evaporation from the excited nucleus. It is deduced that at this gamma ray energy at least 40% of the first neutrons are emitted in a direct interaction with the photon. Further aspects of the results show tentatively that a recent suggestion, to the effect that even in a direct interaction an exchange energy of $\sim$ 7.5 MeV is left in the nucleus, may not always be true.

The final experiment (chapter 5) consisted of the measurement, for 15 nuclei, of the isomeric ratio in the residual nucleus, after a (γ,n) reaction initiated by 30 MeV bremsstrahlung. From these ratios and a recent application of statistical theory, was deduced information on the dispersion parameter σ, which relates the density of energy levels of spin J to that of levels with J = 0, and is closely related to the moment of inertia of the excited nucleus. Comparison is made with the corresponding quantity σ_s derived from shell theory. The ratio σ/σ_s is close to unity for $A \lesssim 40$ and levels off at $\sim$ 0.6 for $A \gtrsim 100$, with a transition region in between. The moment of inertia of an excited nucleus (with average excitation energy 4 - 5 MeV), is therefore close to the shell model result for a light nucleus and falls to about 1/3 of this in a heavy element. These results are discussed in terms of nuclear structure theory and some further experiments are suggested.

CONTENTS

CHAPTER 5

Isomeric Ratios in (γ,n) Reactions and the Spin-dependence of Level Density

LIST OF DIAGRAMS

LIST OF TABLES

CHAPTER 1

PHOTONUCLEAR REACTIONS

1. Introduction

Nuclear photodisintegration, discovered by Chadwick and Goldhaber in 1934, has had a useful part to play in the study of the two-nucleon interaction and nuclear structure and dynamics. Further experimental studies group roughly into those of the deuteron, the light nuclei, and the heavier nuclei, with photon energies ranging from a few MeV to the hundreds of MeV needed to study meson effects. As energy is transferred to the nucleus by electromagnetic forces the information obtained is supplementary to that from the usual nucleon induced reactions.

Many detailed theoretical and experimental studies of photodisintegration of the deuteron have been made, as it is one of the simplest and best ways of investigating the neutron-proton interaction, and can be carried out over a large energy range. Measurements on slightly heavier nuclei, e.g. Be^9, can be compared with detailed shell-model predictions. The roles played by "core" and "valence" nucleons and "clustering" of the nucleons into subunits can be studied. In the medium and heavy nuclei, the investigation of systematic changes in the excitation and de-excitation processes with photon energy, mass number and shell structure leads to further knowledge of nucleon motions in the nucleus.

The fundamental discovery in this field is that of the "giant resonance" in the photon absorption by a nucleus. Experiment has shown this to be a property of all nuclei, so its cause must be quite fundamental. Early work showed that the width of the resonance averaged about 6 MeV, that the peak energy decreased regularly with the mass number A from $\sim$ 20 MeV for light nuclei to $\sim$ 14 MeV for heavy nuclei such as lead, but that the cross section integrated over photon energy increased with A. The explanation of this third fact was an early success for the theory. The giant resonance is so large that it must be mainly due to E1 transitions in the nucleus; modification of the E1 "sum-rules" originally developed for the atomic photo-effect showed that the integrated cross section should be proportional to $\frac{NZ}{A}$ or $\sim \frac{A}{4}$.

For the explanation of the position and width of the giant resonance, two types of models for E1 absorption by the nucleus were proposed. In the collective models, based on the strong-interaction picture of the nucleus, the protons were supposed to oscillate in some way against the neutrons. The quite different weak-interaction view of the nucleus gave rise to the independent-particle model of the giant resonance, in which photon absorption raised just one nucleon to an excited state. Although these models are quite different in conception recent work suggests they are both partly correct, with the true picture somewhere in between.

A photonuclear reaction is usually thought of as taking place in two steps, photon absorption then the subsequent de-excitation of the nucleus, though this division does not always exist. Details of the excitation process are obtained from relative yields of the various emitted particles, their energy spectra and angular distributions. Such experiments have shown that although absorption in the giant resonance region usually produces an excited compound nucleus, in a few of the interactions a nucleon is emitted directly. A complete theory of photon absorption must explain how this occurs.

Although the proposed models have made possible useful predictions of the main parameters of the giant resonance, some of the assumptions made have been rather suspect. In particular, the calculations of the peak energy seemed unsatisfactory. However, recent advances in the understanding of the nucleus as a many-body system have shown how this fundamental problem may be solved. The answer lies in understanding the link between the independent-particle and collective aspects of the nucleon motions, and the importance of correlations within the nucleus. It is certain that photonuclear studies will continue to play a part in the investigation of this aspect of the nucleus.

In sections 2, 3 and 4 of this chapter the photon absorption and decay of the excited nucleus are treated in more detail. In section 5 are described some recent advances in the theory of the

giant resonance, while section 6 discusses the relevance of the present experiments to aspects of the photonuclear process.

2. Photon Absorption by the Nucleus

2.1 The Giant Resonance

Photon absorption in all nuclei occurs mainly in the giant resonance, which shows that some very general property is involved. The resonance is broad, with an average width Γ of about 6 MeV. The width has been found to vary significantly with shell structure (review, Fu 61), being narrowest (4 - 5 MeV) for nuclei with doubly closed shells. Plausible explanations of this have been offered (sections 3.1 and 3.2), but these have been criticized (section 5.4).

Although it is desirable to study the giant resonance by total absorption, this difficult measurement has been done in only a few cases (Du 59, Ko 59, Zi 60, Ca 60a) and with low accuracy; the nuclear absorption is only a few per cent of the total absorption. The alternative has been to measure the partial cross sections (γ,n), (γ,p), $(\gamma,2n)$ etc., either by direct particle detection or by activation methods. It is rare that all of these have been measured for a given nucleus. For light nuclei the (γ,n) and (γ,p) cross sections are often comparable, but for medium nuclei neutron emission predominates, with multiple neutron emission important for heavy nuclei (Ca 58, Si 58). Thus most studies of the magnitude and shape of the giant resonance have been made by detection of

the photoneutrons (e.g. Mo 53), or by measuring the residual activity from the (γ,n) reaction (e.g. Be 54).

Such measurements, usually made with bremsstrahlung X-rays, have been beset by difficulties in absolute normalization and by lack of resolution, but have shown a steady improvement. The recent development of monochromatic γ-ray sources from the annihilation in flight of energetic positrons (Se 60), promises more accurate experiments in the future. In the meantime it has been possible, in careful experiments with bremsstrahlung, to detect fine structure in the giant resonances of light nuclei (Ki 59, Mu 59, Th 61) and demonstrate the splitting into two broad peaks in those of distorted nuclei (Fu 58, Th 60).

The giant resonance may alternatively be studied by using the detailed balance principle to relate measurements of the inverse reaction. This has so far been restricted to the (γ,p) and (p,γ) reactions in light nuclei (Ta 59, Ka 60). It also seems possible to derive information from high-energy (p,p') scattering (Ka 59).

2.2 Sum Rules

As excitation by an incident photon is an electromagnetic process it is possible to apply "sum rules", and these have been very important in the theory. They are able to predict properties of the interaction from the ground state wave function only, so

that knowledge of those of the excited states is not required. The basic sum rule for the atom states (Le 60) that the total oscillator strength for all possible E1 transitions from the ground to excited states is equal to the number of electrons, i.e.

$$\sum_n f_{on} = Z \ . \qquad \text{(Atom)} \qquad (1)$$

When applied to the nuclear case this must be modified to allow for motion of the centre of mass of the nucleus; the sum rule becomes

$$\sum_n f_{on} = \frac{NZ}{A} \ . \qquad \text{(Nucleus)} \qquad (2)$$

From this it is easy to show that the integral of the E1 absorption cross section σ over photon energy, σ_{int}, is given by

$$\sigma_{int} = \int_o^{\mu} \sigma dE = \left(\frac{2\pi^2 e^2 h}{Mc}\right)\frac{NZ}{A} \qquad (3)$$

$$= 0.060 \frac{NZ}{A} \text{ MeV-barns.}$$

The upper limit μ is set at about 150 MeV, the meson production threshold, as above this energy the simple theory does not hold. The derivation of (3) assumes the absence of attractive exchange forces in the nucleus, and σ_{int} is increased if these are included. Levinger and Bethe (Le 50) obtained with the use of a reasonable Yukawa potential well

$$\sigma_{int} = 0.060 \frac{NZ}{A}(1 + 0.8\ x) \ , \qquad (4)$$

where x is the fraction of Majorana exchange force in the neutron-proton potential. Equation (4) has recently been shown to be incorrect (section 5.2); the exchange term should have an extra $A^{\frac{1}{3}}$ dependence. The newer calculation (Ca 60) looks more closely

at the nucleon correlations after an E1 excitation. Comparison of experimental results with equation (4) showed that within the rather large uncertainties the giant resonance was primarily E1 in character.

The integrated cross section has also been obtained from dispersion theory (Ge 54), a calculation which automatically includes all multipoles and absorption mechanisms. Clark (Cl 61) used the dipole sum rule to investigate the effect on σ_{int} of a repulsive core in the nuclear potential. He found that σ_{int} was considerably increased.

Other dipole sum-rules can be derived, and from them some useful mean energies (Le 60). For example, the fact that the harmonic-mean energy $E_h = \int \sigma dE \Big/ \int (\sigma/E) dE$ is closely equal to the peak energy E_m was used by Carver and Peaslee (Ca 60) to obtain an improved expression for E_m as a function of A (section 5.2).

Although use of the various sum-rules and mean energies could in principle give information on the shape of the giant resonance, present calculations have not been sufficiently accurate to do so. The main use of sum rules has been to show which features of the photonuclear effect are model-independent and must be shown by all models proposed, and which may be unique to a given model.

3. Models for the Giant Resonance

Sum rules give a good account of the main features of the giant

resonance but provide no physical picture of what is happening; models for the photon absorption process have therefore been invented and it is hoped that experiment will show which is closer to the truth.

For absorption in the giant resonance region two types of model have been proposed: the collective or "long range correlation" type based on the strong interaction picture of the nucleus, and the independent particle model developed from the simplest type of shell theory. For photon energies above about 40 MeV these are replaced by the "high energy" model which assumes interaction with a "quasi-deuteron" subunit in the nucleus. Above $\sim$ 150 MeV meson effects must be considered.

3.1 The Collective Models

Goldhaber and Teller (Go 48) suggested three possible collective mechanisms for E1 absorption. The first, in which the protons oscillated about mean positions, has not been considered further; the second, in which interpenetrating neutron and proton spheres oscillated about their centre of mass, was developed by them and by Fujita (Fu 56); a third which suggested oscillations in density of proton and neutron fluids inside the spherical nucleus (the "hydrodynamic model") was extended by Steinwedel et. al (St 50).

The second and third models were fairly successful in predicting the dependence of E_m on A, were shown to exhaust the dipole sum, and

could explain qualitatively the width of the resonance by processes akin to "friction". Fujita (Fu 56) extended the rigid-spheres model by suggesting how exchange forces could increase E_m.

An important prediction from the hydrodynamic model was made by Danos (Da 58) and by Okamoto (Ok 58). In this model a nucleus of ellipsoidal shape can sustain oscillations of different frequencies along its major and minor axes. Hence it was suggested that the width of the giant resonance would increase with the ellipticity of the nucleus, i.e. with the distance from doubly closed shells. For very distorted nuclei the resonance should split into two peaks, whose separation could be deduced from the eccentricity of the nucleus. Careful work on the rare earth nuclei (Fu 58, Th 60) and some lighter distorted nuclei (Sp 58) has verified that splitting does occur, although it is not yet clear if the relative intensities of the peaks agree with prediction (Fu 61).

3.2 The Independent Particle Model

The independent particle model (I.P.M.) is based on the quite opposite assumption of independent nucleons in a common potential well (Wi 56, Wi 59). The incident photon is assumed to excite one nucleon (usually from a closed shell) to an excited state, i.e. a large excitation of one nucleon replaces the small excitations of

many nucleons in the collective models. Although the shell model levels are complicated and apparently haphazard at high excitation energies, the E1 type of absorption restores simplicity to a considerable extent by selecting only particular transitions. Wilkinson shows that most of the dipole sum is taken up by transitions of the type

$$1s \longrightarrow 1p, \qquad 1p \longrightarrow 1d \qquad \text{etc.}$$

$$\text{and } 2s \longrightarrow 2p, \qquad 2p \longrightarrow 2s, \qquad \text{etc.},$$

i.e. elevation of nucleons between successive major shells. These are the allowed one-quantum* transitions for the simple harmonic oscillator potential, for which they all have the same energy. Although this degeneracy is removed in more realistic potentials the transition energies are still sufficiently equal to produce the giant resonance. The resonance exhausts the dipole sum since this is true of the simple oscillator potential. Nucleons in low-lying closed shells contribute to the dipole sum by preventing, by the Pauli principle, downward transitions from the higher shells.

This model cannot be taken too literally, since there are thousands of compound nucleus levels instead of a few shell-model levels. The spread of the compound nucleus levels about a shell level is one of the factors determining the width of the giant resonance, and was found by Wilkinson from the absorption part of

---

* For discussion of one-quantum, three-quantum, etc. transitions, see section 5.3

the optical-model potential. The other important contribution to Γ for spherical nuclei is the spread in energy of the single-particle transitions.

Wilkinson (Wi 58) used the Nilsson level scheme for an ellipsoidal potential well to show that the I.P.M. model could satisfactorily explain the widening of the giant resonance in a distorted nucleus. For strongly distorted nuclei the resonance would split into two peaks, as previously predicted by the hydrodynamic model. The correspondence between the predictions of each is so close that there is no chance of discriminating between the models on this basis.

The fundamental difficulty of the I.P.M. model is to obtain the correct value for E_m. This would be thought to equal the average separation E_s of the shell model levels, but this is $\simeq 40\ A^{-\frac{1}{3}}$ MeV, only half the required amount. A small improvement was made by adding to E_s the energy (~ 2 MeV) needed to remove a nucleon from a closed shell, but finally the only solution was to assume an "effective mass" for a nucleon given by $M^* \simeq \frac{M}{2}$. This doubles the theoretical E_s and makes it possible to say $E_m = E_s$.

However, the effective mass assumption was itself a step towards a collective model, and was always rather suspect, and direct measurements of E_s with (d,p) reactions (Sc 59, Co 60) showed it to be incorrect. Recent advances in the many-body

theory of the nucleus have not only given a better explanation of the value of E_m but have shown the relationship between the two apparently incompatible types of model for the giant resonance. These developments are described in section 5.

A significant advantage of the I.P.M. model is that it can explain the small fraction of direct emission processes which are found to occur (section 4). From its basic nature the collective model cannot predict anything of this kind. The motion envisaged in it is simple and its consequences easily calculated; the I.P.M. model can make more detailed predictions but at the cost of much computation.

The simple motions envisaged in both of these models last only a very short time (a few times 10^{-22} sec.), and are soon broken down by scattering within the nucleus.

4. Photonuclear Reaction Products

Study of the emitted particles has shown that in photonuclear reactions in the giant resonance region an excited compound nucleus is usually formed, but that in a small but significant fraction of the interactions a particle is emitted directly. The I.P.M. model is based on each interaction being a direct process, hence it can easily explain direct emission, but it is not a natural part of the collective models.

If the excitation energy is shared among all the nucleons, the decay is described by the usual compound nucleus theory (Bl 52). For light nuclei the decay may involve well-separated resonances, and calculations of branching ratios, energy spectra and angular distributions use the properties of the excited states and selection rules for angular momentum and parity. For heavier nuclei, in which there are many overlapping resonances, the statistical theory is used (Le 59, Er 60). The probability of emission is proportional to the density of states in the residual nucleus and a penetrability factor for the given type of particle.

The main characteristics of the decay of a compound nucleus are the following (Bl 52):

(1) Angular distributions of emitted particles must always be symmetrical about 90° and for the low energy particles are usually isotropic. In addition it can be shown (Le 60) that for E1 or M1 excitation the distribution must be of the form $a + b \sin^2 \theta$.

(2) Emitted neutrons have a roughly "Maxwellian" energy spectrum peaking at the nuclear temperature, $\sim$ 1 or 2 MeV.

(3) The proton energy distribution peaks close to the barrier height and is deficient in low energy particles, as compared with the Maxwell distribution.

(4) Yields of charged particles should in general be much less than that of neutrons due to the effect of the Coulomb barrier.

In the lighter nuclei neutrons and protons are emitted in roughly equal numbers, with the relative yield for a given nucleus determined largely by the neutron and proton separation energies. The large coulomb barrier in heavy nuclei reduces proton emission to less than one per cent of the neutron yield. Emission of deuterons and alpha particles is much less likely than that of protons. For a sufficiently excited nucleus multiple nucleon emission can occur, in particular the (γ,2n) and (γ,3n) reactions.

Most photonuclear reaction products follow the compound nucleus predictions. However, Hirzel and Wäffler (Hi 47) showed that for nuclei with $Z > 45$ photoproton yields were 100 or 1000 times greater than expected, showing that direct emission was occurring in a small fraction of the interactions. This conclusion has been confirmed by numerous experiments of other types: energy spectra and angular distributions of photoprotons (Ta 60, Ba 60), and photoneutrons (Au 59, As 60); relative branching ratio for (γ,n) and (γ,2n), (Ca 58, Ca 58a); yields of alpha particles (Ca 60a). The most conclusive evidence comes from measured angular distributions of fast photoprotons (Ba 60). For direct interactions the E1 - E2 interference term produces a forward-peaked distribution (Br 58) of the form

$$a + b \sin\theta\,(1 + p\cos\theta),$$

where $p \sim 1$ for protons but ~ 0 for neutrons.

The Wilkinson model is able to predict the fraction of directly emitted particles. For example, a proton may be directly excited to

a state in the continuum; because this state is not stationary it has a width $\Gamma_p + 2W'$, where Γ_p is the proton escape width and W' the absorption term in the optical-model potential. The proportion of these protons which escape directly is then $\frac{\Gamma_p}{\Gamma_p + 2W'}$. Calculations on this basis show satisfactory agreement with experiment.

The occurrence of both direct emission and compound nucleus formation has been found in other types of nuclear reaction (Er 60a). The series of events in the nucleus which form the link between them is not yet completely understood.

5. Recent Advances in Photonuclear Theory

Understanding of the nucleus has been increased by further knowledge of the many-body problem, which is fundamental also to such diverse fields as plasma oscillations and superconductivity. Correlations between the particles (nucleons or ions and electrons) are of great importance in determining the properties of the system. The further difficulty in the nuclear case is that the forces involved are not well known and are quite different from electromagnetic forces.

Such studies were used by Bohr and others (Bo 53) in the development of the "unified model" for the low-lying excited states of many nuclei. These states arise from collective motions-rotations and vibrations - in which the protons and neutrons move

together. The quite different type of collective motion in which the neutrons move oppositely to the protons, the "dipole state" of nuclei, has been effectively studied only recently and the theory is still developing. The theory in both of these cases arose from improvements to the independent particle model, and has been in no way related to any classical model, although the results are often surprisingly similar.

There have been three recent approaches to the dipole state or giant resonance problem: (1) Particular nuclei have been treated, using detailed experimental data for shell level positions etc., and a full treatment of configuration mixing; (2) General features of the dipole state for both nuclei and "nuclear matter" have been derived from many-body theory; (3) Sum rules have been applied to obtain general relations applying to all nuclei. Each approach has had something useful to say, and the main examples of each will be briefly described.

The giant resonance will be discussed under two main heads: the relationship between different models of its nature, and calculation of its position for any given nucleus. The two aspects are naturally very closely related. Such developments have suggested revisions in other regions of photonuclear theory. Thus in section 5.3 we discuss "overtones" of the giant resonance, related to the direct emission process, and in section 5.4 a recent view on the splitting of the giant resonance.

5.1 Relationship between Collective and Independent-Particle Models

The single-particle and collective models of the giant resonance seemed to be completely different. However in an important paper, Brink (Br 57) showed that for the simple harmonic oscillator (S.H.O.) potential they were identical, and were probably not greatly different for real nuclei. He began by showing that the E1 operator Q_1 for a nucleus could be expressed in two equivalent forms:

$$Q_1 = e \sum_z (\underline{r}_i - \underline{R}) \qquad (1)$$

$$= e \frac{NZ}{A} \underline{r} , \qquad (\underline{r} = \underline{R}_z - \underline{R}_N), \qquad (2)$$

where $\underline{R}$ is the radius vector of the centre of mass of the nucleus, $\underline{R}_z$ and $\underline{R}_N$ are similarly defined for the protons and neutrons, respectively, and $\underline{r}_i$ is the radius vector of the i'th proton in the nucleus. In form (1), Q_1 is the sum of one-particle operators and connects nuclear wave functions differing at most by the state of one particle. In the second form, however, it is expressed in terms of the collective coordinate $\underline{r}$, so already we have a suggestion of collective motion.

He treated the case of the S.H.O. potential, for which the coordinate $\underline{r}$ is separable. By analyzing the Hamiltonian into four parts he showed that after an E1 absorption the wave function for the excited state was

$$\Phi_1 = \psi_z \chi_N \alpha_o (\underline{R}) \beta_1 (\underline{r}). \qquad (3)$$

Here ψ_z and χ_N contain only the relative coordinates of the protons and neutrons respectively. Thus Φ, represents a collective motion of all the protons against all the neutrons in which the proton and neutron internal motions remain undisturbed, i.e. it is the Goldhaber-Teller oscillation of two interpenetrating spheres. Hence the E1 absorption produces just that linear combination of single-particle excitations which corresponds to the collective vibration.

Brink took a step away from this idealized case by introducing a more realistic potential; the collective state becomes a superposition of single-particle states which now have slightly different energies. Their relative phases are not preserved and they get out of step in a time $\sim\frac{\hbar}{\Gamma}$, thus the collective motion is quickly dissipated into incoherent single particle modes. Brink's achievement has therefore been to show that the collective and single-particle description is contained in the same wave function.

Developments described in the following section confirm Brink's conclusions, and go further by suggesting how such effects arise in the nucleus.

5.2 The Peak Energy of the Giant Resonance

Elliott and Flowers (El 57) carried out a detailed shell-model calculation in intermediate coupling for the doubly closed-shell nucleus O^{16}, taking full account of configuration mixing. They showed that of the five possible E1 transitions with energies from

13.1 to 25.1 MeV, almost all of the dipole strength was concentrated in the two highest transitions at 22.6 and 25.1 MeV, in good agreement with the experimental value for E_m of 23.5 MeV. However, the distribution in strength of these two levels is the reverse of that predicted, and it is found that about half the integrated cross section lies above 25 MeV (Fu 61).

A calculation of the frequency of collective oscillations in nuclear matter was made by Brueckner and Thieberger (Br 60), in an attempt to clarify the relationship between the classical and independent particle calculations. They showed that oscillations of neutron and proton densities (of the hydrodynamic model type) were possible, with the collective motion leading to an increase of 15% in the frequency over the single-particle calculation. This happened because the single-particle energies in general depend on the fluctuation in neutron-proton densities typical of the collective oscillations, an important contribution to the energy of the collective mode which had been omitted in previous discussions. It was not possible to extrapolate their result to finite nuclei, but it seemed clear that the collective effect could lead to an increase of the eigenvalue above the single-particle result. It appears (Ca 60) that this result does apply to nuclei, but it is not the major effect that is required.

Neudachin et al. (Ne 61) used spectroscopic data to calculate the position and shape of the giant resonance for the nuclei Ca^{40},

V^{51}, Ni^{58}, Cu^{63} and Cu^{65}. They showed that account of the residual pair interactions, and more accurate estimates of the nucleon binding energies in closed shells, yielded E_m values in good agreement with experiment, without introduction of an effective mass less than M. However, the calculations seem rather unsatisfactory, as at no stage do they allow for the collective properties of E1 transitions. This has been shown by other treatments (see below) to be the factor which basically determines E_m, hence their good agreement with experiment may be rather fortuitous.

Brown and Bolsterli (Br 59) pointed out that the shell spacing E_s and the resonance energy E_m would not be equal, since in the dipole absorption a hole is formed in the lower shell. Using a schematic model they showed that coherent effects due to the particle-hole interaction should push the dipole transition to higher energies, though they could not say by how much.

The relation between the many-body and single-particle aspects in nuclei was discussed further by Brown and Thouless (Br 60a). They describe in more detail how the collective types of excitations in nuclei are built up from single-particle excitations through the nucleon-nucleon interaction. They emphasize that although the mechanism is the same in both finite and infinite systems the consequences are very different in the two cases. Thus the shell structure of the nucleus causes the single-particle excitations to be nearly degenerate in energy

and guarantees that the minimum energy is quite high, whereas in nuclear matter the energies form a continuous spread and begin at zero if there is no energy gap. Thus, quantitative and in some cases qualitative features of the collective phenomena depend on the finite nature of the problem.

In a more detailed study of the dipole state in nuclei, Brown et al. (Br 61a) performed calculations in j-j coupling with zero-range forces for O^{16} and Ca^{40}. Comparison with the finite-range calculations of Elliott and Flowers (El 57) for O^{16} showed that the zero-range calculations reproduced well not only qualitative but also quantitative features. They were able to show that the dipole state is quite stable against perturbations, suggesting that presence of valence nucleons would have little effect, as long as their contribution to the dipole transition amplitude was small.

The basic conclusions of the above group of three papers may be summarized: the particle-hole interaction concentrates the dipole-strength in the uppermost states, and shifts upward their energies.

Brenig (Br 61) made a detailed quantum-mechanical study of the hydrodynamic model. He showed that the classical expression for E_m was valid only for extremely strong interactions.

Carver and Peaslee (Ca 60) used the sum-rule approach. They calculate not E_m but the harmonic energy E_h, to which it is closely

equal. The sum-rule expression is known to yield $E_h = E_d + E_x$, where E_d arises from the direct part of the two nucleon force and E_x is special to the E1 operator and the charge exchange component of nuclear forces. They show that to first order E_x is independent of A. E_s and E_m are found to be related by

$$E_s = E_m - \left[(E_m - E_h) + 0.15\, E_d + E_x \right]$$

where the factor 0.15 comes from the work of Brueckner (p. 19). A fit to experimental results for E_m as a function of A shows that the first two terms in the bracket accidentally cancel, leaving the important result

$$E_m \simeq E_s + E_x \,.$$

Previous calculations have neglected E_x so have been unable to obtain E_m correctly. From experimental results for spherical nuclei they obtain

$$E_m = \left[(40 \pm 6)\, A^{-\frac{1}{3}} + 7.5 \mp 1.5 \right] \text{ MeV.}$$
$$= E_s + \Delta$$

The interpretation of the exchange term Δ is that it is energy shared among the other nucleons when one nucleon is excited, and is therefore not available in general for a direct emission process.

Their fundamental result is thus that E_m is obtained from E_s not by multiplication by a constant factor as in the Wilkinson treatment, but by addition of the constant term Δ. The effective mass is in the present case treated as a derived quantity and is found to be $(1.2 \pm 0.2)M$; this large value is attributed to the effects of finite nuclear boundaries.

The fact that E_x does not vary with A, as does E_d, allows an improved fit to the A-dependence of σ_{int}. They obtain

$$\int \sigma \, dE \approx 0.013 \, A \left[1 + 0.18 \, A^{\frac{1}{3}} \right] \text{ MeV-bns.}$$

This can be compared with the Levingèr-Bethe expression (section 2.2) in which the bracketed terms were $\left[1 + 0.8 \, x \right]$, with x constant.

Their treatment may be related to that of Brown by ascribing E_x to coherent interactions between particle-hole pairs formed by E1 excitation. It therefore arises from the charge-exchange part of the nuclear potential*.

5.3 Overtones of the Giant Resonance

An interesting development (Ca 61) of the coherent shift picture of the giant resonance suggests the possible importance of higher resonances than the first, (the "overtones"). In the shell model picture E1 excitation may in principle excite nucleons to the next, 3rd next, 5th next ..... shells in agreement with parity conservation. Such transitions have been called one quantum-, three quantum-, etc. jumps. For the simple harmonic oscillator potential the transition energies are in the ratio $W_1 : W_3 : W_5 \ldots = 1:3:5 \ldots$,

---

* In Brown's treatment the interactions are between protons and proton holes and between neutrons and neutron holes, therefore do not arise from charge-exchange; the two treatments can be shown to give the same results. (D. C. Peaslee, private communication. See also Appendix to Ca 61.)

but the matrix elements for jumps higher than the first are zero. Calculations by Wilkinson (Wi 56) for a square-well potential suggested that $\int \sigma_3 \, dW \Big/ \int \sigma_1 \, dW \simeq 3\%$. Such estimates of high transition energy and low cross section caused higher transitions to be ignored in the analysis of experimental data. However, as it is now realized (section 5.2) that about half of W_1 arises from the coherent shift, the new estimate for W_3 is much lower. Improved calculations for σ_3 show that effects of 3-quantum jumps may be important, especially in the direct emission of nucleons.

The energy of the giant resonance is given by (section 5.2)

$$W_1 = E_s + \Delta$$
$$\simeq 40\, A^{-\frac{1}{3}} + 7.5 \quad \text{MeV}.$$

From a similar argument, W_3 should be

$$W_3 = 3\, E_s + \delta$$
$$= 120\, A^{-\frac{1}{3}} + \delta.$$

The term δ is assumed to be similar in nature to Δ but smaller; a first estimate suggests $\delta = 3 \pm 2$ MeV. Thus W_3 falls near 25 MeV for heavy nuclei which is much less than $3W_1$ ($\sim$ 40 MeV) which was previously suggested.

As the exchange energy Δ is assumed to be shared among a number of nucleons, it is now believed that a 1-quantum transition cannot produce direct emission of a nucleon, though it will naturally contribute to evaporation processes. Hence direct ejection must be due to a 3-quantum transition. Calculations

of transition strengths for a square-well potential and a modified oscillator potential suggest that 3-quantum transitions could contribute up to 30% of the E1 absorption cross section.

A study of the (γ,p) peak energies of Cs, I, W, and Hg suggests the 3-quantum transitions dominate the (γ,p) cross section for these nuclei, but for lighter nuclei such as Ti the 1-quantum transitions dominate. They find some confirming evidence in fast neutron emission studies and inelastic scattering of 185 MeV protons at small angles. A rough estimate suggests that the quasi-deuteron effect predominates over 3-quantum transitions for $E_\gamma \gtrsim$ 60 MeV.

These writers conclude that although there is little doubt that 3-quantum transitions do occur, their relative importance is not yet known. The preliminary calculations show no conflict with experimental results. There is a need for further cross-section measurements above the giant resonance, to search for the three-quantum peak.

5.3 Splitting of the Giant Resonance

Peaslee (Pe 61) has extended the coherent shift calculations of E_m and puts forward a new explanation of the splitting of the giant resonance. He postulates that in the formula $E_m = E_s + \Delta$, for a given nucleus Δ can have two possible values Δ_1 and Δ_2; thus major peaks will occur at $E_{m1} = E_s + \Delta_1$ and $E_{m2} = E_s + \Delta_2$,

with separation $\delta = \Delta_1 - \Delta_2$. In contrast to previous explanations, the splitting is not directly related to the shape of the nucleus in its ground state, and the predictions of relative intensities and variation of δ with A are rather different.

Former theories for the splitting (sections 3.1 and 3.2) are criticized on several grounds. The E1 splitting is a function of the excited state, and it is very unlikely that the nuclear shape at 20 MeV excitation is the same as that of the ground state. One experimental result (Fu 60) seems especially significant; the peak splittings of the neighbouring rare earths Ho^{165} and Er are pronounced and almost identical, but Er contains 77% of nuclei with J = 0. This shows that the shape of the ground state cannot be a major cause of the splitting.

On the other hand the quantity Δ is a property of the E1 excited state and not of the ground state. Further, as the excited state must have $J \geqslant 1$ the objection to the Er result does not apply. The splitting can be related much more directly to the internucleon potential, from which all nuclear properties must eventually come.

Splitting of the giant resonance into two major peaks is now identified with incomplete shell closure, and their relative intensity is closely related to F, the fractional filling of the last major shell. The quantity $i = \frac{I_1 - I_2}{I_1 + I_2}$ should equal 1 at shell closure and 0 at mid-shell, while the peak separation δ

remains roughly constant; thus at a closed shell the lower peak is presumed to be still there but with vanishing intensity. This differs from the hydrodynamic model predictions of a constant value of $\frac{1}{3}$ for i and a value of δ which increases with ground-state deformation. Present experimental data do not seem accurate enough to show which theory is more correct.

Peaslee predicts that quadrupole distortion of the excited state will produce fine-structure peaks, with their number increasing linearly with A. Quadrupole deformation of the ground state, the fundamental cause of splitting in former theories, is suspected of reducing the separation of the main peaks rather than enhancing it.

This new development in the theory adds further interest to the study of peak splitting, and emphasizes the need for increasingly accurate experiments.

6. The Present Experiments.

The experiments described in this thesis fall into three groups.

Chapters 2 and 3 describe (γ,n) cross section measurements using monochromatic gamma rays from nuclear reactions, with the object of checking the normalization of previously published data. It is hoped that these measurements will assist in the comparison of integrated cross sections with the sum-rules (section 2.2).

Chapter 4 describes an experiment on the products of a

photonuclear reaction in a medium-weight nucleus. It is designed to show the relative importance of direct and compound nucleus reactions in the region of A = 70.

The experiment described in chapter 5 comes in a different category. It is not a direct study of the photonuclear process, but instead uses the (γ,n) reaction to investigate an important property of excited nuclei - their moments of inertia.

CHAPTER 2

CROSS SECTION FOR THE $Cu^{63}(\gamma,n)Cu^{62}$ REACTION, MEASURED WITH MONOCHROMATIC GAMMA-RAYS

1. Introduction

The cross section for the reaction $Cu^{63}(\gamma,n)Cu^{62}$ is often used as a standard for the normalization of new data and has been investigated by a number of workers, using either bremsstrahlung or the radiation from the $Li^{7}(p,\gamma)Be^{8}$ reaction. Results from the two methods are compared using the known composition of the lithium radiation (St 51). It consists of two gamma-rays, with energies $\sim$ 17.6 MeV (width $\sim$ 12 keV) and $\sim$ 14.8 MeV (width $\sim$ 1.9 MeV), with an intensity ratio at the 440 keV resonance of approximately 2 : 1.

Results to date, including the present measurement are summarized later in tables 2 and 3. The quantity σ_R (R $\equiv$ "resonance") has been calculated from the bremsstrahlung curves and is effectively the cross section which a measurement with the lithium resonance radiation would have given. The bremsstrahlung data are reasonably consistent. The curves peak at $\sim$ 17.5 MeV, and have maximum cross sections of about 100 mb; the gamma-ray measurements show more variation but give an average result of only about 50 mb. This is a serious discrepancy, suggesting the existence of systematic errors in one or both methods, and it is important to find its cause.

In absolute cross section measurements with X-rays the flux is usually measured with some form of ionization chamber, often a thimble chamber in a lucite block (Jo 50). The chamber is calibrated with a radioactive source and the relative response for higher energies calculated assuming that Gray's cavity theorem (Gr 36) holds up to the maximum photon energy used. The response function is rather dependent on the magnitudes adopted for quantities such as the γ-ray absorption coefficients of lucite and the electron stopping power of lucite relative to air, and it is not clear that the cavity theorem holds once the path-lengths of the secondary electrons become comparable with those of the X-ray quanta. Flowers et al. (Fl 52) did not use the cavity principle but calculated the response of a thick-walled aluminium ionization chamber from first principles, allowing for the effects of wall thickness and secondary X-rays. A comparison of such a chamber with a calorimeter, made by Kruglov (Kr 58), gave agreement within 5%.

For their intensity measurement, Krohn and Schrader (Kr 52) used a pair spectrometer calibrated from the photodisintegration of the deuteron. Probably the most reliable method used so far in these measurements was that of Berman and Brown (Be 54) and Scott et al. (Sc 55), in which the electron beam is extracted and collected in a Faraday cup. The radiation process is under greater control than with an internal target, and the bremsstrahlung

intensity can be calculated from the accurately known theory (Wi 53, Sc 51). The measured yield must be corrected for electro-disintegration, but this can be done by placing copper foils before and after the thick radiator.

In a circular machine the exact bremsstrahlung spectrum is less well known, as the multiple transmissions through the target give rise to an energy spread in the incident electrons. The resulting change in the spectrum is mostly confined to the high-energy tip. Penfold and Leiss (Pe 58) show by analysis of a given yield curve using two different spectra that the principal result of such a change in the spectrum is a small energy shift in the resulting cross section, associated with changes of a few % in absolute magnitude. It appears that such spectral variations will not be a major source of error in photonuclear work.

Although the Li^7 + p reaction is the most suitable for this type of experiment, the yield of γ-rays is still quite low, and irradiation must be made in poor geometry. Until the advent of the NaI crystal the flux was measured with a calibrated thick-walled Geiger counter (Ca 54) or by use of Hough's method (Ho 50). This consists in measuring the count-rate of a thin-walled geiger as a function of thickness of metal foil converter placed in front of it. Both of these methods are of low efficiency and it is difficult to make them accurate. In one experiment (Ha 56) a small NaI crystal was employed as a monitor.

A number of the experiments have employed the residual activation technique with detection of positrons from Cu^{62}. Absolute β-counting is very difficult to do accurately, owing to large corrections for self-absorption and back-scattering (Ba 53), and significant discrepancies could easily arise in the process. The results of Berman and Brown and of Scott et al. differ by 20% even though their methods for monitoring and β-counting were almost identical. Careful work by Roalsvig (Ro 59, Ro 60) using a proportional flow counter has shown that some previous measurements for other elements have been in error by up to a factor of 2.

Photoneutron detection arrangements of paraffin moderator and BF_3 counters (Ha 52) have been often used. The main difficulty is to make the system equally sensitive to neutrons having a range of energies; Halpern (Ha 52) did this by adjusting the position of the BF_3 counter until the shape of the yield curve agreed with that from activation measurements. A Ra-Be neutron source was used for calibration. The efficiency of Halpern's system was only 0.5%. Although they used such a system, Montalbetti et al. (Mo 53) adopted the cross section obtained by Katz and Cameron (Ka 51), and did not make an independent measurement.

It was evident that a more accurate measurement with the lithium radiation could be made by monitoring the γ-flux with a large NaI(Tl) crystal and measuring the annihilation quanta from Cu^{62} with a NaI scintillation spectrometer. The detection

efficiency for the γ-rays is about 80% rather than a few %, while the detection of γ^+ quanta does not have the pitfalls of β^+ counting.

The first part of the present experiment was therefore a redetermination of the cross section for the lithium resonance radiation. The second was a study of the shape of the cross section, from measurements at four γ-ray energies from 12 to 17.6 MeV.

The relative intensity of the 14.8:17.6 MeV γ-rays from lithium changes from $\sim$ 0.5:1 at E_p = 440 keV to $\sim$ 2:1 at E_p = 900 keV. The ratio for any given target and bombardment energy can be determined accurately from analysis of spectra in the large NaI monitor crystal. From measurement of the relative cross sections for the radiation from bombardments at two quite different energies, a simple calculation will therefore give the cross section at each γ-ray energy separately. Although of lower intensity, the radiation from the $B^{11}(p,\gamma)C^{12}$ reaction was used in a similar way to measure the cross section at 12.2 and 16.7 MeV.

The shape and magnitude of the cross section from these results was compared with bremsstrahlung measurements.

2. Experimental Method

2.1 General Techniques

The experimental arrangement of beam tube, target and beam-

Figure 1

Irradiation Geometry

The general layout of target and 5 in. NaI crystal with a magnification of the target arrangement, is shown.

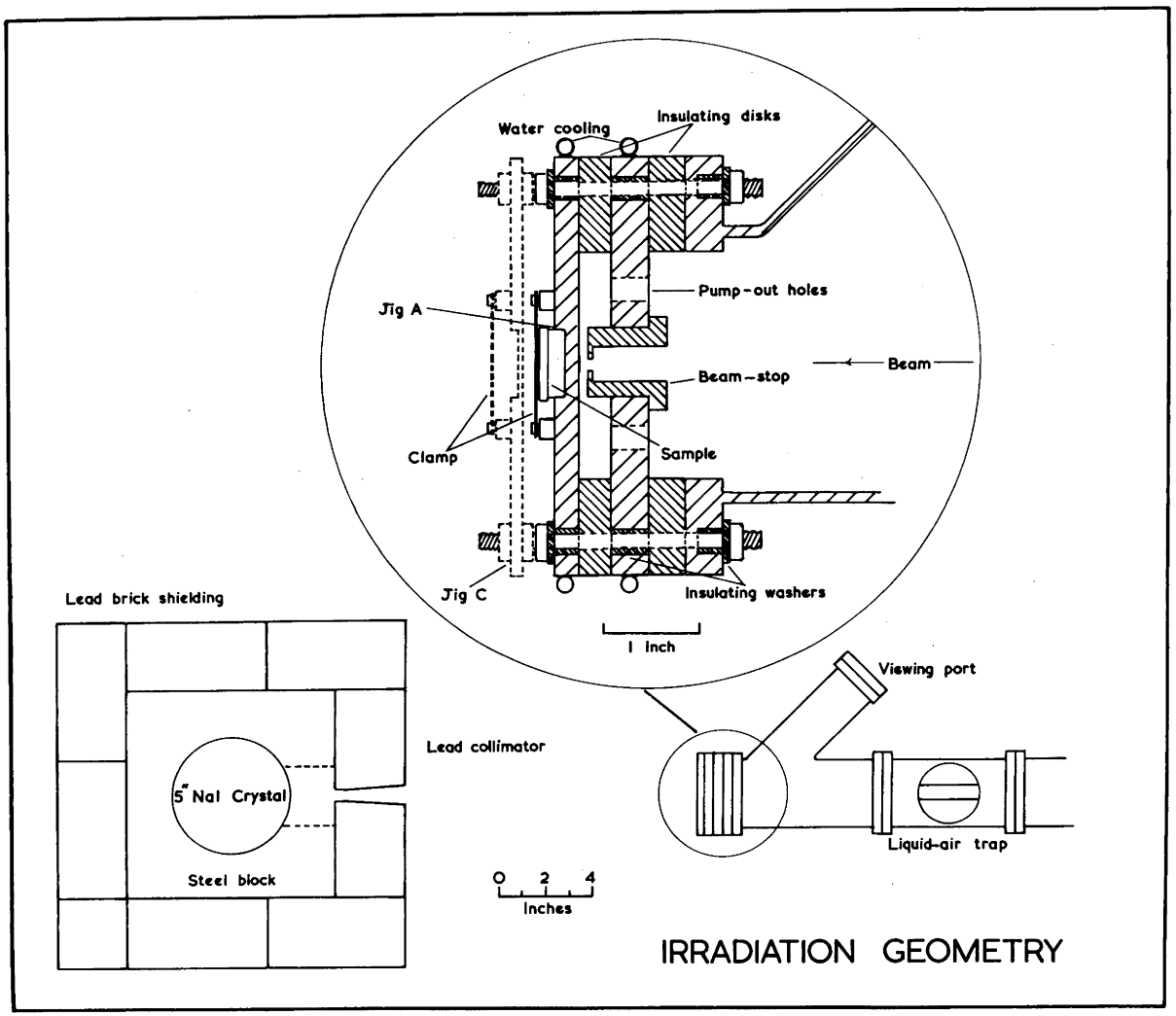

IRRADIATION GEOMETRY

stop, lead collimation, 5" x 4" NaI(Tl) crystal and lead shielding is shown in figure 1.

The proton beam from the Canberra 1.2 MeV H.T. set was analyzed by a 90° bending magnet and focused with strong-focusing electrostatic lenses through a 3/16 in. diameter hole in the copper beam stop, placed 1/8 in. before the target. The targets of natural lithium were $\frac{1}{4}$ in. in diameter and were either thick or of thickness about 150 keV for 600 keV protons. They were prepared in a separate vacuum system, and transferred quickly in a stream of argon. The lithium was evaporated from a molybdenum boat, and the copper target backing was shielded until the lithium surface was clean. Boron targets about 1 mg/cm^2 thick were made by the evaporation to dryness of a slurry of boron in alcohol. To give good adhesion to the backing the boron targets were 1 in. in diameter. Details of the production and nomenclature of the various γ-rays are summarized in Table 1.

The γ-ray flux was monitored with a 5 in. diameter by 4 in. NaI(Tl) crystal, of the Harshaw "matched window" line. This type of mounting, in which the crystal is viewed by a Dumont 6363 (3 in.) photomultiplier, has better resolution than the former type with a 5 in. phototube. The present crystal gave a resolution of 11% for the 20 MeV $T(p,\gamma)$ line (Figure 2). The crystal was mounted in a steel block with its axis vertical and the beam entered along a diameter. This is not the usual

Table 1

Gamma Rays used in Experiment

Reaction	Gamma Ray Energies (MeV)	Target Preparation	Target Thickness	E_p (Kev)	Intensity Ratio at 0° (present work)	Nomenclature	Angular Distribution	Approximate Relative Intensity
$Li^7(p,\gamma)Be^8$	"14.8"	Vacuum Evaporation of natural lithium	Thick	450-550	17.6:14.8	Lithium "resonance radiation"	Both isotropic	100
					1.94 ± 0.1			
	$14.35 + \frac{7}{8} E_p$							
	"17.6"		150-200 Kev	800-900	~ 0.53	Lithium "non-resonance radiation"	Both anisotropic	10
	$17.25 + \frac{7}{8} E_p$							
$B^{11}(p,\gamma)C^{12}$	"12.2"	Evaporation of slurry of boron in alcohol	1 mg/cm²	660	12.2:16.7		Both anisotropic	5
					5.62 ± 0.1			
	$11.53 + \frac{11}{12} E_p$							
	"16.7"			900	2.76 ± 0.05		Both anisotropic	8
	$15.96 + \frac{11}{12} E_p$							

arrangement but for a narrowly-collimated beam gives a 25% greater path-length through the crystal, and is more convenient in that the photomultiplier is vertical rather than horizontal. The lead collimators were each 3 in. thick. That used during most of the experiment had a hole 9/16 in./diameter at the narrow end, with a 5° taper. For lining-up, light was shone through a small hole in a temporary plug at each face of the collimator. The rear collimator-face was 40 cm. from the target.

Photomultiplier pulses were fed from a preamplifier through a Higinbotham non-overload amplifier to a 100-channel kicksorter of the Hutchinson-Scarrott type. Two scalers in parallel were biased to count all pulses above the valley of the spectrum (9.5 MeV for both $Li^{7}(p,\gamma)$ and $B^{11}(p,\gamma)$). Spectra were taken at intervals during an irradiation so that small drifts in gain could be corrected.

As the samples were irradiated very close to the target many γ-rays entered at large angles, whereas the monitor crystal sees only the spectrum near 0°. Hence any anisotropy of the radiation must be allowed for in the determination of relative yields. Where required, the angular distribution was measured under the same target and beam conditions as an irradiation so that the correction could be made. The crystal was set up on a steel beam pivoted beneath the target. With a similar crystal at 60° as a monitor, the counting rates were determined at 0°, 35° and 55°; a similar measurement for the isotropic resonance

Figure 2

Response Function of 5 in. NaI Crystal

The response functions for 20 MeV and 12 MeV radiation are each compared with that for 16 MeV radiation. The energy scales have been adjusted to be the same in each case but the curves are slightly displaced for clarity.

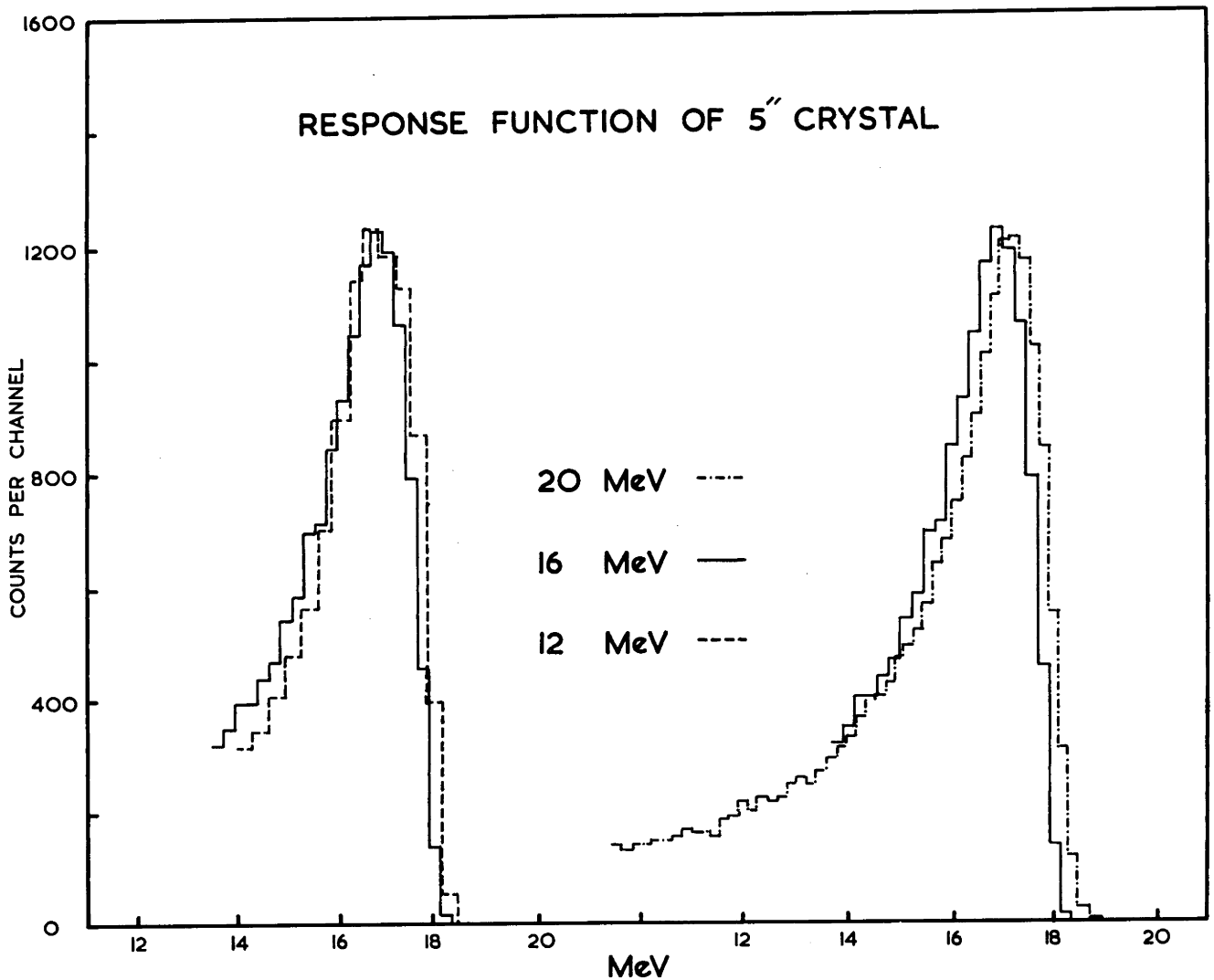
RESPONSE FUNCTION OF 5″ CRYSTAL
COUNTS PER CHANNEL
1600
1200
800
400
0
20 MeV
16 MeV
12 MeV
12
14
16
18
20
MeV

radiation allowed correction for the change of absorption in the target backing with angle. These approximate angular distributions were used to correct the observed yield to that had the radiation been isotropic, in the manner described in Appendix B.

Although the size of NaI crystal used for γ^+ detection was not the same in all parts of the experiment, the general procedure was always identical. Pulses from the preamplifier were amplified by a Higinbotham non-overload amplifier and fed to the kicksorter. Usually a single-channel analyzer was set to cover the photopeak. Further details are given in the relevant sections.

2.2 Analysis of Gamma-Ray Spectra

Intercomparison of the cross sections for the lithium and boron radiations and determination of relative intensities of the constituent γ-rays required analysis of the monitor crystal spectra.

Each spectrum was first separated into its constituent peaks, using the line-shape given by the 20 MeV $T(p,\gamma)$ line. This was obtained by bombarding a zirconium-tritium target with 850 keV protons and observing the spectrum at 90^{o} to the beam with the usual crystal and collimator arrangement. A comparison with the shapes given by the 12 and 16 MeV lines from $B^{11}(p,\gamma)$ is shown in figure 2; the energy scales of the other two lines have been

Figure 3

Analysis of a Resonance Spectrum

The resonance $Li^7(p,\gamma)$ radiation from a thick target is shown, with its analysis into 14.8 and 17.6 MeV components.

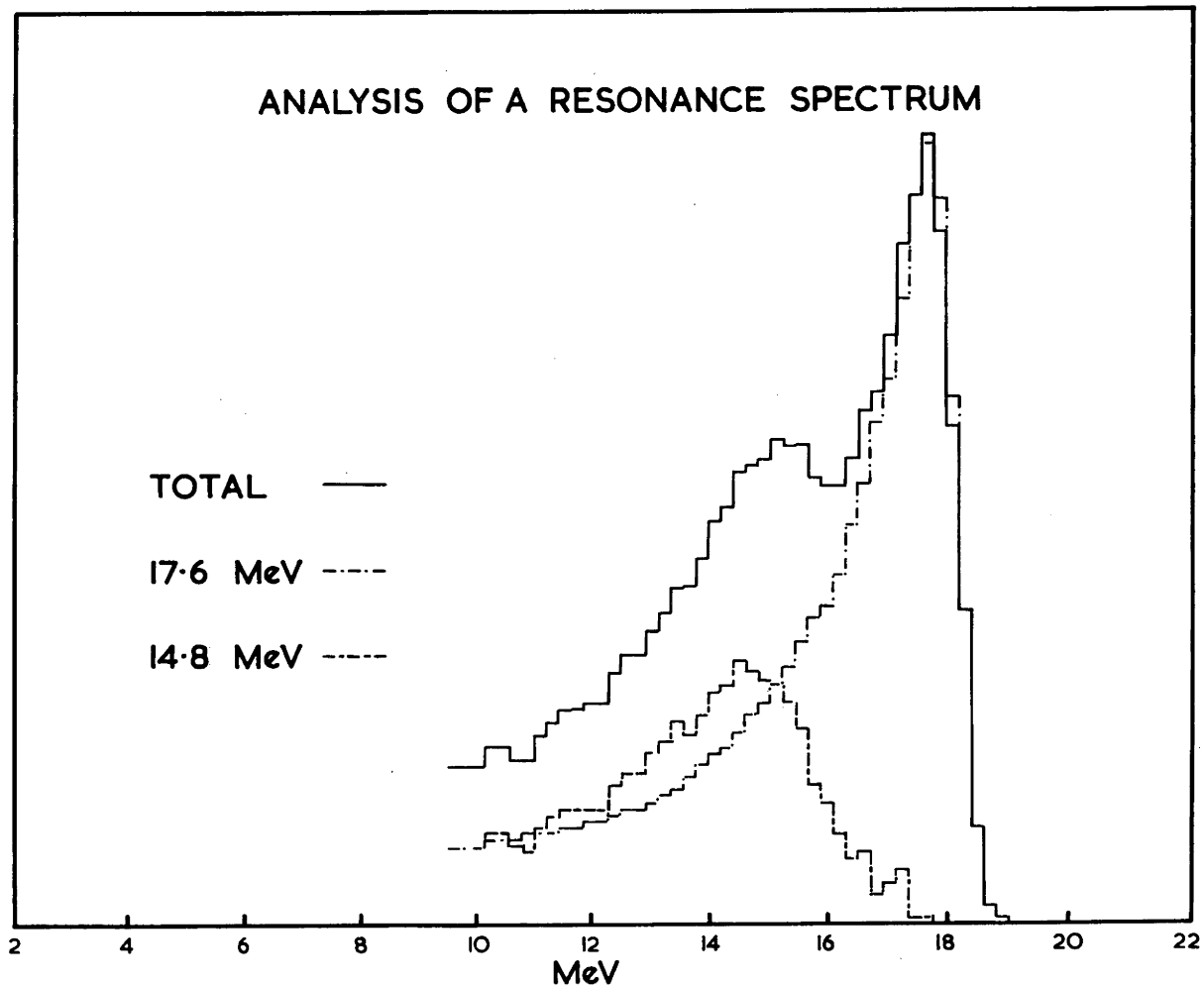
ANALYSIS OF A RESONANCE SPECTRUM
TOTAL
17·6 MeV
14·8 MeV
2
4
6
8
10
12
14
16
18
20
22
MeV

Figure 4

Analysis of a Non-resonance Spectrum

This spectrum was obtained from bombardment of a lithium target 150 keV thick with 850 keV protons.

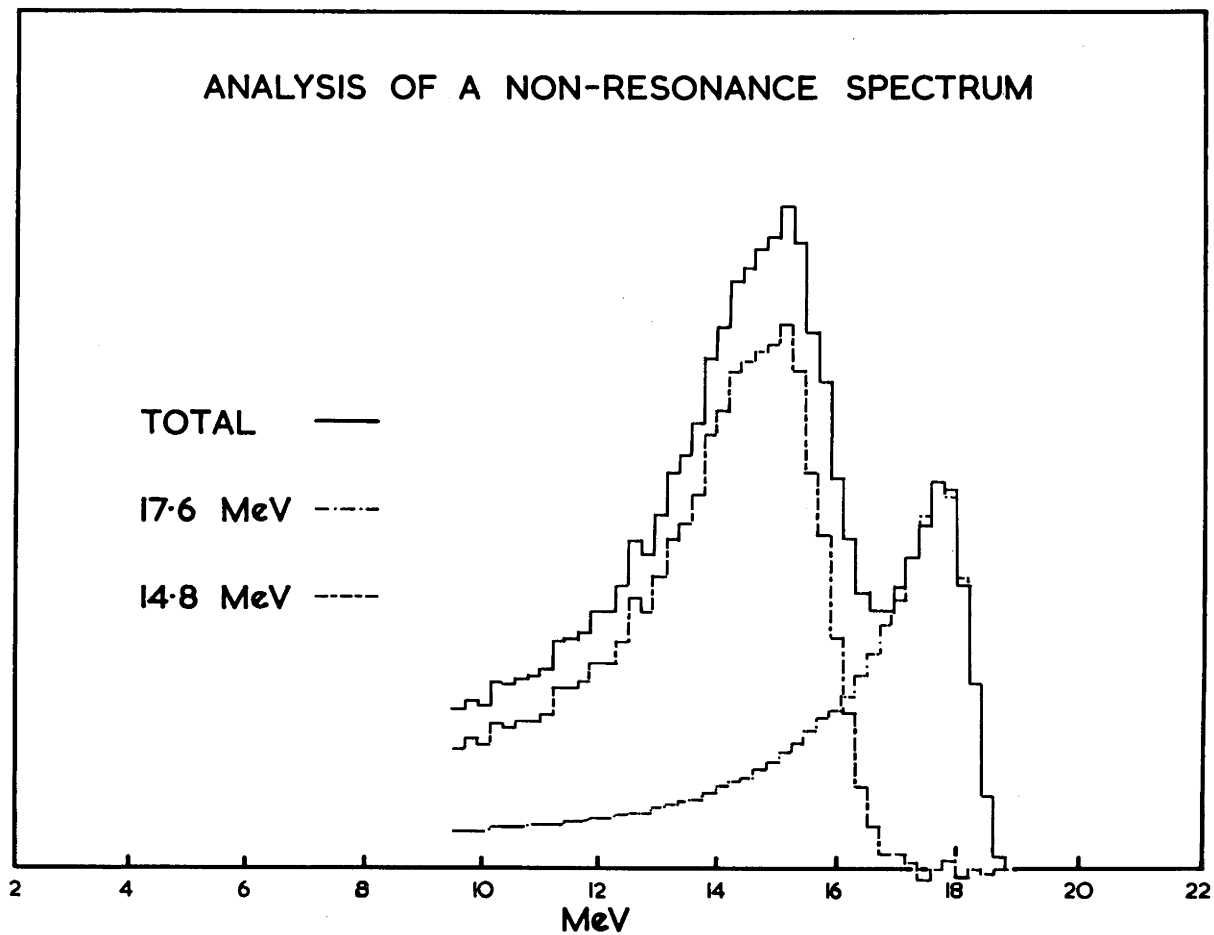
ANALYSIS OF A NON-RESONANCE SPECTRUM
TOTAL
17·6 MeV
14·8 MeV
2
4
6
8
10
12
14
16
18
20
22
MeV

expanded, keeping the same zero, but the curves are drawn slightly displaced for clarity. Although the 12 MeV line has a slightly lower tail there is negligible difference between the other two lines; similar conclusions were reached by Kockum and Starfelt (Ko 59). The 20 MeV line-shape can therefore be used for analysis of the lithium spectra.

The tritium line (with a suitable energy scale) was normalized to the upper edge of the 17.6 MeV line and subtracted, to leave the 14.8 contribution. Typical results are shown in figures 3 and 4. As a check on this method a separation was made by subtracting from a non-resonance spectrum a resonance spectrum normalized at the high-energy edge. Very good agreement for the shape of the lower energy line was shown by the two methods. Owing to its width of $\sim$ 2 MeV (St 51) this line has a quite different shape at the upper end. However, figure 5, in which the two curves enclose the same area, shows that the initial width of the line does not affect the spectrum shape below about 12 MeV.

As the peaks in the boron spectra were well resolved (figure 6), the analysis into components was a simple matter.

Using the analyzed spectra, the original monitor figures were corrected so that only the counts in each peak above 0.65 of the peak energy were included, e.g. above 11.4 MeV for the 17.6 MeV line. This was below the region where the width of the 14.8 MeV line affected the line-shape, but clear of the low-energy

Figure 5

Line-shapes from the lithium Radiation

The 14.8 MeV line-shape has been adjusted to the new energy scale by magnification, keeping the same zero. The area under the two curves is the same. The difference in shape due to the 2 MeV width of the 14.8 line is clearly seen, but there is little difference in the shapes of the tails.

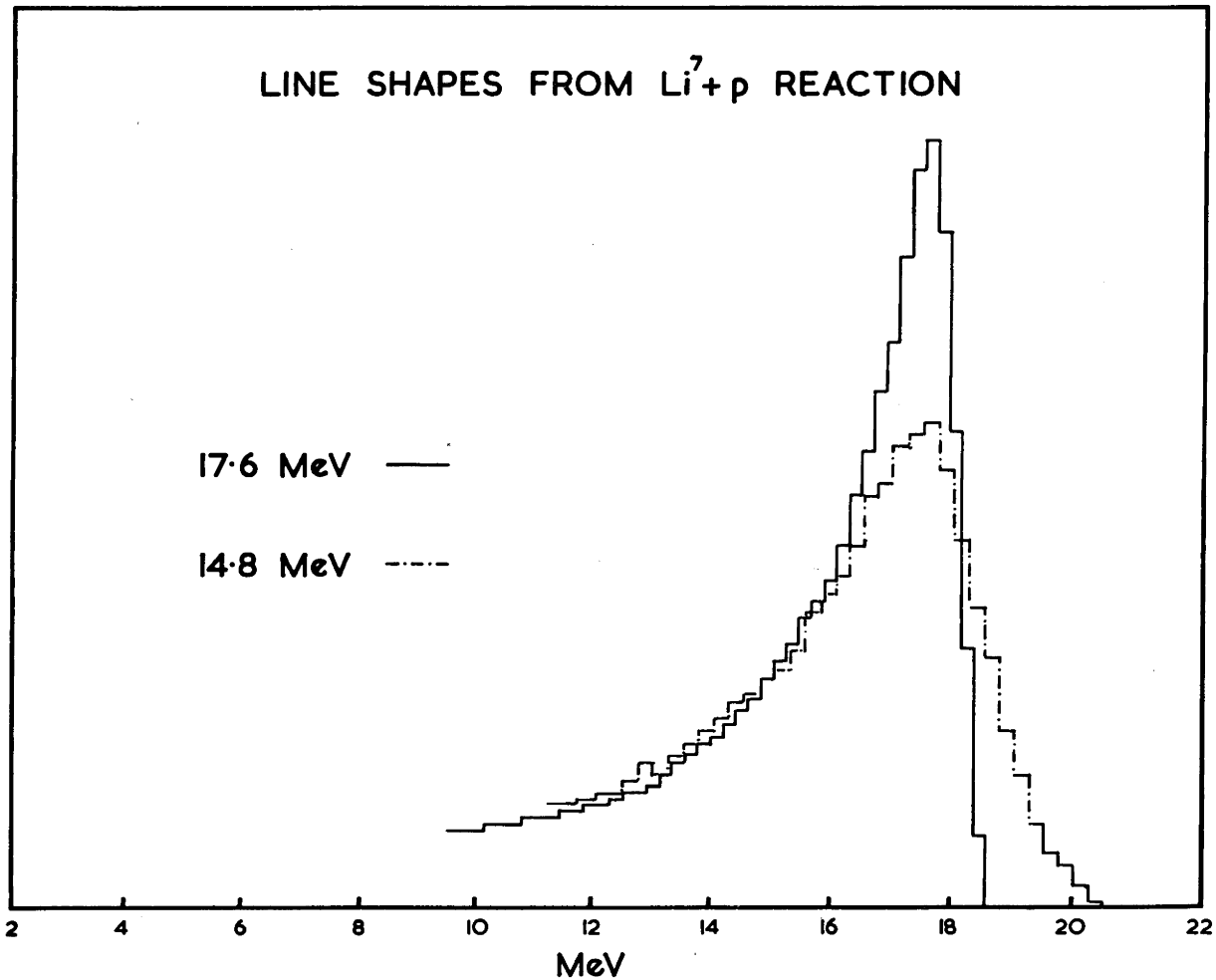
LINE SHAPES FROM Li^7 + p REACTION
17·6 MeV
14·8 MeV
2
4
6
8
10
12
14
16
18
20
22
MeV

Figure 6

Spectra from the $B^{11}(p,\gamma)$ Reaction

The increase in the proportion of 16.7 MeV radiation with proton bombarding energy is seen.

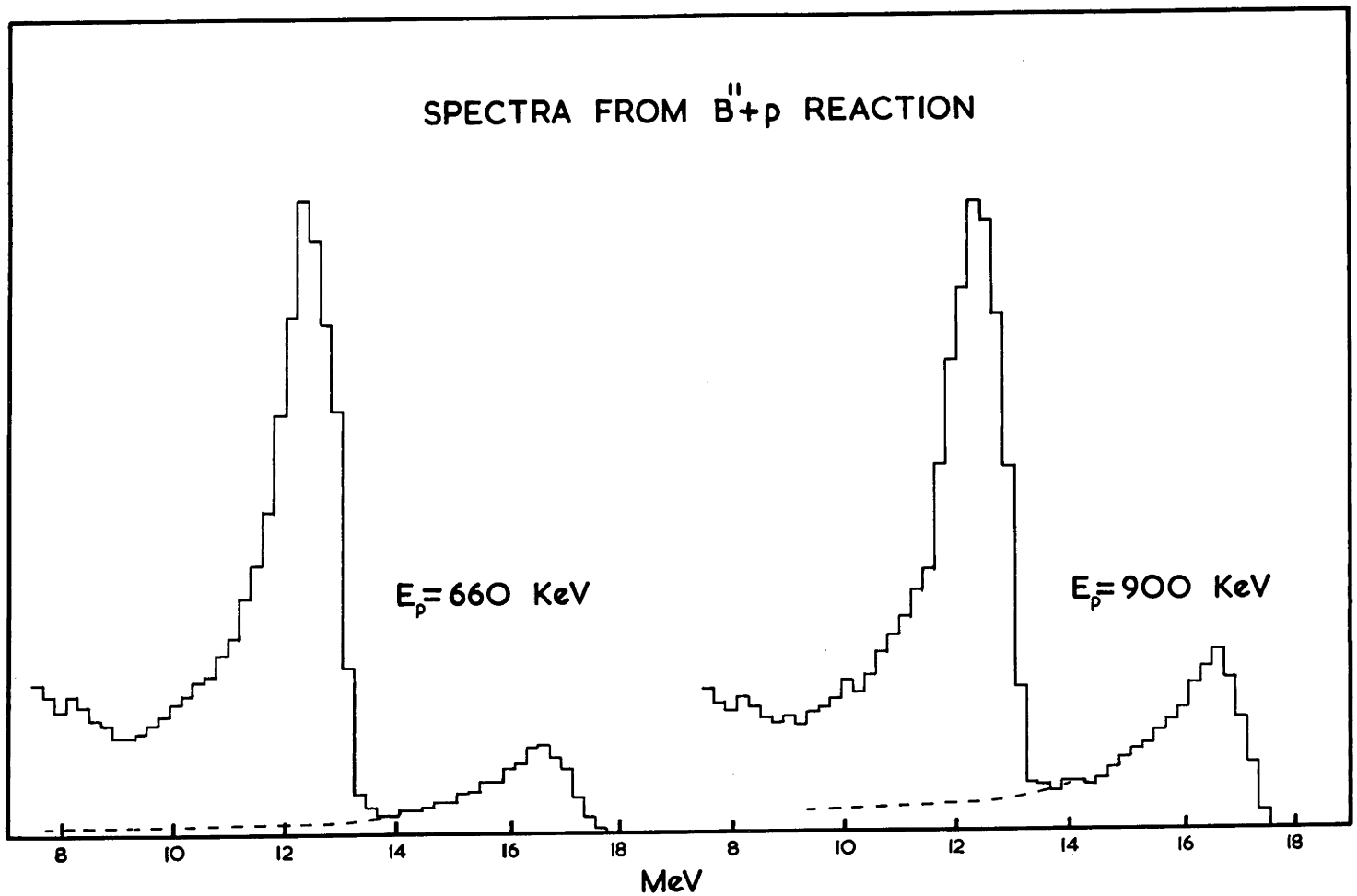
SPECTRA FROM $B^{11}+p$ REACTION
E_p= 660 KeV
E_p= 900 KeV
8
10
12
14
16
18
8
10
12
14
16
18
MeV

background. From the constancy of the line-shape we can say that for each γ-ray the resulting area is a constant fraction of the intensity, once correction has been made for the slight change of NaI absorption coefficient with energy. Hence these areas give relative intensities directly. The line-shape down to zero energy need not be known; the method merely assumes that it is the same in each case.

2.2.1 Relative Intensities of the Gamma Rays

The 17.6:14.8 MeV ratio for resonant radiation was 1.94 ± 0.1, obtained from the analysis of (8) spectra. As the shape of the upper edge of the 14.8 line is not known very accurately a systematic error could arise in the normalization process; the quoted error allows for this and is believed to be a maximum value. This result agrees well with that of Devons and Lindsay (De 50), but is higher than the figure 1.7 ± 0.2 given by Stearns and McDaniel (St 51). A recent measurement by Mainsbridge (Ma 60) using a target 5 keV thick gave the result 2.30 ± 0.04. This is consistent with the present work, in which there would certainly be a non-resonant contribution.

The ratio for non-resonant radiation could be measured to 5% for any given conditions, but its value depended on the target used and the beam energy. The approximate value of 0.53 agrees well with the figure 0.54 ± 0.08 found by Mainsbridge with a 20 keV target. He found that this ratio showed only slight

variation from 700 keV to 1 MeV.

The ratio of the 12.2 to 16.7 MeV peaks of the boron radiation was 5.62 ± 0.1 for $E_p = 660$ keV and 2.76 ± 0.05 at 900 keV, in reasonable agreement with the data of Gove and Paul (Go 55).

2.3 Edge Penetration in Collimator

In the measurement of the absolute cross section, it was necessary to know the effective aperture A of the gamma-ray collimator. This is larger than the geometrical aperture G, owing to penetration of the edges of the hole by the radiation. The relationship between A and G was studied theoretically by Mather (Ma 57) and by Cook (Co 59), and some experiments with low-energy γ-rays have been done (To 57, He 58). As the present setup did not satisfy all the conditions assumed in the theoretical work, an experimental study was made.

Figure 7 shows schematically the arrangement. Mather treats the problem exactly, using the assumption that any gamma-ray which has an interaction in the collimator material is not detected. This will naturally hold much better for low- than for high-energy radiation. He obtained the following approximation:

$$\frac{A}{G} = 1 + \frac{2}{\mu d} + \frac{2}{(\mu d)^2} ,$$

where μ is the attentuation coefficient of the collimator material. For the standard arrangement in the present work μd is ~ 30, so

Figure 7

Collimator Edge-effect

The geometrical arrangement and experimental results are shown for a 9/16 in. diameter collimator. N is the ratio of the counting rate in the crystal to that in a fixed monitor crystal. After normalization to unit intercept, the slope of the line gives the magnitude of the correction as a function of d.

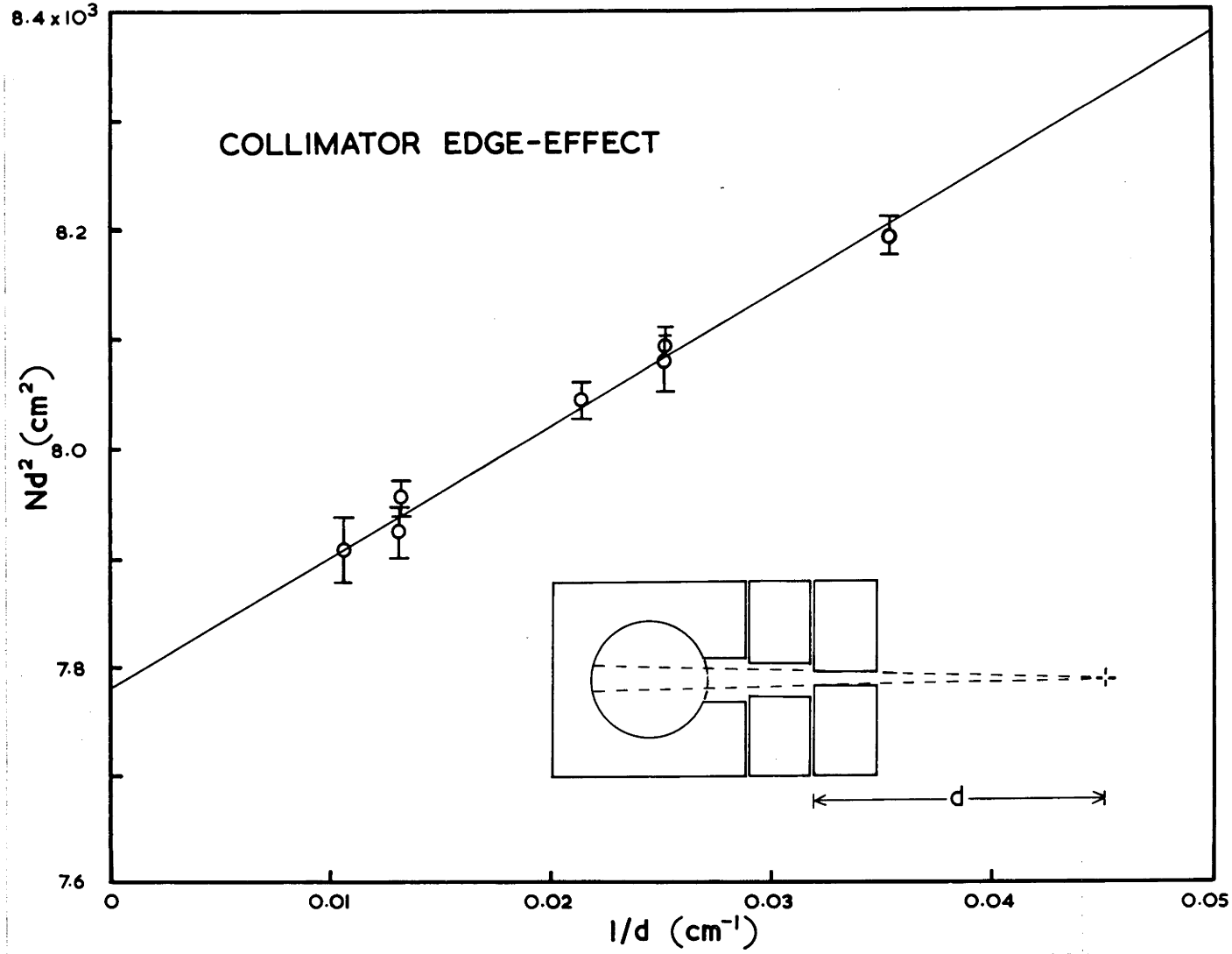
COLLIMATOR EDGE-EFFECT
8.4 x 10^3
8.2
8.0
7.8
7.6
Nd^2 (cm^2)
0
0.01
0.02
0.03
0.04
0.05
1/d (cm^-1)
d

the third term is negligible and we require only the effective coefficient of $\frac{1}{d}$.

The usual tapered collimator was replaced by one with a 9/16 in. diameter straight hole, to make the geometrical aperture more definite, and the further 2 in. diameter collimator was to reduce to a negligible value transmission through the lead itself. The whole arrangement was mounted on a trolley so that the distance d could be easily varied, while a similar fixed monitor crystal was placed at 30° to the beam. The ratio N of the pulses above 9.5 MeV in the two crystals was recorded as a function of d, for the resonance radiation. A plot of Nd^2 against $\frac{1}{d}$ is shown in figure 7; this was then normalized to unit intercept at $\frac{1}{d} = 0$, (i.e. for $d = \infty$ there is no edge penetration and A = G). This graph showed that A and G were related by

$$\frac{A}{G} = 1 + \frac{1.65}{d} ,$$

where d is in cm. Thus for the absolute cross section measurement (d = 40 cm.) the geometrical aperture is to be increased by 4%.

The factor 1.65 is smaller than that of $\frac{2}{\mu}$ (= 2.9) predicted by Mather's theory, i.e. we are getting less edge penetration than expected. This is probably (partly) because photons passing through the edge have a shorter path in the crystal and a smaller chance of being detected.

2.4 Low-energy Region of Line-Shape

Determination of the $Cu^{63}(\gamma,n)$ cross section required a knowledge of the efficiency of the monitor crystal. As the γ-ray attentuation coefficients of NaI are well-known (Gr 57) and as the γ-rays were narrowly collimated through the centre, the fraction which have an interaction in the crystal can be calculated. It remains to ensure that each interaction has been counted, i.e. that the line shape is known down to zero energy. The rapidly rising low-energy background makes this a difficult problem below 8 MeV.

Koch and Wyckoff (Ko 58) review the methods for measuring response functions of such total-absorption spectrometers, including the use of γ-ray sources, monoergic electron data and bremsstrahlung. In one of their experiments (Ko 56) experimentally determined pulse-height distributions from monoergic electrons incident on a 5" diam. and 9" long NaI crystal were used to build up a response function. This method is more suitable for high energies ($\sim$ 100 MeV) where the photon and electron shower production characteristics are very similar. Their results for 19 MeV electrons, modified to allow for the differences at this energy, indicated a response curve which became very small below 8 MeV.

A Monte Carlo calculation of the energy loss spectra in NaI crystals was made by Campbell and Boyle (Ca 53) and more recently

by Miller et al. (Mi 61). The nearest comparison from their work is for a narrowly collimated beam of 11.7 MeV photons incident on a 5 in. diameter by 7.25 in. crystal. Their spectrum, when modified by the resolution characteristics of the system, also indicates a line shape which is small below 8 MeV. Their calculation assumes perfect light-collection from all parts of the crystal, which will not hold in practice. As the pair-production cross section increases 1½ times from 10 to 20 MeV this could also change the response function significantly.

An experimental study using γ-rays from proton bombardment of F^{19}, Li^{7}, B^{11} and H^{3} was made by Kockum and Starfelt (Ko 59). They used two 5" x 4" NaI crystals back to back, each with its own phototube. However, their collimator was wide (1½ in.), the backgrounds were high and the low-energy portion of the spectra was not studied adequately for the present purpose. It was decided to improve on their work by placing more emphasis on reduction of the low-energy background.

Contributions to this background are the following: (a) Gamma ray showers through the collimator slab; (b) Scattering from the sides of the coolimator-hole; (c) Gamma-rays from neutron capture in the crystal; (d) Background from cosmic rays and from decay of I^{128} (formed by the $I^{127}(n,\gamma)$ reaction in the crystal).

The investigation was made with the arrangement of figure 7, except that two further collimators of wider bore were placed in

Figure 8

Contributions to Spectrum of the lithium radiation

A is the original spectrum and D the natural background. For description of B and C see P.44.

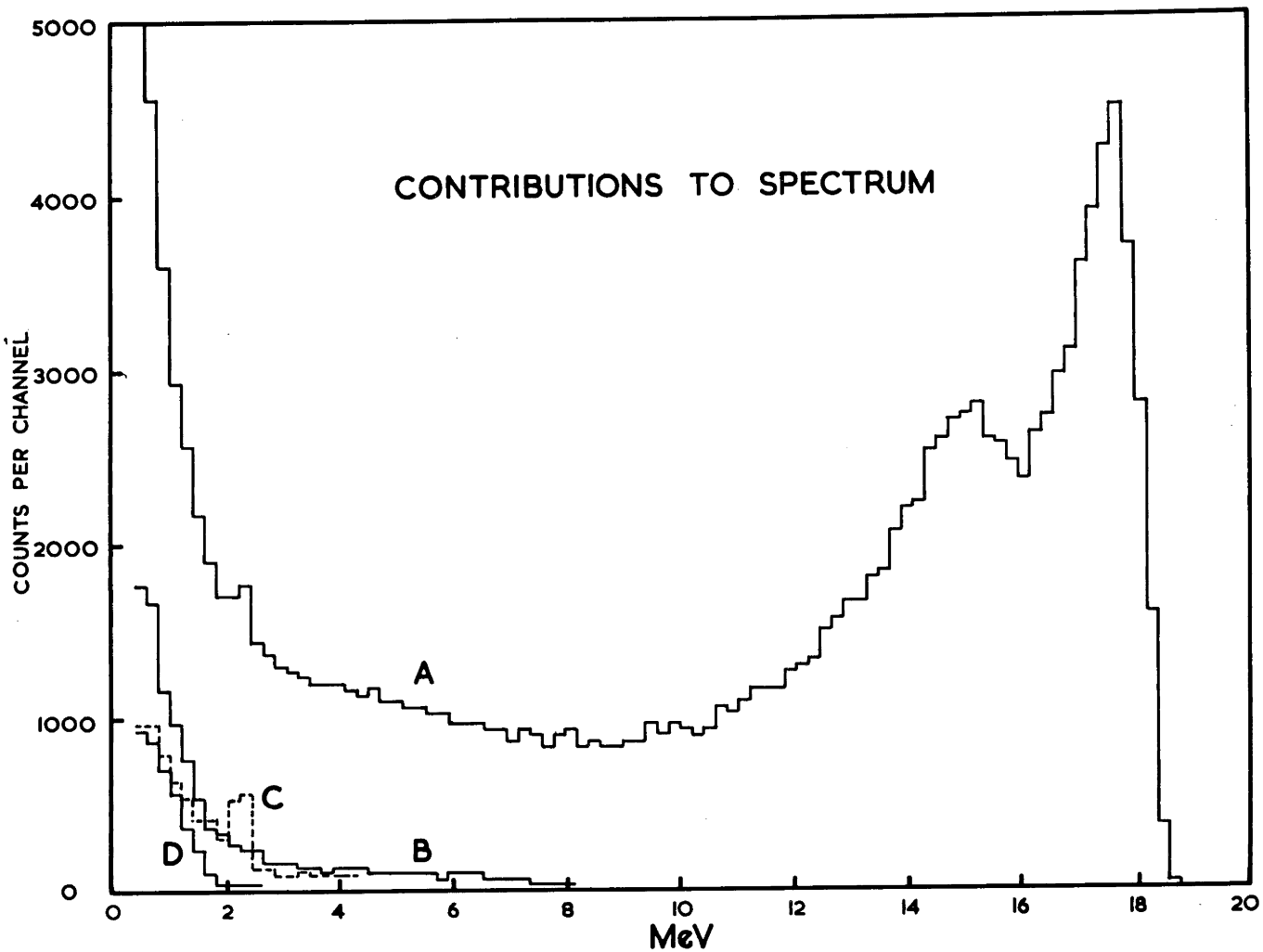
CONTRIBUTIONS TO SPECTRUM
COUNTS PER CHANNEL
5000
4000
3000
2000
1000
0
0
2
4
6
8
10
12
14
16
18
20
MeV
A
B
C
D

Figure 9

Low-Energy region of line-shape

B is the spectrum taken with very good collimation and C the resulting spectrum when backgrounds have been subtracted. Some possible low-energy extrapolations, 1, 2 and 3, are shown.

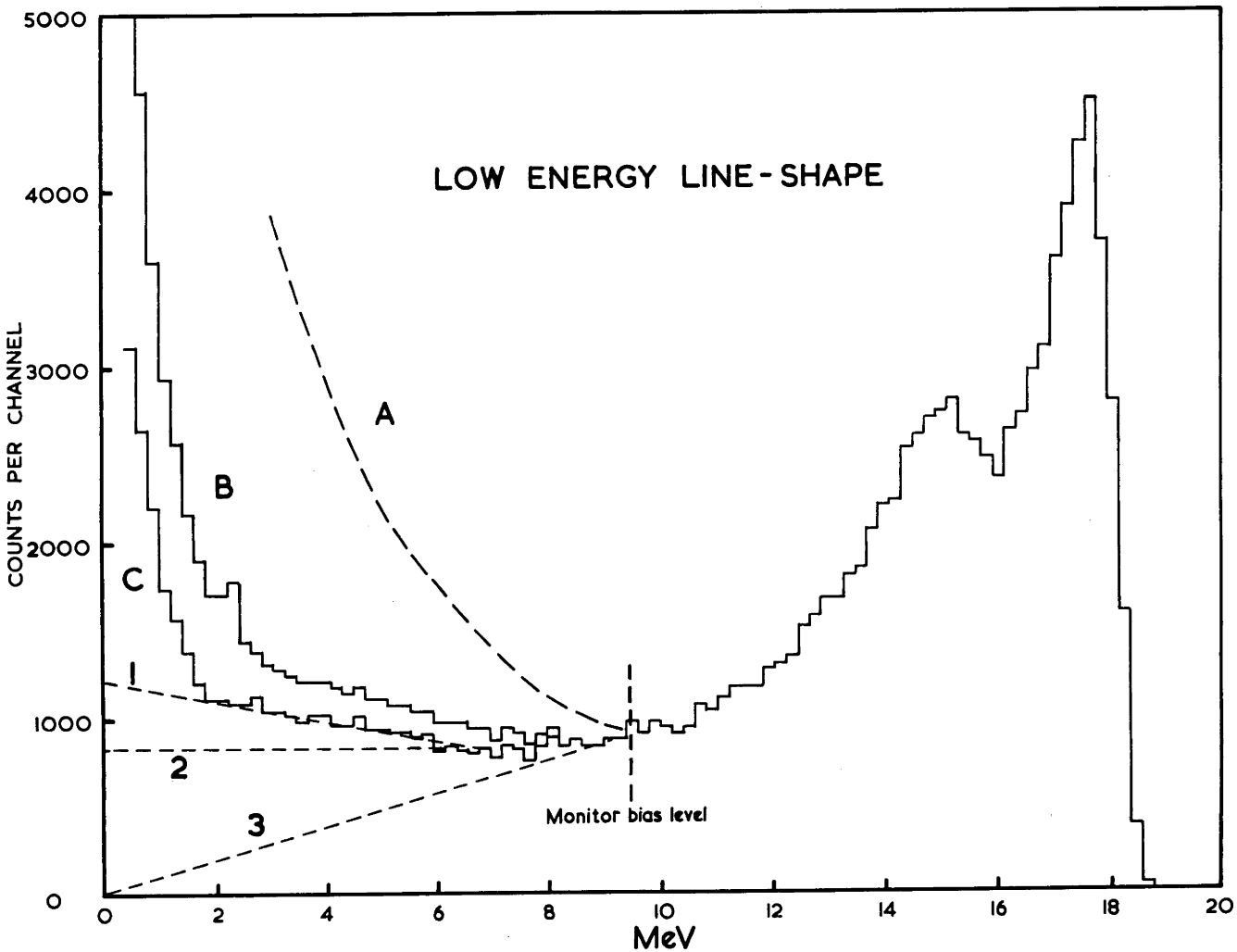
LOW ENERGY LINE-SHAPE
COUNTS PER CHANNEL
5000
4000
3000
2000
1000
0
A
B
C
1
2
3
Monitor bias level
0
2
4
6
8
10
12
14
16
18
20
MeV

front, to give a total thickness of 12 in. of lead. The crystal was shielded with 6 in. of lead, and the distance d was again 40 cm.

In figure 8 each spectrum was taken for a kicksorter "live" time of 15 min. Spectrum A was taken under normal conditions and had a counting loss of 8%. For B, the collimator was blocked with a 6 in. long lead plug so that no γ-rays could enter the crystal; most of this spectrum comes therefore from neutron capture. The lead plug was removed and the lithium target replaced by a "blank target" having only a layer of carbon from previous running, so that from spectrum C was obtained the background due to the 4.43 MeV γ-ray from $C^{12}(p,\gamma)N^{13}$. Finally, spectrum D is the cosmic ray background; counts from decay of I^{128} were detectable but less than 5% of this.

The final spectrum corrected for the various backgrounds, (A - B) - (C - D), is shown as spectrum C in figure 9. The great importance of a thick collimator is seen by comparing B and A in this figure, taken with lead thickness 12 in. and 3 in., respectively. Although very few of the γ-rays penetrate the lead they can be detected over the whole face of the crystal.

This procedure has not subtracted the background due to photons scattered from the collimator. If this is significant the proportion of low-energy counts should change with the distance d. Spectra from the edge-penetration experiment were summed over the regions A (4 to 8 MeV) and B (10 to 19 MeV), and the ratio

Figure 10

Test for Scattering by Collimator

The ratio of the counting rates in energy regions A and B is plotted against 1/d (see figure 7). If scattering were important in region A the points would lie on a line with positive slope.

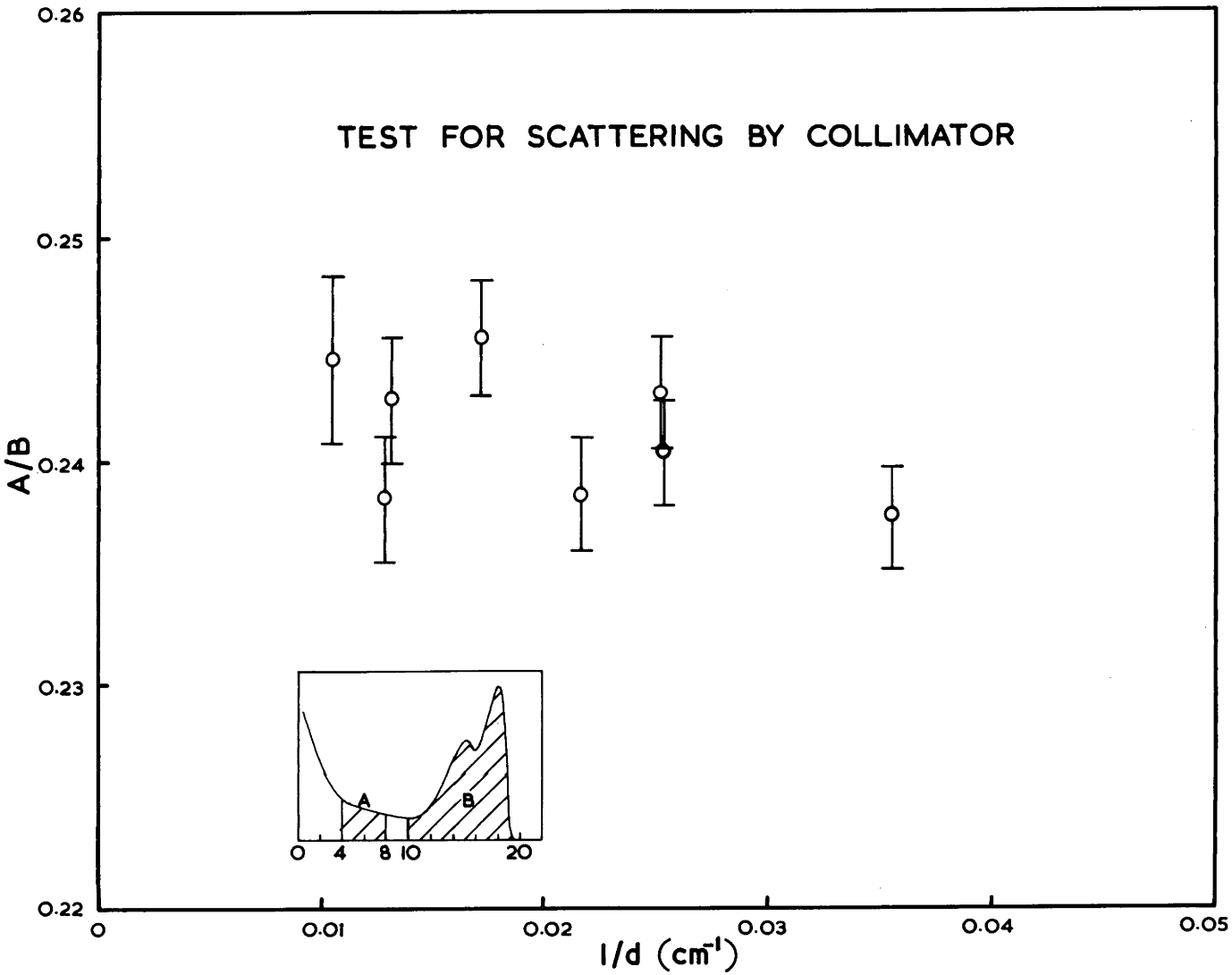
TEST FOR SCATTERING BY COLLIMATOR
A/B
0.26
0.25
0.24
0.23
0.22
0
0.01
0.02
0.03
0.04
0.05
1/d (cm⁻¹)
A
B
0
4
8
10
20

$\frac{A}{B}$ plotted against $\frac{1}{d}$ in figure 10. There is no tendency for $\frac{A}{B}$ to decrease with d as would be expected if scattering were important; it seems unlikely, therefore, that at the standard distance the contribution to region A from scattering is more than a few per cent.

Although these methods have still not reduced the background as much as desired, it seems to be a reasonable assumption that the curve can be extended horizontally (extrapolation 2 of figure 9). Extrapolation 3 would require collimator scattering to contribute about 25% of the total between 4 and 8 MeV and seems to be ruled out by the present work.

3. Absolute Cross Section for the Lithium Resonance Radiation

3.1 Experimental Method

A $\frac{3}{4}$ in. diameter by $\frac{1}{8}$ in. copper disk was held 0.60 in. from the target in a light aluminium jig (C of figure 1), and irradiated for twenty minutes. It was then sandwiched between two $\frac{1}{16}$ in. thick copper disks, to localize the positron annihilation, and placed between two closely-spaced NaI crystals as shown in figure 11. The crystals (5 in. x 4 in. and 3 in. x 3 in.) were shielded on all sides by 3 in. of lead. Two independent determinations of the activity were made by measuring the 0.51 MeV photopeak in each crystal. The Cu^{62} activity was followed for 30 minutes and a correction ($\sim$ 0.3%) for the Cu^{64}

Figure 11

Efficiency Calibration of NaI crystals

The geometrical arrangements and a typical spectrum in each crystal are shown. B was the geometry for counting of residual activity, and A and C were arrangements allowing measurement of absorption corrections.

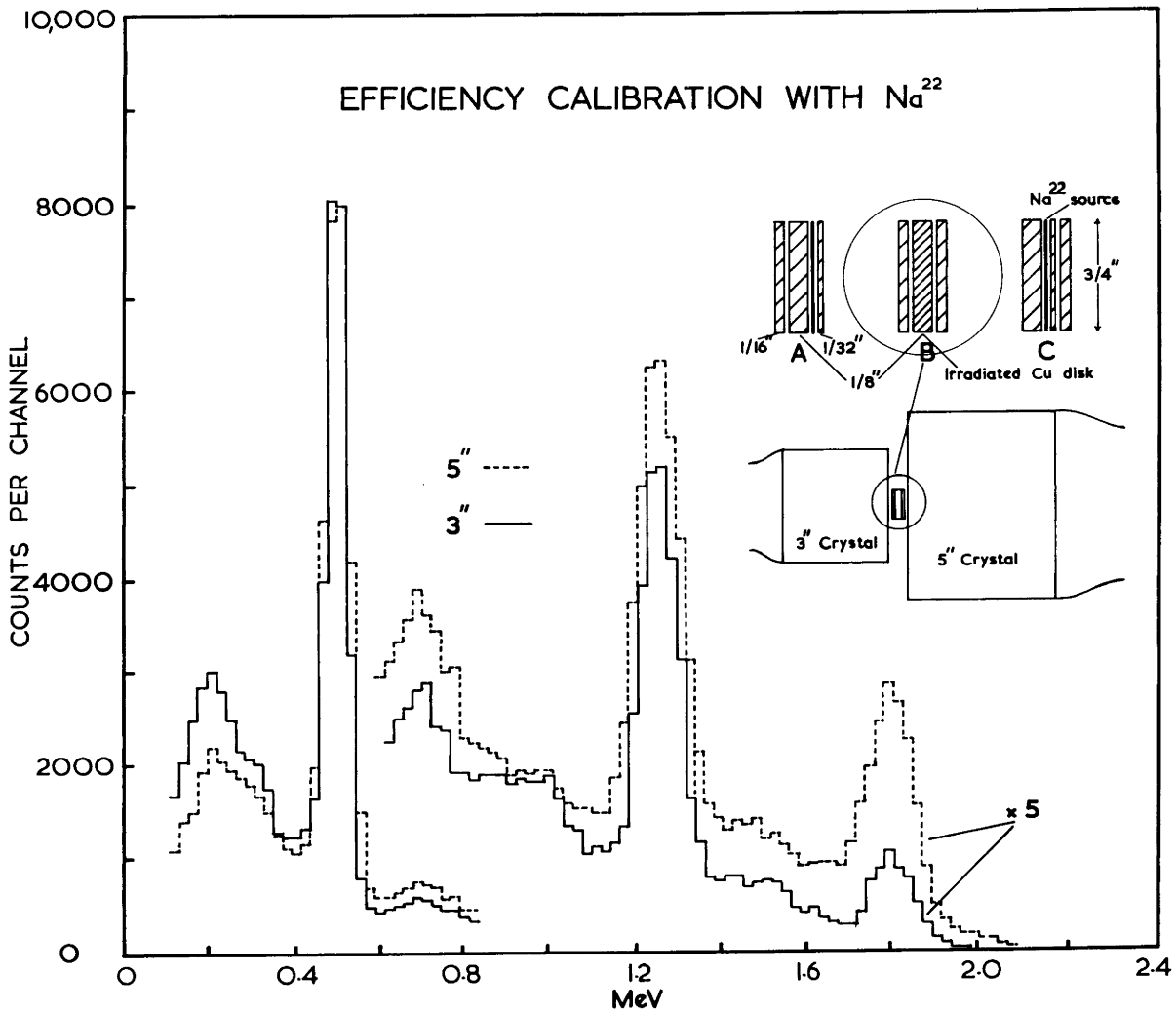
EFFICIENCY CALIBRATION WITH Na22
COUNTS PER CHANNEL
10,000
8000
6000
4000
2000
0
0
0.4
0.8
1.2
1.6
2.0
2.4
MeV
5"
3"
x 5
Na22 source
3/4"
1/16"
A
1/32"
1/8"
B
C
Irradiated Cu disk
3" Crystal
5" Crystal

activity applied using a measurement six hours later. Three separate irradiations were carried out.

The efficiency of each crystal for the annihilation radiation was determined with a standard Na^{22} source, made from a solution calibrated by the National Bureau of Standards, Washington, to an accuracy of 2%. The source was prepared by micro-pipetting 0.1 ml (or 15,000 β^+/min.) of the solution on to a disk of filter paper; this was glued when dry between 0.01 in. thick copper disks. Two such sources prepared from different batches of the standard solution agreed in activity to within 1%. The effect of self-absorption was studied by counting the activity with the source placed successively in arrangements A and C, then in each reversed. The mean of the four counts in each crystal was then equivalent to that from an activated $\frac{1}{8}$ in. disk.

3.2 Analysis and Results

As the 1.28 MeV γ-ray from Na^{22} occurs in coincidence with the positron in over 99% of disintegrations corrections were required in the calculation of the detection efficiencies. The count in the 0.51 photopeak was corrected for: (1) counts from the tail of the 1.28 γ-ray, (2) pulses lost due to coincident detection of an annihilation quantum and the γ-ray. Correction (1) was estimated by summing the appropriate pulses under the extrapolation of the 1.28 MeV peak (typical spectra are shown

in figure 11). For the second correction term the total in the sum-peak was divided by the photofraction for the 1.28 MeV γ, obtained from the tables of Miller et al. (Mi 58).

The corrections were -8% and +14% respectively for the 3 in. crystal and -6% and +27% for the larger crystal. Uncertainty in these corrections was the largest source of error in the Cu^{62} activity measurement, for which an overall accuracy of 5% was estimated. The consistency of the results from the two crystals was much better than this, as the two measurements agreed to within 0.4%. The distance from target to copper sample was known to better than 0.001 in.; geometrical and statistical errors in the cross section measurement were much less than the uncertainty in the crystal efficiencies.

Corrections were applied for the absorption of lithium γ-rays in the sample (5.8%), electron capture in Cu^{62} (1.8%), and edge-penetration in the collimator (3.9%). The total activity induced in the sample in terms of the incident flux was calculated by an integration over the disk as in Appendix A. The attenuation coefficient of NaI was obtained from the tables of Grodstein (Gr 57), and the half-lives adopted were 2.585 ± 0.006 y for Na^{22} (Ga 60) and 9.9 ± 0.1 min. for Cu^{62}.

If the tail of the γ-ray response function is assumed to be horizontal, (extrapolation 2 of figure 9) the cross section is 59 ± 3 mb. A tail following extrapolation 1 gives a lower limit of 56 ± 3 mb. Although it would appear to be ruled out by the

present measurements a response shape following extrapolation 3 would give a cross section of 68 mb.

In view of the present uncertainty in the low-energy response function the value 59 ± 6 mb was adopted.

4. Cross Section as a Function of Photon Energy

4.1 Experimental Method

Measurements were made of the relative activities of copper disks after irradiation with the resonance and non-resonance radiations from lithium, and with the radiations from boron bombarded with protons of 660 and 900 keV. The copper disks were $\frac{3}{4}$ in. diameter by $\frac{1}{4}$ in. They were irradiated in jig A (figure 1), with the front face of the sample 0.16 in. from the target, although for some pairs of lithium irradiations jig C was used; such "good geometry" measurements were to provide a check on the corrections for anisotropy of the non-resonant radiation. For each target bombardments at the two energies followed in fairly close succession, with an angular distribution taken after each. Residual activities were measured with a 3 in. NaI crystal, using a standard sequence of irradiation and counting times. Figures for the activity induced per monitor-count were reproducible to better than 1%.

For the lithium non-resonant radiation the corrections for anisotropy were 7% for the close-up geometry and 2% for the better geometry. The resulting yield ratios at the two positions gave

good agreement. Anisotropy corrections to the boron measurements were 4% at 660 keV and 3% at 900 keV.

4.2 Analysis and Results

The symbols σ and α will be used respectively for cross section and for intensity ratio of high-energy to low-energy γ-ray component. Subscripts R, N, L, H refer to the type of radiation: lithium resonance and non resonance; boron "low" (660 keV) and "high" (900 keV) respectively. The symbols k_1, k_2, k_3, k_4 represent the ratios $\sigma_{15.02}/\sigma_{14.73}$, $\sigma_{17.99}/\sigma_{17.63}$, $\sigma_{12.33}/\sigma_{12.11}$, $\sigma_{16.74}/\sigma_{16.54}$ respectively; these terms must be included because the γ-ray energies increase with E_p as shown in Table 1.

The experimental results were the following (including data from two sets of runs on lithium):

A. $\sigma_N/\sigma_R = 0.82 \pm 0.02$, $\alpha_R = 1.93 \pm 0.10$, $\alpha_N = 0.51 \pm 0.03$

B. $\sigma_N/\sigma_R = 0.84 \pm 0.02$, $\alpha_R = 1.93 \pm 0.10$, $\alpha_N = 0.53 \pm 0.03$

$\sigma_H/\sigma_R = 0.44 \pm 0.01$, $\sigma_L/\sigma_R = 0.311 \pm 0.007$,

$\alpha_L = 0.178 \pm 0.003$, $\alpha_H = 0.363 \pm 0.004$.

It can be easily shown that the following relations hold:

$$\sigma_{17.6}/\sigma_R = \frac{(\alpha_N + 1)\sigma_N/\sigma_R - k_1 (\alpha_R + 1)}{k_2 \alpha_N - k_1 \alpha_R} \qquad (1)$$

$$\sigma_{14.8}/\sigma_R = \frac{k_2 \alpha_N (\alpha_R + 1) - \alpha_R(\alpha_N + 1) \sigma_N/\sigma_R}{k_2 \alpha_N - k_1 \alpha_R} \qquad (2)$$

Figure 12

Excitation Function from Successive Approximations

The first four approximations are shown; a fifth gives no significant change.

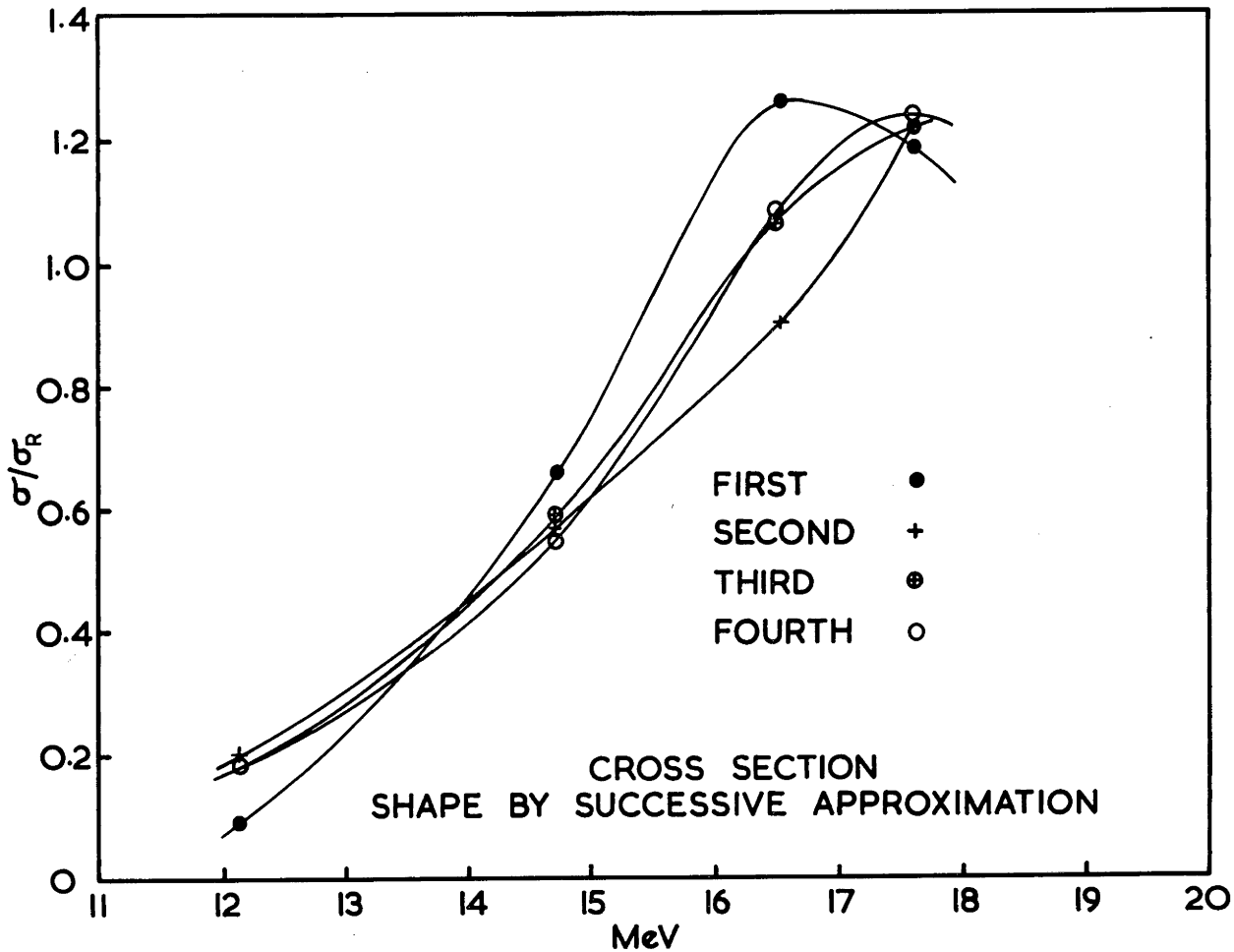
1.4
1.2
1.0
0.8
0.6
0.4
0.2
0
σ/σR
11
12
13
14
15
16
17
18
19
20
MeV
FIRST
SECOND
THIRD
FOURTH
CROSS SECTION
SHAPE BY SUCCESSIVE APPROXIMATION

$$\sigma_{16.7}/\sigma_R = \frac{(a_H + 1)\sigma_H/\sigma_R - k_3 (a_L + 1)\ \sigma_L/\sigma_R}{k_4\ a_H - k_3\ a_L} \qquad (3)$$

$$\sigma_{12.2}/\sigma_R = \frac{k_4\ a_H\ (a_L + 1)\sigma_L/\sigma_R - a_L\ (a_H + 1)\sigma_H/\sigma_R}{k_4\ a_H - k_3} \ . \qquad (4)$$

There are two possible ways of applying these equations - values for k_1, k_2, k_3 and k_4 can be taken from bremsstrahlung cross section curves, or a method of successive approximations applied using only the present data. Both methods were used.

Values of the constants taken from the curves of Katz and Cameron (Ka 51) and Berman and Brown (Be 54) were $k_1 = 1.13$, $k_2 = 1.00$ (i.e. curve peaked at 17.6 MeV), $k_3 = 1.10$, $k_4 = 1.06$. In the successive approximation method the k's were first each put equal to 1; from the resulting curve improved values were found and the calculation repeated. Although the first approximation is poor the convergence is rapid, and figure 12 shows that the third and fourth trials differ very little. The only external data put into this calculation was in the fourth step, when the curve was assumed to peak at 17.6 MeV. The results which follow give the cross section at each energy as a fraction of σ_R. The figures from the successive approximation method are given in parentheses; the agreement is very good.

12.1 MeV, 0.18 (0.18) $\pm$ 0.03; 14.8 MeV, 0.56 (0.54) $\pm$ 0.04;

16.5 MeV, 1.06 (1.08) $\pm$ 0.07; 17.6 MeV, 1.23 (1.23) $\pm$ 0.03.

A calculation using the shape near 15 MeV found by Berman and Brown showed that the width of the 14.8 MeV line gave it an

Figure 13

Cross Section for $Cu^{63}(\gamma,n)Cu^{62}$

The excitation function from the present work is compared with that of Berman and Brown. The error bars shown do not include the uncertainty in the absolute cross section. The dotted lines show the Berman and Brown result, normalized at 17.6 MeV.

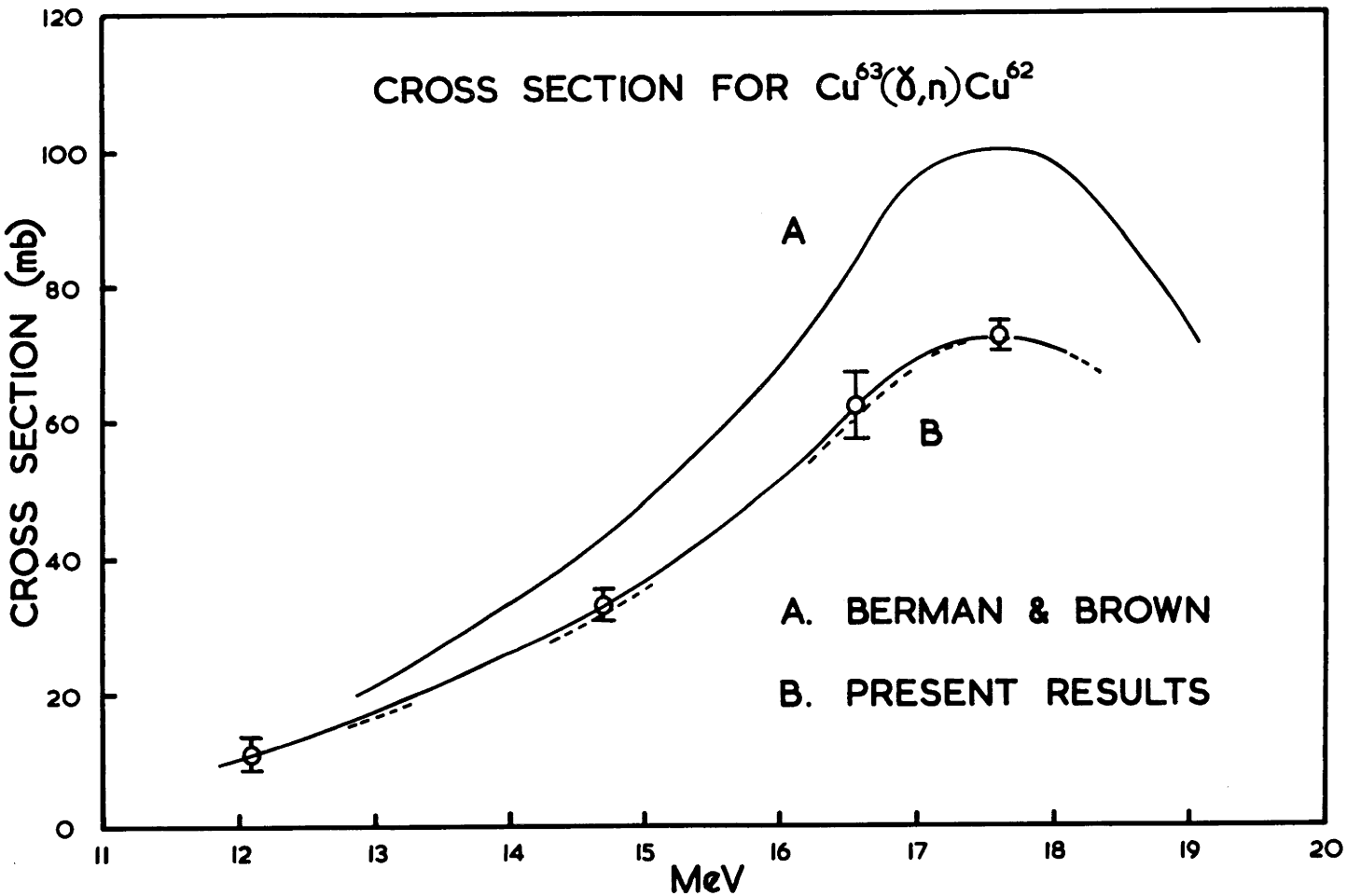
CROSS SECTION FOR $Cu^{63}(\gamma,n)Cu^{62}$
CROSS SECTION (mb)
120
100
80
60
40
20
0
11
12
13
14
15
16
17
18
19
20
MeV
A
B
A. BERMAN & BROWN
B. PRESENT RESULTS

effective energy about 120 keV higher than its nominal energy. Although this does not affect the above calculations within their present accuracy it means that the cross section has been measured at about 14.85 MeV.

If we take σ_R to be 59 ± 6 mb, the cross sections become:

12.1 MeV 11 ± 2 mb; 14.8 MeV 33 ± 4 mb;

16.5 MeV 63 ± 8 mb; 17.6 MeV 73 ± 8 mb.

Comparison with the shape found by Berman and Brown is made in figure 13, where the error bars do not include the error in the absolute cross section. The dotted lines show the other curve normalized at 17.6 MeV.

5. Discussion

5.1 Comparison with Previous Work

A useful way to compare the lithium and bremsstrahlung measurements is to obtain from the cross section curves an effective resonance radiation cross section; adopting $\sigma_R = 1.94$ we calculate

$$\sigma_R = 0.66\ \sigma_{17.6} + 0.34\ \sigma_{14.8}\ ,$$

to be compared with the present result of 59 ± 6 mb. Figures from experiments using neutron detection are further corrected for neutrons from Cu^{65}, using $\sigma_R(Cu^{65})/\sigma_R(Cu^{63}) = 1.19 \pm 0.03$ (obtained in Chapter 3). Tables 2 and 3 summarize results from the two types of measurement.

Table 2 Bremsstrahlung Measurements of $Cu^{63}(\gamma,n)Cu^{62}$ Cross Section

Reference		$E_{max.}$ (MeV)	$\sigma_{max.}$ (mb)	Half-width (MeV)	$\sigma_{int.}$ (MeV-barn)	σ_R (mb)	X-ray Intensity Measurement	Measurement of activity
A. Activation Measurements (Cu^{63})								
Diven & Almy	(Di 50)	17.5	100	5.6	0.6	86	R-meter	β+ End-window G.M. Counter
Katz & Cameron [a]	(Ka 51)	18.1	94	6.1	0.60	79	R-meter	β+ G.M. Counter
Byerly & Stephens	(By 51)	17.5	100	5.3		80	R-meter	β+ G.M. Counter
Krohn & Shrader	(Kr 52)	17.0	94	5.1		76	Pair spectrometer	β+ End-window G.M. Counter
Berman & Brown	(Be 54)	17.5	98	4.9	0.55 ± 0.03	80	Electron current	β+ 4π Scintillation Counter
Scott, Hanson & Kerst	(Sc 55)	16.7	80	4.9	0.41	68	Electron current	β+ 4π Scintillation Counter
Roalsvig et al. [b]	(Ro 59)		93			79	R-meter	β+ Flow Proportional Counter
Haslam & Gupta [c]	(Ha 61)	18.0	80	8 MeV		66	R-meter	β+ Flow Proportional Counter
B. Neutron detection measurement (Natural Cu)								
Gavrilov & Lazarova	(Ga 57)	17.2	126	4.3	0.93	102 (Cu) 96 (Cu^{63})	Thick-walled Al BF_3 + paraffin Ionization Chamber	

σ_R is the cross section for the same mixture of gamma rays as the lithium resonance radiation.

(a) Their published cross section has here been reduced by 10%, in accordance with their later statements (Ry 58).

(b) Re-measurement of the absolute yield as given by Katz and Cameron.

(c) The cross section has been obtained from the yield curve via the Leiss-Penfold tables. See discussion, P. 55. The absolute normalization is that of Roalsvig et al.

Table 3

Measurements of $Cu^{63}(\gamma,n)Cu^{62}$ Cross Section with the Lithium Radiation

	σ_R (Natural Cu) (mb)	σ_R (Cu^{63}) (mb)	γ-ray Monitoring	Activity Measurement	Neutron Detection
Wäffler & Hirzel (Wa 48)		120 ± 30	G.M. Counter	G.M. Counter	
Shimizu (Sh 49)		29*	G.M. Counter	G.M. Counter	
McDaniel, Walker & Stearns (Mc 50)	55 ± 12	52 ± 11	G.M. Counter		BF_3+ paraffin
Glattli, Seippel & Stoll (Gl 52)		48 ± 8	G.M. Counter	G.M. Counter	
Hartley, Stephens & Winhold (Ha 56)	64 ± 10	60 ± 9	Small NaI crystal		BF_3+ paraffin
Carver & Kondaiah (Ca 54)	85 ± 15	80 ± 14	G.M. Counter		Szilard-Chalmers
Nakamura et al. (Na 59)		38 ± 6	G.M. Counter	G.M. Counter	
Yasumi et al. (Ya 60)		62 ± 4	G.M. Counter; NaI crystal	G.M. Counter & 4π flow counter	
Present work		59 ± 6	NaI crystal	NaI crystal	

* As recalculated by Nakamura et al.

Except for that of Scott et al. and the recent result of Haslam, the bremsstrahlung experiments using activation techniques all give σ_R close to 80 mb. The lower result of the former group is of interest as their methods were almost identical with those of Berman and Brown. They did not suggest any reason for the 15% difference, but it is probable that it arose in the β-counting arrangements. Roalsvig redetermined the yield from Cu^{63} at 22 MeV, using a proportional flow-counter. His result was 10% lower than the original published value of Katz and Cameron, therefore agrees well with their revised value. The result of Haslam raises new questions and will be discussed below. The only experiment in which a calibrated neutron detector was used gave a rather higher cross section; this is probably due to the difficulty of calibrating the neutron counter.

Of the results with lithium radiation, those of McDaniel et al., Hartley et al. and Yasumi et al. are in good agreement with the present result, while that of Carver and Kondaiah is close to the bremsstrahlung value.

The Japanese workers rejected their previous results and have confidence in their recent measurement. The γ-ray monitor was a large end-window geiger counter, calibrated by using lead-foil converters at the centre of a flow-type 4π geiger counter. Positrons from Cu^{62} were also detected by an end window geiger, calibrated against a 4π gas-flow counter. By using very thin

neutron-activated copper disks they were able to extrapolate accurately to zero sample thickness. The large difference from their previous result had arisen in the β-counting, even though this had been carefully done. As a second γ-ray monitor they used a 5" x 4" NaI crystal, but without a collimator, with the efficiency derived from theory. Had they adopted this calibration their cross section would have been 8% lower.

In a number of recent papers from the Saskatoon group (Ry 58, Ki 60, Ro 59) it has been stated that analysis of yield curves by the more recent Leiss-Penfold (L.P.) inverted matrix method results in cross sections which have the same shape but are $\sim$ 30% less than those given by the Katz and Cameron (K.C.) "photon difference".analysis. In view of the present results this is an attractive possibility, though the real meaning is not yet clear. The difference certainly cannot lie in the mathematical treatment - the derived cross section must reproduce the original yield curve when the inverse process is applied - hence the discrepancy must lie in the published tables or the way in which they are used. In the only discussion of the discrepancy, Rybka and Katz (Ry 58) advance two reasons: (1) Newer γ-ray absorption coefficients in lucite altered the previous calculations of the number of roentgens per erg of radiation on which the K.C. tables were based; (2) The L.P. tables were calculated using Schiff's integrated spectrum formula (Appendix D) with the screening constant C = 111, while

the older tables were based on his thin target spectrum with C = 191. The second reason must be far less important.

Haslam (private communication) also suggests that the difference has arisen in the relationship between the reading of the monitor (Victoreen thimble in lucite) and the flux through the sample. J. R. Thyer (private communication) analyzed Roalsvig's yield curve for nickel by both methods, using their original monitor response function, and obtained good agreement (justifying the higher cross sections). The monitor response function is therefore involved in this problem, but as the same function should be used in both methods of analysis the situation is still not clear. If it is decided that the lower cross sections are correct the agreement between bremsstrahlung and lithium measurements will be greatly improved. The results of Berman and Brown and of Scott et al. are in a different category; although they used the "photon difference" method they did not use the K.C. tables, owing to their different method of monitoring.

The shape obtained for the Cu^{63} cross section agrees very well with that of Berman and Brown. As other bremsstrahlung measurements of the shape are in reasonable agreement with their work, it appears that the main problem is that of normalization.

If photonuclear cross sections are to be considerably reduced in magnitude the conclusions drawn from the integrated cross sections must change, especially as to the amount of exchange

force to be included. However, as will appear in Chapter 3, even measurements of other nuclei relative to Cu^{63} are subject to large uncertainties. Until the experimental results have been considerably improved it does not seem appropriate to draw any new detailed conclusions from values of integrated cross sections.

5.2 Conclusions

These measurements with monochromatic γ-rays give a shape for the $Cu^{63}(\gamma,n)$ cross section in very good agreement with bremsstrahlung results, but suggest that the presently accepted magnitudes are 25% too high. The discrepancy is probably due to inaccuracies in absolute β-counting or in the measurement of X-ray intensity.

CHAPTER 3

CROSS SECTIONS FOR THE (γ,n) REACTION IN Cu^{65}, Zn^{64}, Sb^{121} and Pr^{141}, MEASURED WITH THE Li^{7} + p RESONANCE RADIATION

1. Introduction

It was stated in Chapter 2 that the results of measurement of the $Cu^{63}(\gamma,n)Cu^{62}$ cross section with the lithium radiation suggest that the bremsstrahlung results are too high by about 25%. We wished to find out if this was an example of a systematic error in normalization, due, e.g. to problems of X-ray intensity measurement, or whether measured cross sections could be astray in either direction because of the difficulties of β-counting or neutron detection. Using the previous methods, measurements of cross sections relative to Cu^{63} for some other isotopes were made, for comparison with synchrotron results.

The nuclides chosen for study were Cu^{65}, Zn^{64}, Sb^{121} (fraction going to 16 m ground-state only) and Pr^{141}. The photoneutron product in these isotopes is β^{+} - active with a half-life and decay scheme favourable for detection. Detection of annihilation radiation in each case makes the comparison with Cu^{63} as direct as possible; in addition, some former experiments had used direct detection of positrons from these products.

Lithium radiation was used in three series of relative measurements, but the only one using activation techniques was

that of Wäffler and Hirzel (Wa 48). McDaniel et al. (Mc 50) and Hartley et al. (Ha 56) detected photoneutrons with paraffin moderator and BF_3 counters.

Wäffler and Hirzel used geiger counters to study β^- and β^+ emission. Their measurement of the $Cu^{63}(\gamma,n)$ cross section was very high (Table 3, Chapter 2). McDaniel et al. detected the neutrons emitted from 33 elements and found that their results fluctuated much less than those of Wäffler; they assumed this was because they were measuring a weighted average over the isotopes of the element. Hartley et al. used very similar methods except in monitoring the γ-rays with a small NaI crystal. Their cross sections were about 20% higher than McDaniel's but they regarded the agreement as still satisfactory.

The general method of the present work was to detect with a small NaI crystal the annihilation radiation from the samples, after irradiation in a close-up geometry. Corrections were then made for the fraction of β^+ emission, self-absorption, and isotopic abundance.

2. Experimental Method

The samples were contained in aluminium cans $\frac{3}{4}$ in. in diameter by $\frac{1}{4}$ in., with wall thickness 250 mg/cm^2. The zinc and antimony were Analar-grade powders, the copper solid metal, and the praseodymium was a compressed disk of PrF_3. They were irradiated

in the close-up geometry (jig A) for the following times: Pr, 6 m, Cu^{65} 4 h, Cu^{63} 10 m, Sb 15 m, Zn 20 m. The monitor count was recorded at intervals but the flux was usually constant to within 5%. In the Cu^{64} runs the intensity dropped as the target deteriorated, but the corrections needed were less than 1%.

The annihilation radiation was detected with a spectrometer consisting of a $1\frac{1}{2}$" x $1\frac{1}{2}$" Harshaw NaI(Tl) crystal on a Dumont 6292 phototube, contained in a lead castle with walls 3 in. thick. The sample was held close to the crystal in a brass jig with walls 0.12 in. thick, to localize the positron annihilation. The photopeak totals on the kicksorter screen were corrected for background and counting loss, using a dead time of 850 μs. Spectra with counting loss greater than 10% were not used. Frequent checks were made of the background (11 c/m in the photopeak), and of the counting efficiency, using a Na^{22} source. Typical initial count rates were 7,000 c/m for Cu^{63} and 180 c/m for Cu^{65} (the lowest yield). Counting was continued for two half-lives, with two separate counts for Pr and three for the other elements.

3. Analysis and Results

As 0.51 MeV γ-rays were detected in each case the crystal efficiency was constant. However, the calculation of self-

Figure 14

Calculation of Self-absorption

The geometry used and some calculated curves are shown. The construction of these curves is described on P. 61.

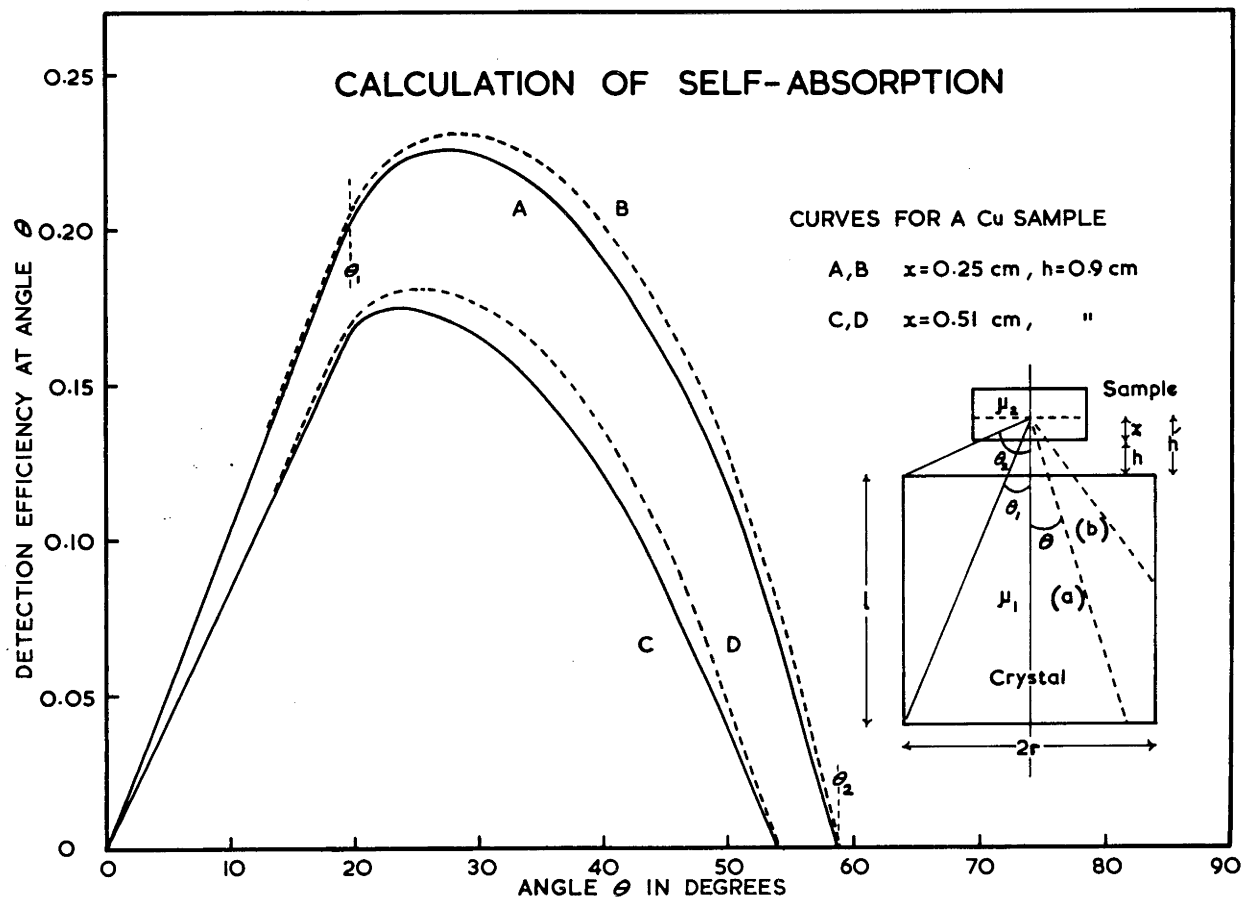
CALCULATION OF SELF-ABSORPTION
DETECTION EFFICIENCY AT ANGLE θ
ANGLE θ IN DEGREES
0.25
0.20
0.15
0.10
0.05
0
0
10
20
30
40
50
60
70
80
90
A
B
C
D
θ1
θ2
CURVES FOR A Cu SAMPLE
A,B x=0.25 cm , h=0.9 cm
C,D x=0.51 cm , "
Sample
μ2
x
h
t
θ2
θ1
θ
(b)
μ1
(a)
Crystal
2r

absorption corrections needed care as the activity was not uniformly distributed in the disks and they were counted close to the crystal.

The relevant dimensions and some results appear in figure 14. A first approximation assumes that the photons leaving a thin slice at x are all emitted parallel to the crystal axis; the intensity leaving the front face is then $I_o(x)e^{-\mu_2 x}$, and the intensity from the disk is given by an integration over x. An improvement is made by including the effect of the variation of self-absorption and crystal efficiency with the angle θ. Activity in the slice at x is assumed to be concentrated on the axis. The number of quanta emitted at the angle θ which are detected in the crystal is proportional to

$$k_1(\theta) = \sin\theta \cdot e^{-\mu_2 x/\cos\theta} \cdot (1 - e^{-\mu_1 p(\theta)}),$$

where the first term refers to solid angle, the second to self-absorption, and the third to interaction in the crystal; $p(\theta)$, the path-length in the crystal, is $L/\cos\theta$ for paths like (a) and $(r \operatorname{cosec}\theta - h \sec\theta)$ for paths like (b). The quantity

$$k_2(\theta) = \sin\theta \cdot (1 - e^{-\mu_1 p(\theta)})$$

is also calculated - here the self-absorption has been omitted. For a copper sample the standard value of h and a typical value of x were chosen, and $k_1(\theta)$ and $k_2(\theta)$ integrated numerically from $\theta = 0$ to $\theta = \theta_2$. The area under $k_2(\theta)$ was normalized to that under $k_1(\theta)$, using the previous correction factor multiplied by a "mean angle" term, thus:

$$\int_o^{\theta_2} k_1(\theta)\, d\theta = \int_o^{\theta_2} k_2(\theta) \cdot \exp\left[-\mu_2 x \overline{(1/\cos\theta)}\right] \cdot d\theta.$$

The term $\overline{(1/\cos\theta)}$, found in this manner, represents in an approximate way the effect of self-absorption. Its value was about 1.22 and did not change by more than 5% for a change of 0.1 in. in x and 25% changes in μ_2. It corresponds to a mean angle of about 35^o. In figure 14 the full curves show $k_1(\theta)$, while those dotted show $k_2(\theta)$, normalized with the ordinary correction factor $\exp\left[-\mu_2 x\right]$ only. The effect of self-absorption is clearly shown.

The activity $I_o(x)dx$ in a thin slice at x is calculated in Appendix A (the variable x used there must be replaced by (d + x) when x has its present meaning). The self-absorption correction term is now the ratio

$$\frac{\int_o^b I_o(x) \exp\left[-1.22\,\mu_2 x\right] dx}{\int_o^b I_o(x)\, dx} .$$

Numerical integration for each sample gave the correction factors in table 1. The absorption coefficients were taken from Grodstein's tables (Gr 57), with interpolation to the required Z when necessary.

If N_o^1 is the number of radioactive atoms of decay constant λ left at the end of an irradiation of length t_i, then

$$N_o^1 = k\, I\, \frac{\sigma N_t (1 - e^{-\lambda t_i})}{\lambda} ,$$

where σ is the cross section, k the geometric factor and I the radiation intensity, and N_t the density of target atoms in the

sample. The exponential term corrects for decay during the irradiation. If N_o is the initial population as derived from counts in the crystal, then

$$N_o^1 = \frac{N_o}{2\epsilon b} \quad ;$$

ϵ is the detection efficiency and b the fraction of positrons emitted per decay. The γ-ray intensity I is proportional to the monitor counting-rate γ, hence to compare cross sections for different isotopes we compute the quantity

$$J = \frac{N_o \lambda}{N_t \quad b \gamma (1 - e^{-\lambda t_i})} \quad .$$

The efficiency ϵ need only include the self-absorption term, and γ must be corrected for absorption of lithium γ-rays in the sample. The largest correction was 11% for copper.

Corrections for absorption do not enter into the comparison of Cu^{63} and Cu^{65} as the same disks were used for each measurement. The mass of PrF_3 was corrected for the presence of 2% of water; this was determined from the loss of weight on conversion to the oxide, after heating at 800°C for 14 hrs.*

In the estimate of experimental accuracy an allowance of 2% was made for variations in irradiation and counting geometry from one sample to another and of 1% for errors in monitor bias setting and variations in irradiation flux. Absorption corrections were assumed to have 10% accuracy. Statistical errors derived from

---

* This was done by Mr. M. J. Vernon.

deviations between runs were: Cu^{63}, 0.5% (7 measurements); Cu^{65}, 1.4% (2); Zn^{64}, 1.4% (3); Sb^{121}, 1.1%, (3); Pr^{141}, 1% (4).

The data for half-lives and fraction of positron decay were taken from Strominger et al. (SHS 58) or the Nuclear Data Sheets (NDS 59). Values adopted and the resulting cross sections are given in Table 1.

Table 1

Cross Section Measurements with the Lithium Resonance Radiation

Isotope	Half-life	Fraction of β^+ in total decay	Correction for self-absorption (%)	Total Cross Section relative to Cu^{63}	Total Cross Section (mb)
Cu^{63}	9.9 m	0.981	25	1	59 ± 6
Cu^{65}	12.8 h	0.19	25	1.19 ± 0.03	70 ± 7
Zn^{64}	38.3 m	0.904	10	0.68 ± 0.03	40 ± 4
Sb^{121}	16.4 m	0.438	11	2.07 ± 0.09	122 ± 13
Pr^{141}	3.4 m	0.54	4	3.07 ± 0.14	181 ± 20

4. Discussion

The cross sections in Table 2 are all for the lithium radiation and are computed as in Chapter 2. The quantities σ_{β^+} and $\sigma_{\beta^+}/\sigma_{Cu^{63}}$ are obtained using the decay scheme and Cu^{63} cross section adopted by each author. By this means the problem of absolute normalization is avoided.

Table 2

Comparison of Relative Cross Sections for the Lithium Resonance Radiation

Isotope	Reference	σ_{total} (mb)	σ_{β^+} (mb)	$\frac{\sigma_{\beta^+}}{\sigma_{Cu^{63}(author)}}$	Activity Measured
Cu^{65}	Katz & Cameron (Ka 51)	127	22.6*	0.26	$(\beta^+ + \beta^-)$
	Present work	70	13.3	0.23	γ^+
Zn^{64}	Katz & Cameron (Ka 51)	108	101	1.15	β^+
	Roalsvig et al. (Ro 60)	44	41	0.52	β^+
	Present work	40	36	0.61	γ^+
Sb^{121}	Katz & Cameron (Ka 51)	320	140	1.6	β^+
	Present work	122	53	0.9	γ^+
Pr^{141}	Carver & Turchinetz (Ca 59)	223	130	1.6	K X-ray
	Ferrero et al. (Fe 59)	282	152	1.7	γ^+
	Present work	181	98	1.7	γ^+

* Calculated from authors' value of $\sigma (\beta^+ + \beta^-)$

Study of the normalized cross sections shows that the present results and those of Katz and Cameron agree well for Cu^{65}, but differ by nearly a factor of 2 for Zn^{64} and Sb^{121}. Roalsvig et al. paid special attention to absolute β-counting with a flow counter and their result for Zn^{64} agrees reasonably well with the present work. It seems from their note that the Zn^{64} cross section calculated using the Leiss-Penfold tables was stated relative to the Cu^{63} cross section obtained using the Katz-Cameron tables. As they obtain at present different results from the two methods this is not a consistent treatment. It therefore seems that the ratio should be increased to about 0.65, in even better agreement with the present result.

The three measurements for Pr^{141}, each using scintillation counting of the activity, show good agreement.

It is clear from these comparisons that the absolute β-counting methods employed in much of this work have not been very reliable. We might have expected a correlation between positron energy and degree of agreement, but this does not appear. We find: Cu^{62} 2.91 MeV; Cu^{64} β^+ 0.66, β^- 0.57, good agreement; Zn^{63} 2.36, Sb^{120} 1.70, both poor agreement. In their review of their methods Baker and Katz (Ba 53) believed them to be accurate to 20%, which they considered good when compared with discrepancies in measurements by different radioactivity-standardizing laboratories at that time.

However, considerable improvements in standardizing techniques have taken place since then (Ma 54), and it should be practicable now to re-evaluate much of the older work using the latest methods, such as 4π β-counting, scintillation counting or coincidence work. Work along these lines has been done by Roalsvig, using a 4π flow-counter to study Cu^{63}, Zn^{64} and Ni^{58}. Previously determined yield curves should be quite satisfactory except for their normalization, so that measurements at one energy should be sufficient to greatly improve their usefulness.

In cases where scintillation studies are not possible 4π β-counting of thin samples should be the standard method.

CHAPTER 4

THE (γ,n) AND $(\gamma,2n)$ REACTIONS IN Ga^{69}

1. Introduction

One method for investigation of the relative importance of compound nucleus formation and direct interaction in photonuclear reactions is to compare the (γ,n) and $(\gamma,2n)$ excitation functions of a given nucleus. Above the $(\gamma,2n)$ threshold the two modes of de-excitation are in competition. If the first neutrons are evaporated from the excited nuclei their average energy will be small; there will usually be sufficient energy left for a second neutron to be evaporated, and the $(\gamma,2n)$ reaction will soon predominate over the (γ,n) as the gamma ray energy is increased above the threshold. On the other hand, if many of the first neutrons are ejected with high energies the (γ,n) cross section σ_1 will have a long tail and the $(\gamma,2n)$ cross section σ_2 will be correspondingly smaller. Measurement of σ_1 and σ_2 as a function of photon energy can therefore supply information on the energy spectrum of the first emitted neutrons.

Further information on the systematics of $(\gamma,2n)$ reactions should be helpful in the many studies made by total neutron detection. In these it is usually necessary to know σ_2 to investigate the splitting of the giant resonance or to measure

its width.

Previous measurements of σ_1 and σ_2 have been mainly in the heavy elements such as Ta^{181} (Ca 58), Au^{197} (Na 61) and Pr^{141} (Ca 59), and include only three medium-weight nuclei, Ni^{58} (Ca 59a), Cu^{63} (Be 54) and Nb^{93} (Si 58). The usual method has been to subtract from a total neutron yield curve a yield curve for σ_1 measured by residual activation, with the two curves normalized below the $(\gamma,2n)$ threshold. For many nuclei this is the only possible method, though in some cases both σ_1 and σ_2 have been measured by the activation technique. This method should be capable of greater accuracy as it does not entail taking the difference between two yield curves.

In the present experiment, the excitation functions σ_1 and σ_2 for Ga^{69} were measured by the activation method from the thresholds to 32 MeV at 1 MeV intervals. There are no previous measurements on Ga in this energy range. It is an interesting element for photoneutron studies, as the heavier isotope Ga^{71} has a closed shell of 40 neutrons. It would therefore be possible to study the change in Γ as the closed shell is approached. Unfortunately, there was not enough time for measurements on Ga^{71}, but it seems a worthwhile nucleus for study.

Figure 15

Nuclides near Gallium

The full lines show photonuclear reactions which can easily be studied by activation methods, and the dotted lines other possibilities.

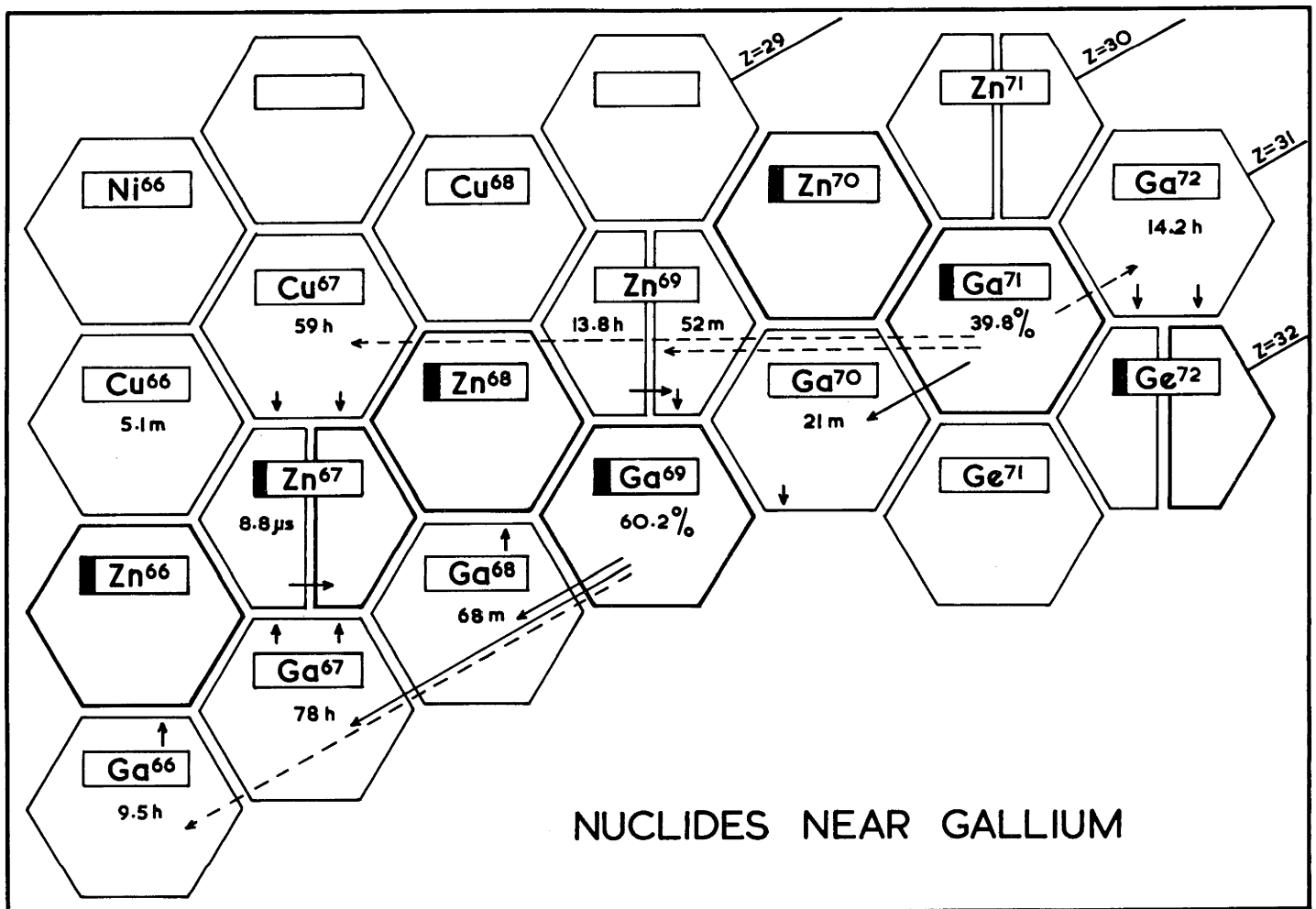
Z=29
Z=30
Z=31
Z=32
Ni66
Cu68
Zn71
Zn70
Ga72
14.2 h
Cu67
59 h
Zn69
13.8 h
52 m
Ga71
39.8%
Cu66
5.1 m
Zn68
Ga70
21 m
Ge72
Zn67
8.8 μs
Ga69
60.2%
Ge71
Zn66
Ga68
68 m
Ga67
78 h
Ga66
9.5 h
NUCLIDES NEAR GALLIUM

2. Experimental Work

Figure 15 shows the two gallium isotopes and the other nuclides near them. Some details of the photonuclear reactions in gallium which could be studied by the activation method are given in Table 1. The thresholds were obtained from the mass tables of Wapstra (Wa 58). T is the half-life of the residual nucleus, and the gamma-ray energies are in MeV.

Table 1

Photonuclear Reactions in Gallium

	Reaction	Threshold (MeV)	T	Activity
1.	$Ga^{71}(\gamma,n)Ga^{70}$	9.08	21 m.	β^-
2.	$Ga^{71}(\gamma,np)Zn^{69}$	17.03	52 m.	β^-; γ, 0.438
3.	$Ga^{71}(\gamma,\alpha)Cu^{67}$	5.23	59 h.	γ, 0.092, 0.182
4.	$Ga^{69}(\gamma,n)Ga^{68}$	10.30	68 m.	β^+
5.	$Ga^{69}(\gamma,2n)Ga^{67}$	18.60	78 h.	γ, 0.092, 0.182
6.	$Ga^{69}(\gamma,3n)Ga^{66}$	29.68	9.5 h.	β^+

Reactions 4 and 5 were those studied here, and reaction 1 could be investigated easily using β-counting. The other reactions were not observed.

The decay schemes of Ga^{67}, Ga^{68} and Ga^{70}, taken from the Nuclear Data Sheets (NDS 60), are shown in figure 16. They appear to be quite well established, except that the conversion coefficient of the 0.092 MeV gamma-ray from Ga^{67} is not known accurately; this point is discussed in section 3. The

Figure 16

Decay Schemes of Ga^{67}, Ga^{68} and Ga^{70}

These were taken from the Nuclear Data Sheets, 1960.

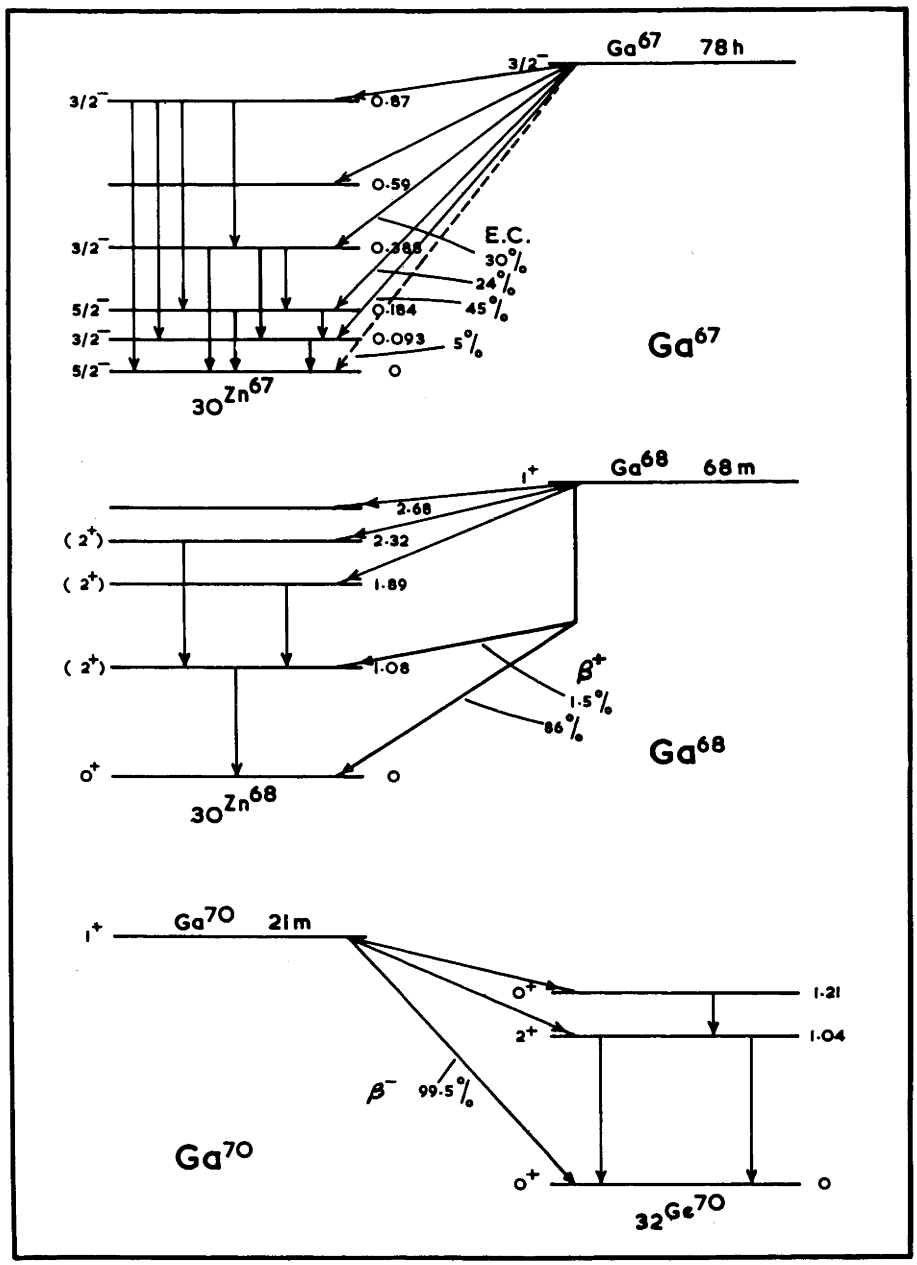
Ga67 78 h
3/2−
3/2−
0·87
0·59
3/2−
0·388
5/2−
0·184
3/2−
0·093
5/2−
0
E.C.
30%
24%
45%
5%
Ga67
30Zn67
1+
Ga68 68 m
2·68
(2+)
2·32
(2+)
1·89
(2+)
1·08
0+
0
β+
1·5%
86%
Ga68
30Zn68
1+
Ga70 21m
0+
1·21
2+
1·04
β−
99·5%
Ga70
0+
0
32Ge70

experimental results were consistent with half-lives of 68 m. for Ga^{68} and 78 h. for Ga^{67}.

2.1 Relative Yield Curves

The gallium was in the form of the oxide, Ga_2O_3, of purity about 99.99%. Each sample contained 1.3 gm. of this material in a thinwalled aluminium can with diameter $\frac{3}{4}$ in. and height 0.20 in. For an irradiation a tantalum monitor disk of the same diameter with thickness 0.010 in. was placed against each face; the whole was wrapped in cadmium foil to reduce slow-neutron capture and placed in a plastic holder about 2 in. from the donut of the 33 MeV electron-synchrotron.

Irradiations were usually for two hours above the $(\gamma,2n)$ threshold and for one hour below it, though these times were increased near the thresholds. An ionization chamber was used to check the constancy of the beam with time. The yield at each point was found relative to the average activity of the two tantalum disks, then converted to a relative yield per electron with the use of a standard yield curve for $Ta^{181}(\gamma,n)Ta^{180m}$ (Ca 58a). This had in turn been obtained, via experimental comparison of the $Ta^{181}(\gamma,n)$ and $Cu^{63}(\gamma,n)$ yield curves, from the $Cu^{63}(\gamma,n)$ excitation function of Berman and Brown (Be 54), which is taken as standard in this laboratory. (The results

of chapter 2 suggest that their measured cross section is about 30% too high, but as long as only renormalization is required it can be left as a final correction.)

The absolute scale of the yield curves was obtained by a direct comparison with Cu^{63}, as described in section 2.3.

2.2 Measurement of Residual Activity

The gamma-rays from the gallium samples and the 57 keV X-rays from Ta^{180} were detected with a scintillation spectrometer. This consisted of a $1\frac{3}{4}$ in. diameter by 2 in. Harshaw NaI(Tl) crystal mounted on a Dumont 6292 phototube, enclosed in a castle giving shielding of 1 in. of steel, 1 in. of mercury and 3 in. of lead.

The pulses were fed by a cathode-follower through a Higinbotham non-overload amplifier to a 100-channel Hutchinson-Scarrott kicksorter. The spectrometer energy calibration was checked frequently with the following sources (the gamma-ray energies are in MeV): Ce^{139}, 0.166; Na^{22}, 0.511, 1.28; Cs^{137}, 0.662; Zn^{65}, 1.12. The calibration was linear over this range and the energy resolution was 9% for the Cs^{137} 0.662 MeV line.

Owing to its large average dead-time (0.885 ms), the kicksorter could not be used for measuring the high initial counting rates from Ga^{68}. A single-channel analyzer with the window set over the 0.51 MeV photopeak was therefore placed in parallel with it. The window was set accurately by using the

Figure 17

Spectrum of Ga^{67} Radiation

The gamma ray spectrum from 78 h Ga^{67}, as measured in the 2 in. NaI crystal, is shown. The counting period was 2 hours.

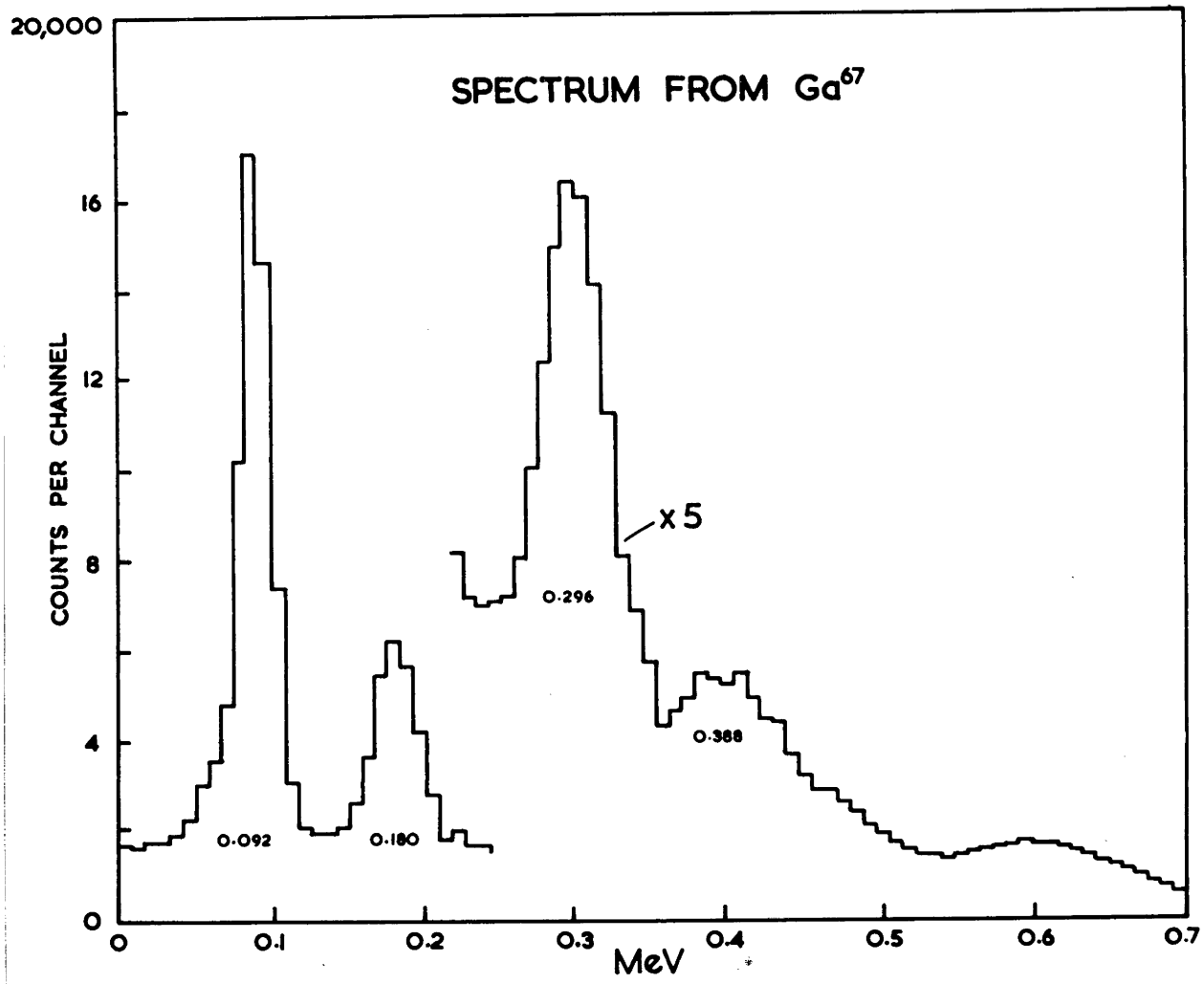
SPECTRUM FROM Ga67
20,000
16
12
8
4
0
COUNTS PER CHANNEL
x 5
0.092
0.180
0.296
0.388
0
0.1
0.2
0.3
0.4
0.5
0.6
0.7
MeV

output pulse of the analyzer to gate the kicksorter. A Na^{22} source was used to check the setting and counting rate before and after each run. The analyzer was also used with the monitor foils, for which the counting rates were often quite high, and provided a check on the kicksorter in the measurement of the Ga^{67} activity.

A spectrum of the radiation from Ga^{67} is shown in figure 17, and some typical decay curves for Ga^{68} and Ga^{67} are drawn in figure 18. In neither case was there any other significant activity present. The backgrounds were about 20 c/m for the 0.092 MeV peak and 10 c/m for the 0.51 MeV peak.

2.3 Normalization of Yield Curves

Normalization was carried out in two steps: first the comparison of Ga^{68} with the adopted standard Cu^{63}, then comparison of Ga^{68} with Ga^{67}. The method was to determine the relative yields per atom for irradiation with 30 MeV bremsstrahlung, then deduce the ratio of the integrated cross sections up to this energy.

A sample was made up of a mixture of Ga_2O_3 and Cu powder in accurately known proportions. This was irradiated at 30 MeV and the decay curve of the annihilation radiation analyzed for the 9.73 m and 68 m components. The X-ray intensity,

Figure 18

Decay Curves and Yield Curves for Ga^{67} and Ga^{68}

Some decay curves for 68 m Ga^{68} and 78 h Ga^{67} are plotted; $T_{\frac{1}{2}}$ is the appropriate half-life and T' the interval between the end of the irradiation and the middle of the counting period. The yield curves per electron, normalized to the value 100 at 30 MeV, are also drawn.

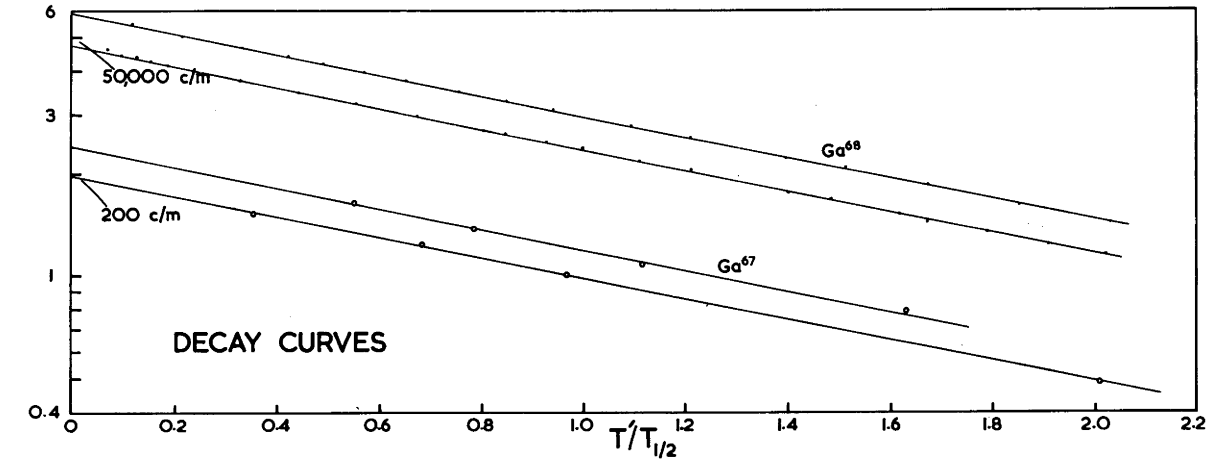
6
3
1
0.4
50,000 c/m
200 c/m
Ga68
Ga67
DECAY CURVES
0
0.2
0.4
0.6
0.8
1.0
1.2
1.4
1.6
1.8
2.0
2.2
T/T1/2

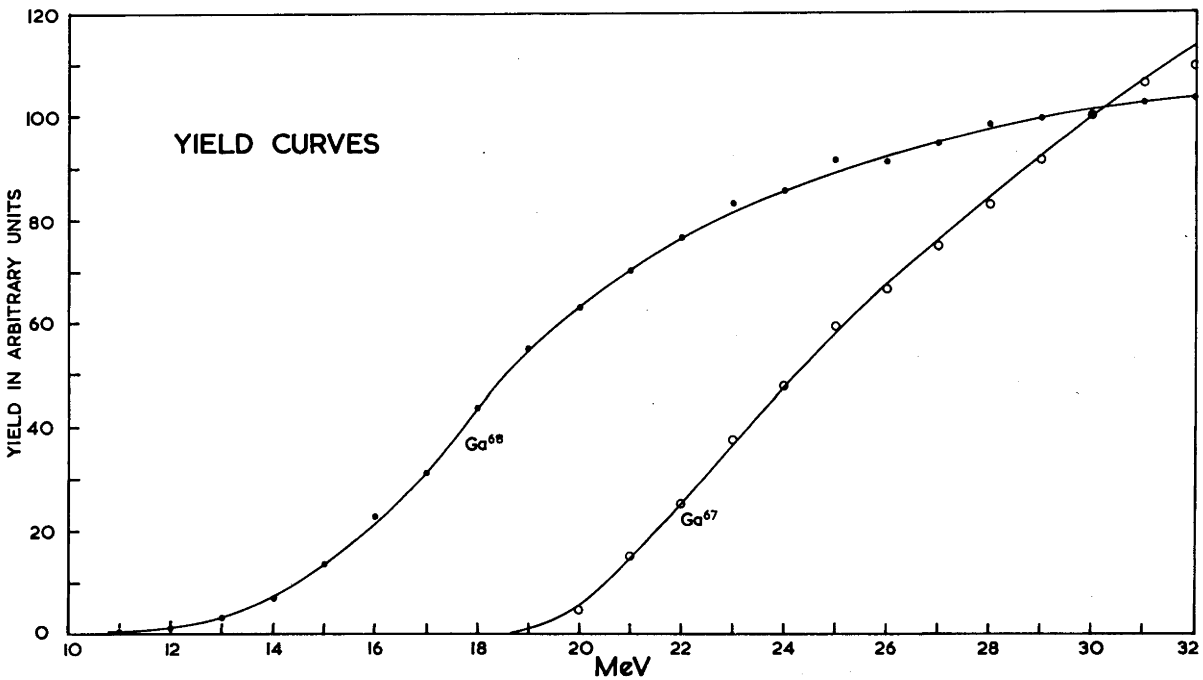
120
100
80
60
40
20
0
YIELD CURVES
YIELD IN ARBITRARY UNITS
Ga68
Ga67
10
12
14
16
18
20
22
24
26
28
30
32
MeV

photopeak detection efficiency and self-absorption were the same for each element and were not needed in the comparison, though it was necessary to keep the flux constant during the irradiation. The results from two irradiations lasting respectively 10 and 20 minutes agreed within 5%.

The comparison of Ga^{68} with Ga^{67} was more involved, as the gamma-rays did not have the same energy and the Ga^{67} photopeaks had to be separated from the rest of the spectrum. Independent calculations were made using the 0.092 and 0.182 MeV photopeaks. Corrections for self-absorption, making use of the absorption coefficients of Storm et al. (St 58), were: 0.092, 18%; 0.182, 9%; 0.511, 2%. The relative crystal efficiencies and photofractions were taken from the graphs of Vegors et al. (Ve 58).

The yield curves obtained, normalized to the value 100 at 30 MeV, are shown in figure 18. They were smoothed by means of first and second differences, then unfolded to obtain the excitation functions by the method described in Appendix D.

3. Results

The ratio of the (γ,n) yields per atom of Ga^{69} and Cu^{63} for 30 MeV bremsstrahlung was

$$\left[\text{Yield } Ga^{69}(\gamma,n) \Big/ \text{Yield } Cu^{63}(\gamma,n)\right]_{30\ \text{MeV}} = 1.73 \pm 0.06 .$$

From this figure and analysis of the yield curve the ratio of the cross sections integrated to this energy is

$$\left[\sigma_{int}\ Ga^{69}(\gamma,n) \Big/ \sigma_{int}\ Cu^{63}(\gamma,n)\right]_{30} = 1.7 \pm 0.1 .$$

The probable error quoted includes an estimated uncertainty of 5% in the ratio arising from inaccuracies of the original yield curve.

A difficulty which arose in the comparison of the (γ,n) and $(\gamma,2n)$ yields was due to conflicting results for the conversion coefficient of the 0.092 gamma-ray from Ga^{67}. Calculations using each of the three published values gave for the ratio $\left[\text{Yield}(\gamma,n) \Big/ \text{Yield}(\gamma,2n)\right]$ the figures 6.05, 7.10 and 7.52. Use of the 0.182 MeV line gave the ratio as 6.10; this line is only slightly converted and measurements on it agree well. As the measurement giving the ratio as 6.05 seems to be the most careful of the three, the adopted ratio was:

$$\left[\text{Yield } Ga^{69}(\gamma,n) \Big/ \text{Yield } Ga^{69}(\gamma,2n)\right]_{30\ MeV} = 6.1 \pm 0.7 .$$

The uncertainty quoted arises from the following estimated contributions: separation of photopeaks from background 5%, self-absorption corrections 2%, ratio of photopeak detection efficiencies 5%, yield ratio measurement 5% and uncertainty in decay scheme 10%. Adoption of a higher value of the ratio would favour the direct interaction interpretation. The corresponding ratio of integrated cross sections is

$$\left[\sigma_{int}\ Ga^{69}(\gamma,n) \Big/ \sigma_{int}\ Ga^{69}(\gamma,2n)\right]_{30} = 3.8 \pm 0.6 .$$

Figure 19

The (γ,n) and $(\gamma,2n)$ Excitation Functions for Ga^{69}

The excitation curves σ_1 and σ_2 are illustrated, along with $\sigma_1 + \sigma_2$ and $\sigma_1 + 2\sigma_2$. The cross section scale was derived from the Berman and Brown result for Cu^{63}, without renormalization. The cross-over point of σ_1 and σ_2 is shown to be at about 24.5 MeV.

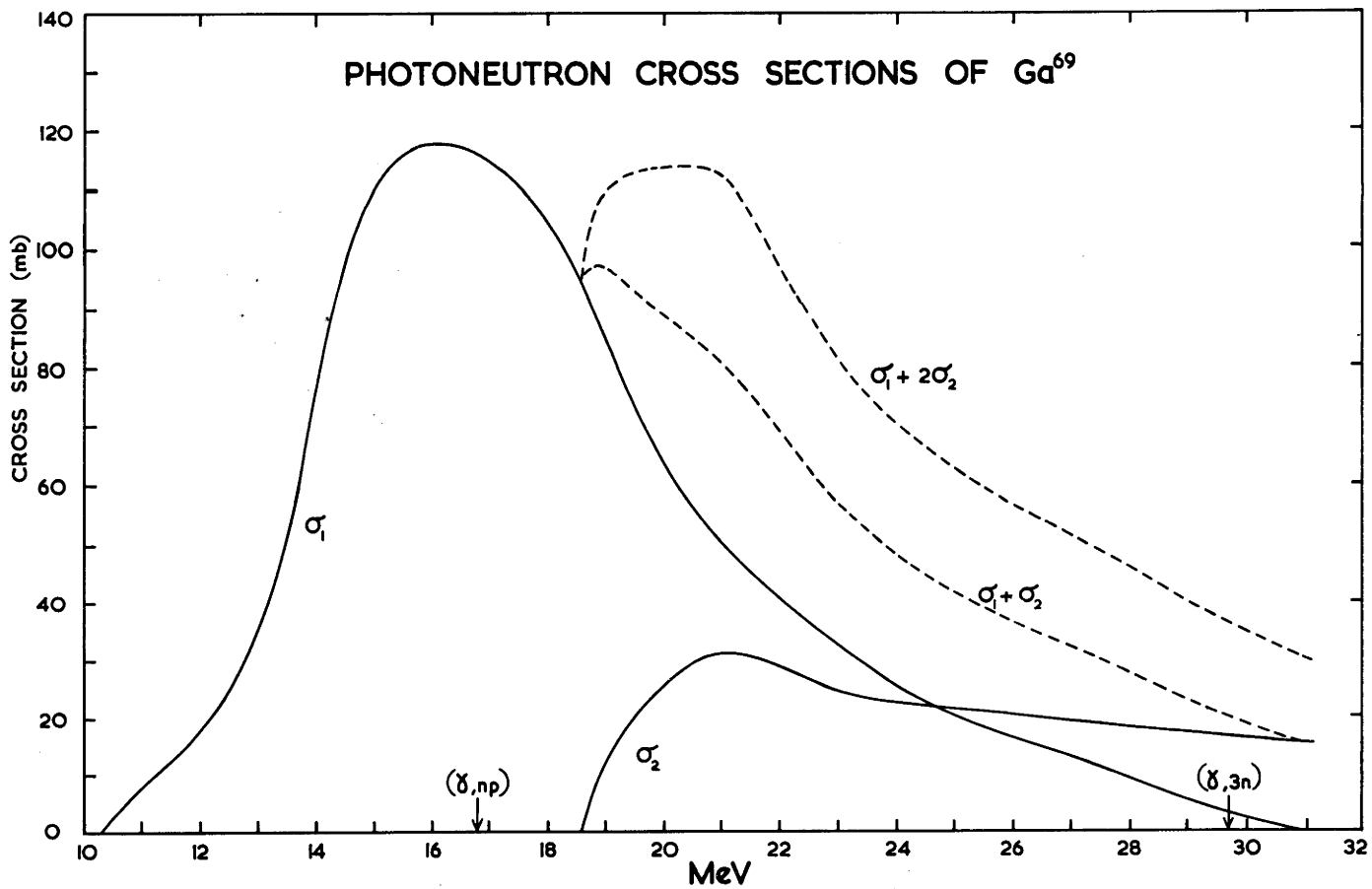
PHOTONEUTRON CROSS SECTIONS OF Ga69
CROSS SECTION (mb)
140
120
100
80
60
40
20
0
10
12
14
16
18
20
22
24
26
28
30
32
MeV
σ1
σ2
σ1 + σ2
σ1 + 2σ2
(γ,np)
(γ,3n)

The total integrated cross section to 30 MeV for the two reactions is therefore 2.2 $\pm$ 0.4 times that of $Cu^{63}(\gamma,n)$, or 1.20 $\pm$ 0.2 MeV-bn if the result of Berman and Brown (σ_{int} = 0.55 $\pm$ 0.03 MeV-bn) is accepted. The formula of Carver and Peaslee (P. 23) gives σ_{int} = 1.56 MeV-bn for integration over all energies.

We can estimate the relative importance of other possible reactions in Ga^{69}. The (γ,p) cross section is expected to be small, for two reasons. Although the true threshold is only 6.6 MeV the effective threshold would be about 10 MeV, close to that of the (γ,n) reaction. In addition the (γ,p) and (γ,n) reactions lead respectively to an even and an odd nucleus, hence the odd-even effect in energy level densities (Er 60) favours the (γ,n) reaction by a factor ~ 5. It is shown in section 4.2 that the (γ,np) cross section is much smaller than that of $(\gamma,2n)$. We conclude that the sum of the (γ,n) and $(\gamma,2n)$ cross sections represents most of the absorption cross section.

The excitation functions σ_1 and σ_2 are drawn in figure 19. (The normalization has not been altered from that given by the Berman and Brown result.) Also shown are the total absorption cross section $\sigma_1 + \sigma_2$ and the excitation function $\sigma_1 + 2\sigma_2$ which would follow from a measurement of the total neutron yield.

4. Discussion

4.1 Position and Width of the Giant Resonance

The peak energy of about 16.2 MeV is just within the limits of the formula given by Carver and Peaslee (P. 22). As the position of this rather broad peak is not determined very accurately this is quite good agreement.

The width Γ of σ_1 is about 6.5 MeV, while that of $\sigma_1 + \sigma_2$ has the quite large value of 9 MeV. Comparison with a diagram given by Okamoto (Ok 58) shows that this could have been expected. He plots the eccentricity of the nucleus and measured values of Γ against neutron number N. Although there are few measurements in the region, Γ appears to increase rapidly from $\sim$6 MeV to $\sim$ 10 MeV between N = 35 and N = 45. The present result falls rather above his curve but more measurements are needed to establish the trend accurately. A number of nuclei have been studied near N = 50 (Ye 56), where both proton and neutron shells are closed, but few near N = 40, where only the neutron shell is completed.

4.2 Neutron Energy Spectrum

Before comparison of σ_1 and σ_2 it is necessary to obtain some idea of the importance of the (γ,np) reaction, i.e. the relative probabilities of proton and neutron evaporation from the intermediate nucleus Ga^{68}.

This problem was treated by Weigold and Glover (We 61), in a discussion of compound nuclei formed by neutron capture. They show from simple statistical theory that an approximation for the relative probability of proton and neutron evaporation from an excited nucleus is given by the following formula:

$$P(p)/P(n) \simeq \exp \frac{1}{\tau}\left(S_n - S_p + \delta_p - \delta_n - 0.6V\right). \qquad (1)$$

S_n and S_p are the separation energies for a neutron and a proton respectively from the compound nucleus, δ_p and δ_n are the pairing energies for the respective residual nuclei and τ the average of their temperatures, while the final term is an approximation for the effective barrier to protons in terms of the barrier height V.

In the calculation for Ga^{68} the pairing terms cancel as both residual nuclei have odd mass. The result, with τ taken as 0.5 MeV, was $P(p)/P(n) \simeq 0.04$. It appears therefore that the (γ,np) reaction can be neglected, especially as the $(\gamma,n)/(\gamma,2n)$ normalization is not known particularly well.

The most direct approach to the neutron energy spectrum is to use the energy E_c at which σ_1 and σ_2 are equal. For a gamma-ray of energy E_c, exactly half of the neutrons are emitted with enough energy to make impossible evaporation of a second neutron. The difference between E_c and the $(\gamma,2n)$ threshold S_{2n} is therefore the median energy of the first neutrons emitted. This argument is quite general and requires no assumption about

the shape of the spectrum. There is a small inherent uncertainty since for a few hundred keV above the $(\gamma,2n)$ threshold the nucleus may emit a gamma-ray rather than a second neutron.

From figure 19 we find $E_c - S_{2n} \simeq 5.9$ MeV, suggesting a median neutron energy of about 5.5 MeV. It can be shown (Le 58) that the median energy of an evaporation spectrum is 1.7τ. An estimate of τ for Ga^{68} (by the method described on P. 112), suggests $\tau \simeq 1.5$ MeV, corresponding to a median energy of 2.6 MeV. As the experimental median energy is twice this we have clear evidence that many of the neutrons are ejected with high energies rather than being evaporated.

We can obtain a minimum estimate of the fraction which are directly ejected by making the extreme assumption that they all receive energies greater than 5.5 MeV. For $\tau = 1.5$ MeV only 13% of the evaporated neutrons receive such energies. It follows from a simple calculation that for a gamma-ray energy of about 25 MeV at least 40% of the neutrons have been emitted in direct interactions.

The present results seem to have some application to the theory of Carver et al. (P. 22). They suggest that when a nucleon is directly emitted the exchange energy $\Delta \simeq 7.5$ MeV is left in the nucleus. For irradiation of Ga^{69} with 25 MeV gamma-rays the maximum energy of an emitted neutron would be

Figure 20

Comparison of Statistical Predictions with Experiment

The dashed curves are those calculated for the given temperatures τ, assuming the initial neutrons to have an evaporation spectrum. The experimental curves from the present work on Ga^{69} and from the work of Berman and Brown on Cu^{63} are shown.

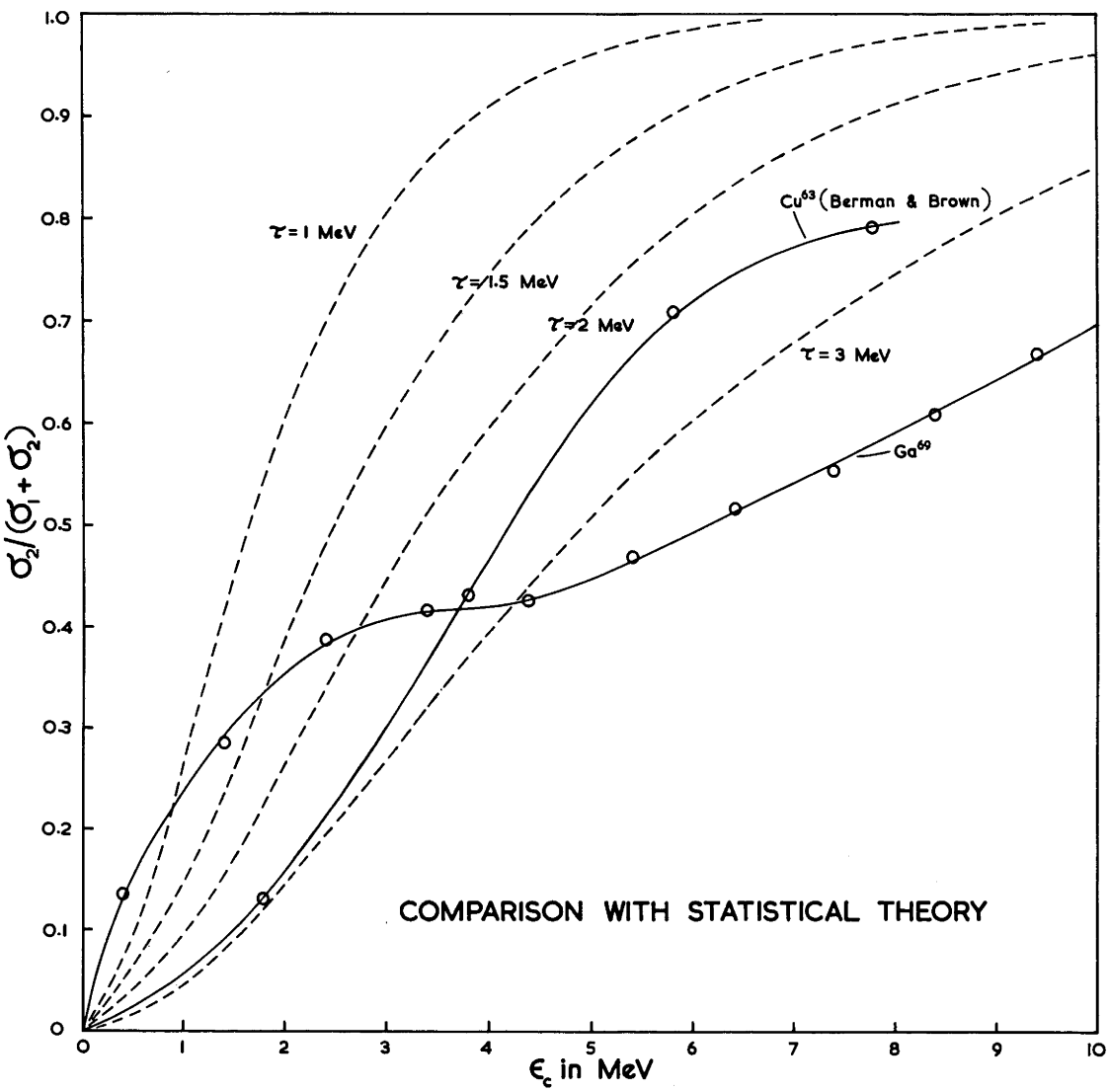
1.0
0.9
0.8
0.7
0.6
0.5
0.4
0.3
0.2
0.1
0
$\sigma_2/(\sigma_1+\sigma_2)$
0
1
2
3
4
5
6
7
8
9
10
ϵ_c in MeV
τ = 1 MeV
τ = 1.5 MeV
τ = 2 MeV
τ = 3 MeV
Cu^{63} (Berman & Brown)
Ga^{69}
COMPARISON WITH STATISTICAL THEORY

$25.0 - 10.3 - 7.5 \simeq 7$ MeV, whereas we have found the median energy to be ~ 5.5 MeV. This suggests that either the energy Δ is sometimes available for direct emission or that the neutron spectrum has a strong peak at ~ 6 MeV. (The three-quantum resonance peak (P. 24) would be at about 32 MeV and can be neglected.) It seems worthwhile, therefore, to see if the present experiment can give any further information on the neutron spectrum.

An approximate statistical model calculation of the competition between evaporation of one or of two neutrons presents the following result (Bl 52):

$$\sigma(a;\, n,n) = \sigma'(a,n)\left[1 - (1 + \epsilon_c/\tau)\exp(-\epsilon_c/\tau)\right], \qquad (2)$$

where a represents any incident particle, $\sigma'(a,n)$ is the sum of the cross sections for all reactions in which a neutron is emitted first, and ϵ_c is the excess excitation energy over the threshold for evaporation of the second neutron. For the present experiment, (2) may be restated as

$$\sigma_2/(\sigma_1 + \sigma_2) = 1 - (1 + \epsilon_c/\tau)\exp(-\epsilon_c/\tau), \qquad (3)$$

where $_c = h\nu - 18.60$ MeV.

Calculations of this function for a few values of τ are compared with the experimental ratio in figure 20. Although the experimental curve is not very reliable because σ_1 is not accurately known in this region, it certainly does not fit any statistical prediction. The curve rises quicker than those

calculated but falls below them at higher energies. This suggests that the neutron spectrum rises more steeply at low energies than a statistical spectrum and has a more pronounced high energy tail. The last is certainly what we expect but the first conclusion must be rather tentative.

There is no sign of an increase in slope for $\epsilon_c \sim 6$ MeV, which would occur if the spectrum had a strong peak there. However the measurements are probably not accurate enough to show this if it did occur, and it is likely that the neutron spectrum would change with excitation energy.

From figure 19 we see that σ_1 becomes negligible compared with σ_2 above about 30 MeV. This result must be viewed with suspicion as σ_1 is poorly known there, but if accepted leads to an estimate of the maximum energy E_{max} of the ejected neutrons. For a 30 MeV γ-ray, E_{max} would be $30 - 18.6 \simeq 11.5$ MeV or $11.5 - 7.5 \simeq 4$ MeV depending whether or not the exchange energy is available to a directly emitted particle. As the median energy will be greater than 5.5 MeV the second alternative does not seem very likely.

4.3 Some Comparisons with Other Work

An experiment similar to the present one has been carried out on Pr^{141} (Ca 59), with results which are rather different. This nucleus, with a closed shell of 82 neutrons, has a narrow

giant resonance ($\Gamma \simeq 4$ MeV), and a long tail on σ_1. The $(\gamma,2n)$ excitation function has a shape very similar to that from Ga^{69}, but although the threshold is at 18.3 MeV, σ_1 is still greater than σ_2 up to the maximum energy of 32 MeV. P(p)/P(n) for Pr^{140} is ~ 0.02, so that the (γ,np) reaction can be neglected. Hence this experiment suggests that the median neutron energy at $E_\gamma = 32$ MeV is greater than 14 MeV, whereas the maximum neutron energy would be ~ 14.5 MeV if the exchange energy is always left in the nucleus. Here again we have evidence that a nucleon may sometimes receive the full photon energy. This seems plausible if, as is likely, nucleons emitted directly are those near the surface.

A measurement of the $Ta^{181}(\gamma,n)$, $(\gamma,2n)$ excitation functions by a combination of neutron detection and activation methods (Ca 58), shows that for this nucleus σ_1 equals σ_2 about 2.3 MeV above the $(\gamma,2n)$ threshold. This requires an evaporation temperature at $E_\gamma = 16$ MeV of 1.35 MeV while a calculation suggests $T \simeq 0.6$ MeV. Again we have good evidence for direct interactions, which was expressed rather differently by the original authors as the ratio of the integrated cross sections over the high-energy region.

The measurements of Berman and Brown (Be 54) for Cu^{63} show $E_c \simeq 23.5$ MeV, implying a median neutron energy of ~ 4.5 MeV.

However $P(p)/P(n) \simeq 0.4$, so the (γ,np) reaction can certainly not be neglected. Although a plot of $\sigma_2/(\sigma_1 + \sigma_2)$ fits the statistical theory quite well (figure 20), further calculation with inclusion of the (γ,np) cross section would be needed to make the position quite clear.

A further topic of interest is the sum $\sigma_1 + \sigma_2$, which should be close to the absorption cross section and should therefore be a smooth function. Figure 19 shows that this is fairly true for Ga^{69}, but for Pr^{141} (Ca 59) there is a pronounced bump at the $(\gamma,2n)$ threshold. This could be due to the fact that a dip in σ_1 has not been resolved, or that a competing reaction such as the (γ,p) fills in the gap. For both Ga^{69} and Pr^{141}, $\sigma_1 + 2\sigma_2$ has a double peak, underlining the importance of careful separation of the $(\gamma,2n)$ contribution in neutron detection studies of peak splitting.

4.4 Conclusions

The present measurements show that the giant resonance of Ga^{69} has an integrated cross section to 30 MeV which is 2.2 ± 0.4 times that of the $Cu^{63}(\gamma,n)Cu^{62}$ reaction. The ratio of the integrated (γ,n) and $(\gamma,2n)$ cross sections to this energy is 3.8 ± 0.6. The peak position is about 16.2 MeV and the width about 9 MeV, both in reasonable agreement with the systematics of the photonuclear process.

It has been shown that the neutrons emitted from Ga^{69} after excitation at E_γ = 25 MeV have a median energy of $\sim$ 5.5 MeV, which is a factor of 2 too high to be due to evaporation. It follows that at this excitation energy at least 40% of the neutrons are emitted in direct interactions.

The neutron energy spectrum appears to have more low-energy particles than an evaporation spectrum, and has a longer high-energy tail.

Some evidence suggests that the full energy of a photon may sometimes be available for emission of a single nucleon.

Results from similar experiments by other workers lend support to the conclusions reached in this work.

CHAPTER 5

ISOMERIC RATIOS IN (γ,n) REACTIONS AND THE SPIN-DEPENDENCE OF LEVEL DENSITY

1. Introduction

There is at present little experimental evidence relating to the spin-dependence of nuclear level density. The variation in density of states with Z, N and the excitation energy is now understood in a general fashion, (Er 60) but the distribution over J-values is less well known. Such information would be very useful, as it is closely related to the problem of the moment of inertia of the nucleus, a topic of considerable interest and difficulty in nuclear structure theory. Nuclei have in their low-lying states moment of inertia $\mathcal{I}$ from 1/5 to 1/2 the rigid-body result $\mathcal{I}_o$. We wish to know if $\mathcal{I}$ approaches $\mathcal{I}_o$ at higher excitation energies, as this will show the destruction of the correlations among the nucleons.

The most direct method of approach is to establish the energies, spins and parities of a large number of levels of a given nucleus. Hibdon (Hi 59, Hi 61) used high resolution neutron spectroscopy to achieve this for 71 levels in Na^{24} and 66 for Al^{28}. With a less complete classification of the spins of individual levels, Ericson (Er 59) and Carver and Jones (Ca 60b) inferred spin distributions by comparing the total

level density (for all spin states), with the density of states of a particular spin.

A less direct method was applied by Douglas and McDonald (Do 59) and by Ericson and Scrutinski (Er 58). They examine the angular distribution of emitted particles from an evaporation process at high excitation energies, where many states are excited simultaneously. Measurement of the degree of anisotropy about 90^{o} can provide useful information.

A second type of indirect method was used in the present work. It consists in measuring the relative cross sections for formation of a residual nucleus in each of an isomeric pair of levels, following an evaporation process. Although many types of compound nucleus reaction are suitable, the (γ,n) reaction can be shown to have some advantages. Using activation methods a study of the relative populations of components of an isomeric pair following a (γ,n) reaction was made for 15 nuclei. Suitable target nuclides were selected over the range $A = 59$ to $A = 198$, in a search for systematic trends in the results.

A few similar studies have been made previously (Ka 52, Ka 53, Si 56), but no theory was available to relate the results to the statistical parameters of the nucleus. These experiments are discussed in section 5.

The isomer ratios were obtained by irradiation with 30 MeV bremsstrahlung. No attempt was made, in this survey experiment,

Figure 21

Spin Dependence of Energy Level Density

The function

$$\rho(J)/\rho(0) = (2J + 1) \exp\left[-J(J + 1)/2\sigma^2\right]$$

is plotted for the stated values of σ. Results from the present experiment usually lie between $\sigma = 2$ and $\sigma = 4$. The straight line for $\sigma = \infty$ corresponds to the common approximation

$$\rho(J)/\rho(0) = 2J + 1 \text{ .}$$

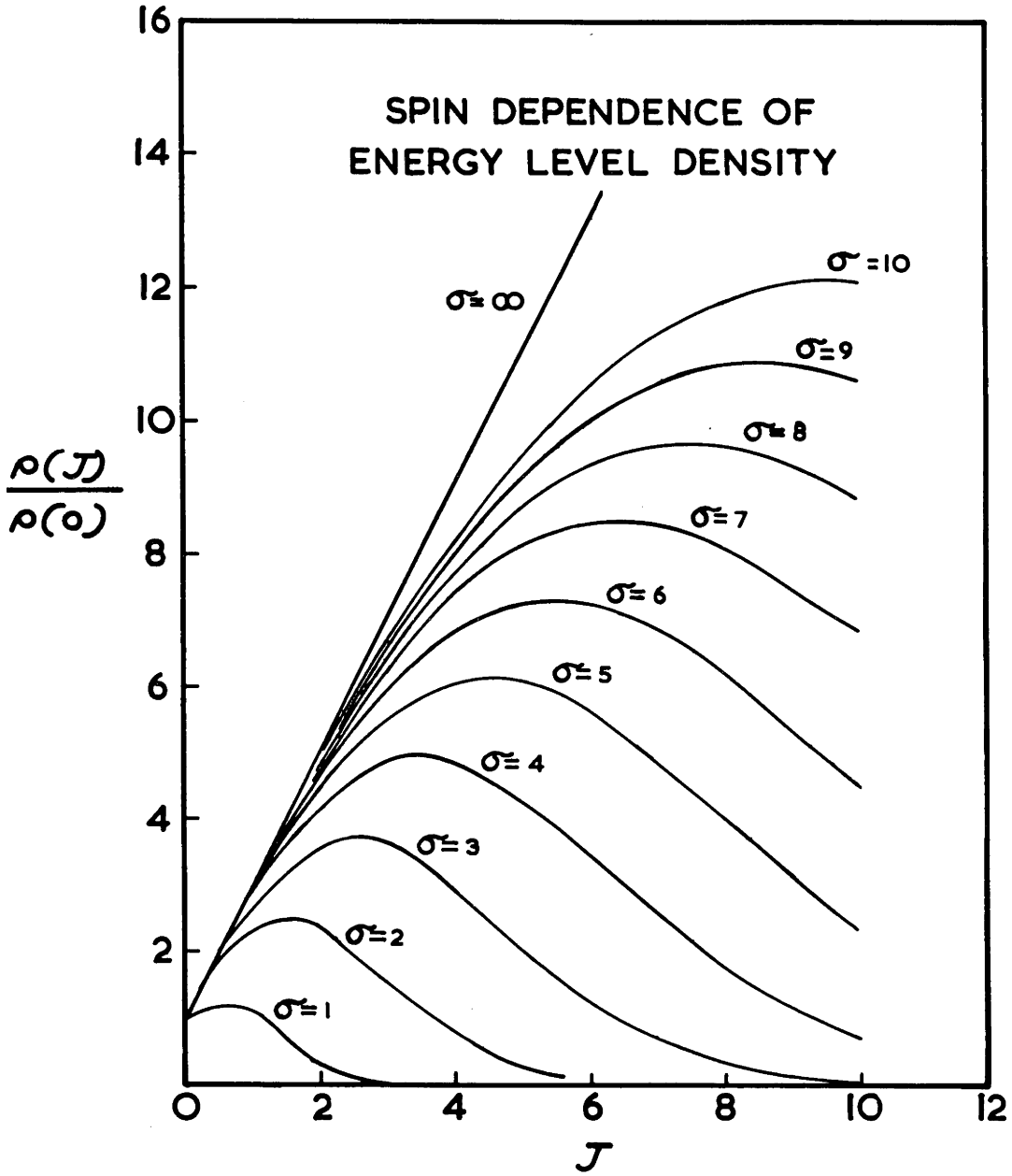
SPIN DEPENDENCE OF
ENERGY LEVEL DENSITY
ρ(J)/ρ(0)
J
σ=∞
σ=10
σ=9
σ=8
σ=7
σ=6
σ=5
σ=4
σ=3
σ=2
σ=1
0
2
4
6
8
10
12
14
16

to study the variation of each ratio with X-ray energy. This has been done previously, however, in the experiments just mentioned. The ratio is found to be fairly constant with energy, except near threshold. It therefore seems that no large errors should be introduced by the present technique.

1.1 Spin-Dependence of the Level Density and the Nuclear Moment of Inertia

The most commonly used approximation for the dependence of level density on J is

$$\rho_U (U, J) = (2J + 1)\, \rho (U,0) \qquad (1)$$

where $\rho(U,J)$ and $\rho(U,0)$ are the densities at excitation energy U for levels of spin J and spin 0 respectively. Equation (1) is of very limited validity and a more exact expression is (Er 60)

$$\rho (U,J) = (2J + 1)\, \exp\left[- J(J + 1)/2\sigma^2\right] \cdot \rho(U,o), \quad (2)$$

where all factors independent of J have been merged into $\rho(U,o)$. The exponential term is known as the "spin-cutoff factor"; its effect can be seen in figure 21, in which $\rho (U,J)/\rho (U,o)$ is plotted against J, for a range of values of σ. Equation (1) corresponds to $\sigma = \infty$. The exponential term reduces the probability of states of high spin.

The important dispersion parameter σ which characterizes the distribution (2) is related to the temperature t and to $\mathcal{I} = c\hbar^2$ the moment of inertia of the nucleus by (Er 60)

$$\sigma^2 = ct = \frac{\mathcal{J} t}{\hbar^2} \quad . \tag{3}$$

The "thermodynamic temperature" t is related to the "nuclear temperature" T by (La 54)

$$\frac{1}{T} = \frac{1}{t} - \frac{3}{4U} \quad . \tag{4}$$

It is convenient to relate $\mathcal{J}$ to the rigid-body value $\mathcal{J}_o$ given by

$$\mathcal{J}_o = c_o \hbar^2 = \frac{2}{5} M A R^2 \quad . \tag{5}$$

(M = nucleon mass, A = mass number, R = nuclear radius). This is also the result obtained by Bloch (Bl 54) for independent particles in a square well. For a nuclear radius parameter $r_o = 1.2 \times 10^{-13}$ cm, we have

$$c_o = \left[A^{5/3} / 75 \right] \text{ MeV}^{-1} . \tag{6}$$

It is not strictly correct to take σ as constant for a given energy. Equation (3) shows that even for a constant moment of inertia σ^2 will vary with t, or approximately as $U^{\frac{1}{2}}$. We also expect $\mathcal{J}$ and therefore c to increase with the energy of excitation. However, following Huizenga et al. (Hu 60), σ will in the present work be taken as constant over the energy region of interest. They produce some evidence that σ does not vary strongly with energy. Thus this simplifying assumption seems justified, though further refinements could no doubt be introduced in further work.

Figure 22

(γ,n) Reaction leading to an Isomeric Pair

The diagram illustrates the excitation by a photon of a nucleus with ground state spin J_o, and its subsequent decay to a nucleus having an isomeric pair of levels. The numbered steps in the process are discussed on P. 89. S_n is the separation energy of the last neutron from the target nucleus.

An inset shows the decay of the isomeric levels, as used in the calculations on P. 102; p_1 is the fraction of the isomer level decay which arrives at the ground state.

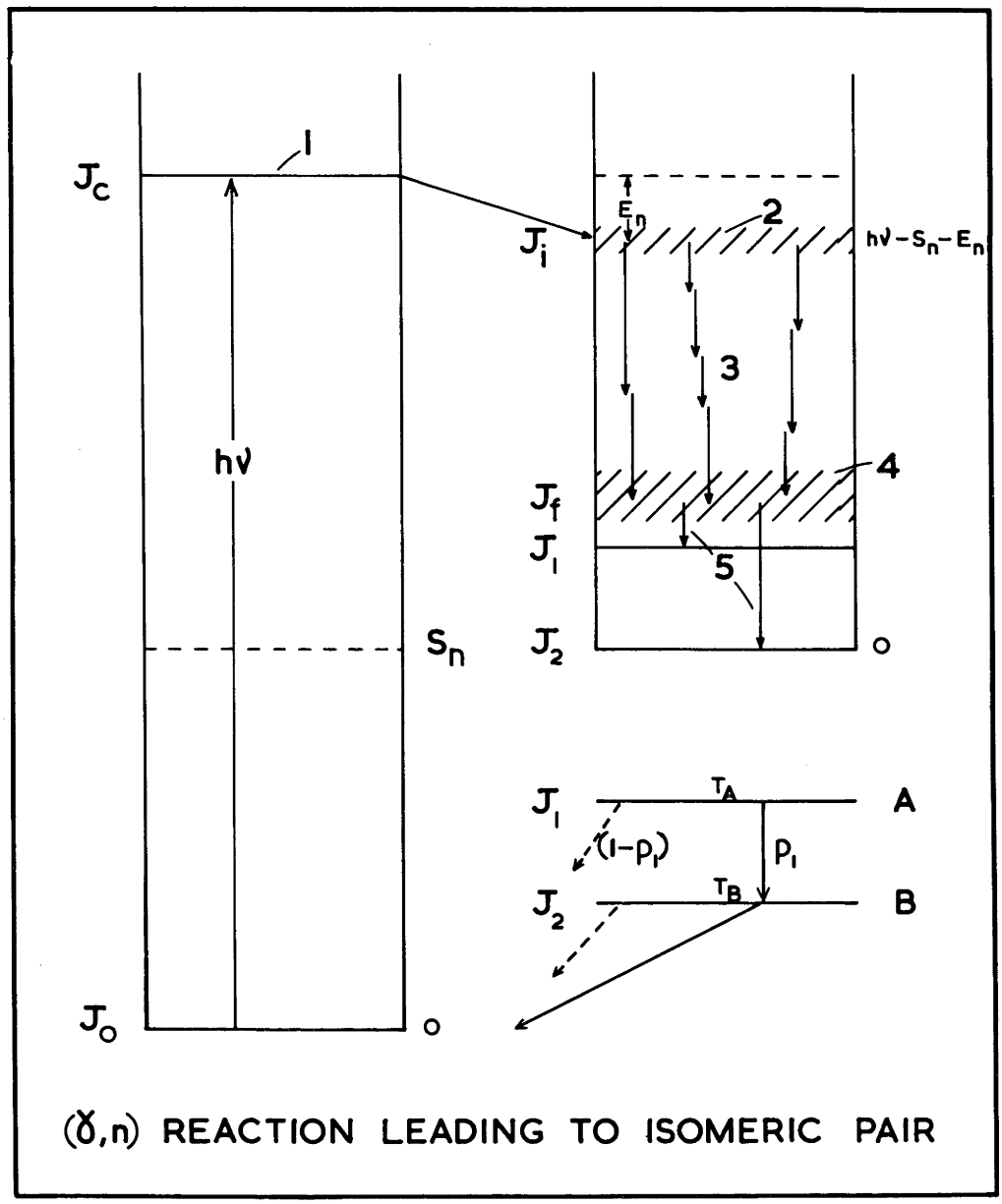

(γ,n) REACTION LEADING TO ISOMERIC PAIR

1.2 Outline of Statistical Treatment

The theory to be used was developed by Huizenga and Vandenbosch, (Hu 60) who applied it to their results for Hg^{197} (Va 60). It has since been applied with success to several reactions producing Co^{58} (We 61). An outline of the treatment is given here with further details of the assumptions and calculations reserved for section 2.

The application of their ideas to a (γ,n) reaction can be followed with reference to figure 22, which illustrates the five steps in the process. Of these, (2) and (4) are influenced by the value of σ. The target nucleus has $J = J_o$ in the ground state.

(1) A photon absorbed in the giant resonance raises the nucleus to a level of excitation energy $h\nu$ and spin J_c. (2) A neutron is emitted with energy E_n. The residual nucleus is formed in a level with spin J_i at an excitation energy $h\nu - S_n - E_n$, where S_n is the separation energy of a neutron from the target nucleus. The nucleus now emits gamma-rays, and cascades over many paths to within about 1 MeV of the ground state. Step (3) is the calculation of the distribution in the number of gamma-rays per cascade. (4) The spin distribution broadens with each emission, and near the ground state covers a range of spins J_f. (5) With emission of the final gamma-ray this distribution separates between the levels 1 and 2, with spins J_1 and J_2.

The relative probabilities of the possible spins must be calculated at each step, i.e. we must derive from statistical theory the distribution functions $P(J_c)$, $P(J_i)$, and $P(J_f)$, each of which depends on the one before it. It is assumed that at each stage sufficient levels are available to make statistical formulae applicable.

The complete calculation is carried through for a range of σ, so that comparison with the experimental result will give the best value for this parameter.

It is probable that, for some nuclei, the statistical assumptions may not always hold. For example, in some nuclei, such as lead, the de-excitation takes place via only a few gamma-rays of high energy. It is hoped that study of a number of nuclei will allow recognition of one behaving in a way such as this.

2. Theoretical Treatment

The calculations for the five steps described in section 1.2 are fairly simple but tedious; they are described in more detail below. Huizenga et al. (Hu 60) discuss in detail the assumptions made.

2.1 Compound State

It is assumed that the absorption takes place by an E1 transition in the giant resonance region. Hence a target with

$J_o = 0$ must arrive at a level with $J_c = 1$. The excited state of a nucleus with $J_o \neq 0$ is assumed to take up one of the values $J_c = J_o - 1, J_o, J_o + 1$, with respective probabilities proportional to $2J_c + 1$ (Bl 52). Huizenga gives the rather more complicated formula to be used for a particle-induced reaction. The simplicity and definiteness of this part of the calculation in the case of a photonuclear reaction is an advantage over other types of reaction which could be used.

This simple distribution over three or fewer spins is now modified by evaporation of the neutron, followed by emission of gamma-rays.

2.2 Evaporation of the Neutron

The relative probability for an excited state with spin J_c to emit a neutron with orbital angular momentum l leading to a state in the residual nucleus of spin J_i is given by

$$P(J_i) \propto \rho(J_i) \sum_{S=\left|J_i-\frac{1}{2}\right|}^{J_i+\frac{1}{2}} \sum_{l=J_c-s}^{J_c+s} T_l(E)$$

where $T_l(E)$ is the barrier transmission coefficient for a neutron with energy E. Values of $T_l(E)$ were taken from Feld et al. (Fe 51). The energy of the giant resonance was taken as 17 MeV for a medium-weight nucleus and 14 MeV for a heavy nucleus, with the nuclear temperature τ and neutron separation energy S_n equal to 1 MeV and 8 MeV respectively in each case.

T_L was taken as that for a neutron of the mean energy 2τ. By dividing the neutron energy spectrum into four sections and calculating each separately, Huizenga showed that this was a good approximation.

In table 1, we show $P(J_i)$ as a function of σ and J_i, for a medium and a heavy nucleus, for the case $J_c = 1$.

Table 1

Table of $P(J_i)$ as a function of σ, for $J_c = 1$

	Medium Nucleus					Heavy Nucleus				
$J_i \backslash \sigma$	2	3	4	5	∞	2	3	4	5	∞
1/2	0.31	0.25	0.21	0.20	0.18	0.24	0.18	0.15	0.13	0.11
3/2	0.49	0.44	0.44	0.43	0.41	0.46	0.37	0.35	0.34	0.30
5/2	0.18	0.25	0.26	0.27	0.29	0.23	0.29	0.29	0.29	0.29
7/2	0.02	0.05	0.08	0.08	0.10	0.06	0.12	0.15	0.16	0.19
9/2	0	0.01	0.01	0.02	0.02	0.01	0.03	0.05	0.06	0.08
11/2	0	0	0	0	0	0	0.01	0.01	0.02	0.03

2.3 Number of Cascade Gamma-Rays

It is possible to estimate from statistical theory the distribution in the number of gamma rays per cascade. The spectrum for dipole radiation is of the general form (Bl 52),

$$P(\epsilon) \propto \epsilon^3 \rho(U_c - \epsilon),$$

where $P(\epsilon)$ is the probability for emission of radiation of energy ϵ, from a level with excitation energy U_c. The level

density can be taken as $\rho\,(U_c - \epsilon) \simeq$ const. $\exp\left[\frac{U_c - \epsilon}{\tau}\right]$. 93

For the present purpose we may then take

$$P\,(\epsilon) \simeq \text{Const.}\,\epsilon^3\, e^{-\epsilon/\tau}.$$

The temperature τ was taken as 1 MeV. From the adopted E_m, S_n and t we find that the energy to be radiated is 7 MeV for a medium nucleus and 4 MeV for a heavy nucleus.

The spectrum was divided into strips 1 MeV wide. For the medium nucleus, the fraction of gamma-rays with energies between 6 and 7 MeV was regarded as reaching the region near the isomeric levels in one emission. The procedure for a two-step cascade was as follows: the fraction of the radiation with $\sim$ 1 MeV in the first step was multiplied by the fraction with $\sim$ 6 MeV in the second; similarly were formed all other products in which the energies totalled 7 MeV. The sum of these products was the fraction reaching the lower levels in two jumps. The method for a three-step cascade was similar, except that many triple products were required. The calculation for a heavy nucleus was similar, except that only 4 MeV was to be radiated.

The relative probability of 1, 2, 3 or 4 gamma-rays in the cascade is given in table 2. As the final results do not depend sensitively on these numbers the rather crude calculation seems adequate.

From these figures, $\overline{\nu}$, the average number of gamma-rays per cascade, is easily determined. (The extra photon added is

Table 2

Relative Probabilities of n Gamma-rays in Cascade

	Medium Nucleus	Heavy Nucleus
n	P (n)	P (n)
1	0.08	0.36
2	0.52	0.55
3	0.34	0.09
4	0.06	0
	$\overline{\nu}$ = 2.4+1 = 3.4	$\overline{\nu}$ = 1.7+1 = 2.7

that which makes the final transition to the isomeric levels.) For the medium nucleus, $\overline{\nu}$ is very similar to results from neutron capture studies (e.g. Mu 50). The situation for the heavy nucleus is not comparable, however, as there is only $\sim$4 rather than $\sim$8 MeV to be radiated. The calculated $\overline{\nu}$ for the heavy nucleus is therefore rather less than that obtained by Muelhause.

2.4 Broadening of Spin Distribution by Gamma-ray Cascade

The assumption here is that all transitions are dipole in character, i.e. for each jump $\Delta l = \pm 1$ or 0. (Levels of odd and even parity are believed to exist in roughly equal numbers, so the parity selection rule causes no difficulty.)

A level of spin J_i will decay to states with spins $J_i - 1$, J_i and $J_i + 1$, with relative probabilities proportional to the

level density term $(2J + 1)\left[\exp - J(J + 1))/2\sigma^2\right]$. Each of these levels can further cascade to three spin groups. The contributions to each new spin group are added and the process repeated for the third transition. In this way, for a given J_i and σ the distribution $P(J_f)$ can be calculated for each step in the cascade.

A set of such calculations for both integral and half-integral J_i has been prepared. As these tables are rather long they are presented in Appendix E.

2.5 Populating of the Isomeric Levels

The computations described in the previous four sections are now to be combined to give the relative probabilities for population of the two isomer levels. Following Huizenga and Vandenbosch, it is assumed that the last transition takes place which has the smaller spin change, i.e., the distribution $P(J_f)$ midway separates/between the spin values of the isomer levels. If a third state of intermediate spin lies between them it competes with the isomeric level. This happens, e.g., in Br^{80}, where a $J = 2$ state intervenes between the $J = 5$ metastable state and the $J = 1$ ground state.

From the tables in Appendix E was obtained, for each step in the cascade, the fraction of transitions from a given J_i which proceeded to the higher spin state of the isomeric pair.

Figure 23

Role of σ in de-excitation

The probability distributions of the spins J_i (at the beginning of the gamma ray cascade) and J_f (near the end of the cascade) are illustrated for $\sigma = 3$, 5 and ∞. These have been calculated for a target nucleus with $J_o = 0$. The small influence of σ on $P(J_i)$ and the quite large influence on $P(J_f)$ are easily seen. The distributions are naturally not continuous but the points are joined for clarity.

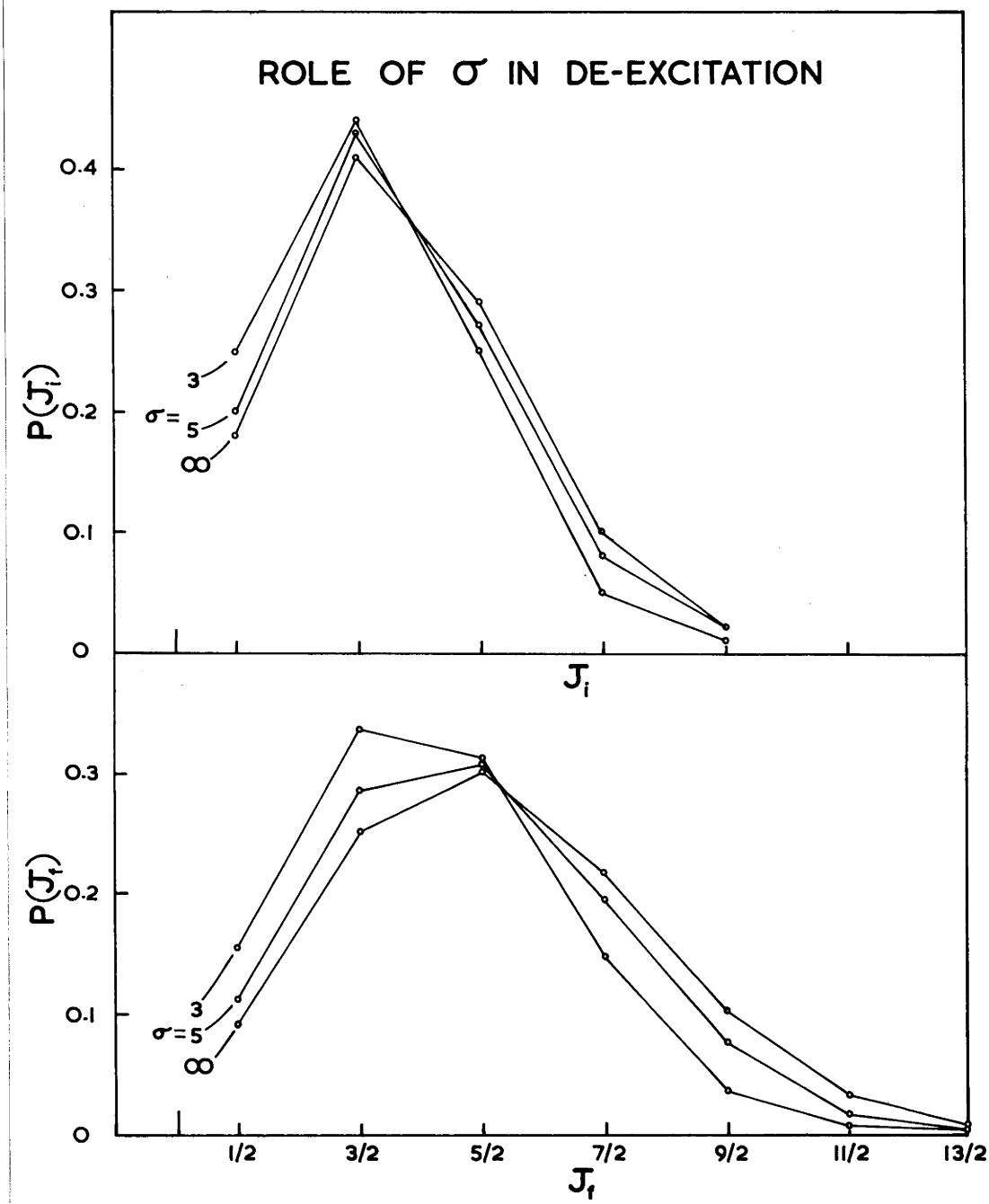
ROLE OF σ IN DE-EXCITATION
P(Jf)
0.4
0.3
0.2
0.1
0
σ=
3
5
∞
Ji
P(Jf)
0.3
0.2
0.1
0
σ=
3
5
∞
1/2
3/2
5/2
7/2
9/2
11/2
13/2
Jf

These were averaged over the different lengths of cascade, weighting with the quantities P(n) of table 2. Thus for each J_i we know the fraction of the initial population which finally arrives at the higher spin state. If $J_c = 1$ we then use table 1 to average these results over the relative probabilities of different J_i. For targets with $J_o \neq 0$, the whole of this procedure was carried out for the three possible values of J_c, then a further weighted average formed over $P(J_c)$. (Tables for $P(J_i)$ for half-integral J_c were prepared but have not been included here.) It is seen that the process consists in forming weighted means, firstly over P(n), then $P(J_i)$, then if necessary over $P(J_c)$.

A more general procedure than this was finally adopted for the most common case of $J_c = 1$ in a medium-weight nucleus. This consisted in calculating $P(J_f)$ as a function of σ, i.e. the weighting over P(n) and $P(J_i)$ has been carried out before the spins of the isomeric levels are decided. From these results (Table 3), it is possible to calculate very simply the ratio for any given pair of spins, for a target nucleus with $J_o = 0$.

Figure 23 illustrates the results given in Table 1 and Table 3. It shows the dependence of $P(J_i)$ and $P(J_f)$ on σ, for the case $J_c = 1$. It is apparent that the value of σ has only a small influence on the distribution of spins directly after the neutron emission, but has a large effect on the broadening process during the gamma-ray cascade.

Figure 24

Isomeric Ratios from Theory and Experiment

Curves of $\sigma_1/(\sigma_1 + \sigma_2)$ are shown for some choices of competing spins; subscripts 1 and 2 denote respectively the levels of high and low spin. The corresponding experimental results are shown. The dotted lines show how the value of σ and its uncertainty is obtained from the experimental ratio.

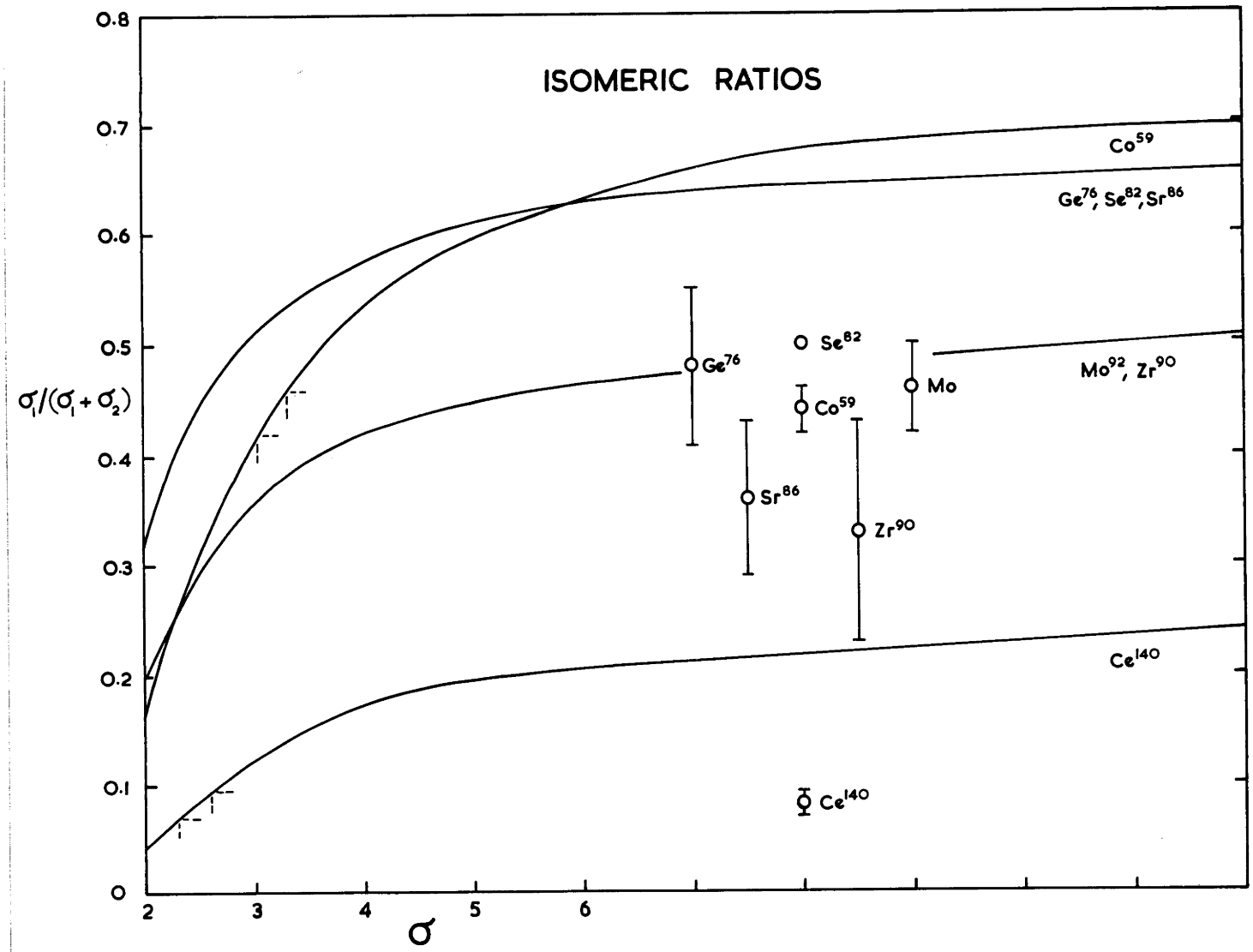
ISOMERIC RATIOS
0.8
0.7
0.6
0.5
0.4
0.3
0.2
0.1
0
$\sigma_1/(\sigma_1+\sigma_2)$
2
3
4
5
6
σ
Co^{59}
$Ge^{76}, Se^{82}, Sr^{86}$
Mo^{92}, Zr^{90}
Ce^{140}
Ge^{76}
Se^{82}
Co^{59}
Mo
Sr^{86}
Zr^{90}
Ce^{140}

Table 3

$P(J_f)$ as a Function of σ, for a medium-weight nucleus

J_f \ σ	2	3	4	5	∞
1/2	0.254	0.155	0.125	0.112	0.091
3/2	0.436	0.337	0.301	0.286	0.250
5/2	0.239	0.312	0.309	0.308	0.302
7/2	0.063	0.149	0.186	0.194	0.218
9/2	0.008	0.037	0.064	0.078	0.101
11/2	0	0.008	0.013	0.019	0.032
13/2	0	0.002	0.002	0.003	0.006

The final result of the calculations is a set of the quantities $\frac{\sigma_1}{\sigma_1 + \sigma_2}$ as a function of σ, where σ_1 and σ_2 are the respective cross-sections for population of the high- and the low-spin level. (The isomeric level does not always have the higher spin.) Such results are graphed in figure 24, for some given pairs of isomer spins. From comparison of such a graph with the experimental ratio the best value of σ can be deduced.

3. Experimental Method

The samples were irradiated close to the donut of the synchrotron; the intensity of the 30 MeV bremsstrahlung beam was monitored with tantalum disks placed on each side of the sample, in a similar way to that described in Chapter 4. In

a few cases (e.g. Co^{58} and Br^{80}) the decay of the ground state activity made known the initial populations of both levels and monitoring was not required. Usually, however, irradiations of different length were needed for separate study of each level; such measurements were related through the tantalum activity. No attempt was made to obtain absolute cross sections.

Most of the samples were contained as the metal or oxide powder in $\frac{3}{4}$ in. diameter by $\frac{1}{4}$ in. aluminium cans, though some metals were as $\frac{3}{4}$ in. diameter foil disks. The form of target material is listed in Table 4 (section 3.1).

The NaI scintillation spectrometer described in Chapter 4 was used for all measurements of residual activity. Extensive use was made of single-channel analyzers set over prominent photopeaks, especially for the very short activities (e.g. 49 sec. Ce^{139}). Two scalers connected to a change-over switch alternately recorded the pulses from the analyzer. The switch was operated every 15 seconds for such short activities; no counts were lost and very good decay curves were obtained.

In the calculation of results corrections were made for the following:

(1) Contributions from weaker peaks from the nuclide being measured;

(2) Self-absorption (using the method of Chapter 3, section 3);

(3) Variation of crystal detection efficiency and photofraction with gamma-ray energy, (using the curves of Vegors et al. (Ve 58)).

Decay curves were usually analyzed by the least squares technique, though sometimes in simple cases by the method of Perkel (Pe 57).

3.1 Decay Schemes

In Table 4 are summarized the important data for the nuclides studied. The decay schemes used were taken from the Nuclear Data Sheets (N.D.S. 59), except when more recent information was available. Some of these schemes are still not very well known. Notes on nuclei which gave difficulty for this or some other reason are given below.

Se^{74} The decay scheme of $Se^{73, 73m}$ is not well known (Ri 60). This is unfortunate because as both levels decay by positron emission the experimental measurement is fairly easy. It is not certain which level lies higher, or whether there is an isomeric transition between them. The analysis was carried out following Ricci's suggestion that there is none.

Ge^{76} The conversion coefficient of the 0.139 gamma-ray from Ge^{75m} has not been measured. The value obtained from interpolation of the tables of Rose (Ro 58) was $\alpha = 1.55$, assuming a pure E3 transition.

Mo^{92} Both the isomeric and ground states of Mo^{91} emit

Table 4 Details of Isomeric Pairs Measured

Target Nucleus				Residual Nucleus										Remarks
				Metastable State					Ground State					
Nucleus	%	J_o	Form of Target	T	J_A	E_γ	t_i	p_1	T	J_B	E_γ	t_i	J_{int}	
Co^{59}	100	7/2	Metal Cylinder	9.2 h	5^+	-	6 h	1	71.3 d	2^+	γ^+	6 h	-	(a)
Se^{74}	0.87	0	Powdered element	44 m	$\frac{1}{2}$?	γ^+	60 m	0 ?	7.1 h	$\frac{9}{2}^+$	γ^+	60 m	-	(b)
Ge^{76}	7.7	0	Powdered element	48 s	$\frac{7}{2}^+$	0.139	60 s	1	82 m	$\frac{1}{2}^-$	0.264	60 m	-	(b)
Br^{81}	49.5	3/2	Compressed NaBr	4.4 h	5^-	-	30 m	1	17.6 m	1^+	0.62	30 m	2^-	(a)
Sr^{86}	9.9	0	$SrCO_3$	70 m	$\frac{1}{2}^-$	0.225	60 m	0.86	64 d	$\frac{9}{2}^+$	0.513	6 h	$7/2^+$	
Zr^{90}	51.5	0	Powdered element	4.4 m	$\frac{1}{2}^-$	0.588	5 m	0.93	79 h	$\frac{9}{2}^+$	0.913	6 h	-	
Mo^{92}	15.9	0	Powdered element	66 s	$\frac{1}{2}^-$	γ^+	2 m	0.57	15.5 m	$\frac{9}{2}^+$	γ^+	2 m	-	
Ag^{107}	51.4	$\frac{1}{2}$	Metal foil	24 m	1^+	γ^+	30 m	0	8.2 d	6^+	0.513	6 h	-	(c)
In^{113}	4.2	9/2	Metal foil	20.7 m	4^+	-	15 m	1	15 m	1^+	γ^+	15 m	-	(a)
Cd^{116}	7.6	0	Metal foil	43 d	$\frac{11}{2}^-$	0.335	6 h	0	53 h	$\frac{1}{2}^+$	0.335	6 h	-	(d)
Sb^{121}	57.3	5/2	Powdered element	5.8 d	?	1.18	6 h	0	16.4 m	1^+	γ^+	15 m	-	(e)
Te^{122}	2.5	0	TeO_2	154 d	$\frac{11}{2}^-$	-	6 h	1	17 d	$\frac{1}{2}^+$	0.575	6 h	$3/2^+$	(a), (d)
Te^{130}	34.5	0	"	33 d	$\frac{11}{2}^-$	0.49	6 h	1	72 m	$\frac{3}{2}^+$	0.49	60 m	-	(d)
Ce^{140}	88.5	0	Ce O	55 s	$\frac{11}{2}^-$	0.74	1 m	1	140 d	$\frac{3}{2}^+$	0.165	6 h	-	
Au^{197}	100	3/2	Metal foil	9.2 h	11^+	-	6 h	1	6.1 d	2^-	0.354	6 h	7^-	
Hg^{198}	10.0	0	Liquid metal	24 h	$\frac{13}{2}^+$	0.133, X-rays	6 h	0.97	65 h	$\frac{1}{2}^-$	0.077, X-rays	6 h	$5/2^-$	(f)

- % Isotopic Abundance
- J_o Spin of target in ground state
- T Half-life
- J_A Spin of metastable level
- J_B Spin of ground state
- J_{int} Spin of intermediate level (where applicable)
- E_γ Energy of gamma-ray studied (in MeV)
- p_1 Fraction of isomeric level decay reaching ground state
- t_i Length of irradiation used.

(a) Follow ground state decay only
(b) Decay scheme not well known
(c) Complex decay scheme, with many gamma-rays
(d) Weak activities
(e) Spin of isomeric level not known
(f) Analysis of data rather difficult

positrons, and the isomeric transition gamma-ray has energy 0.658 MeV. As gamma-rays of energy 1.21 and 1.54 MeV are also emitted, analysis of the data requires careful correction for contributions of the gamma-rays in the 0.511 MeV peak. This was done using the decay scheme and the efficiency tables of Vegors et al. (Ve 58).

Ag^{107} The decay scheme of Ag^{106m} is very complicated (Ro 60). As many gamma-rays contribute in the region of the 0.513 peak, high accuracy in this case cannot be expected.

Sb^{121} The spin of the 5.8 d Sb^{120m} level is not known, though the level is known to decay by electron capture to 7^- and 6^+ levels in Sn^{120}. It was hoped that measurement of the isomer ratio would allow a useful suggestion as to its value.

Te^{122}, Te^{130} Owing to the large number of stable Te isotopes, very confused spectra were obtained. Most of the activities were also quite weak. Although considerable effort was put into the analysis the results are not very reliable.

Au^{197} The existence of a 9.5h isomer level in Au^{196} has been recently proved (Ka 60a). Although the ground state activity was abundant after a 6 hr irradiation no 9h activity was observed. This is understandable as the separation will be between an 11^+ and a 7^- level, which means that the isomer level is populated in a negligibly small proportion of the transitions.

Hg^{198} Although the activity of both levels in Hg^{197} is easily observed, analysis of the results is quite difficult. The low-

energy gamma-rays emitted are mixed with X-rays from a number of sources (Va 60). The L/K capture ratio of Hg^{197} is not known, though an estimate was made by Vandenbosch. The counting was done with the sample 3 cm above the crystal, to reduce summing effects.

3.2 Analysis of Results

A sufficiently general diagram of an isomeric pair of levels is shown as an inset in figure 22; p_1 is the fraction of the decays of level A which proceed to level B. If, at a time t after the end of an irradiation the populations of the two levels are A and B, respectively, then the following relations hold for the decay of each level:

$$\frac{dA}{dt} = -A\lambda_A \qquad (1)$$

$$\frac{dB}{dt} = -B\lambda_B + p_1 A\lambda_A . \qquad (2)$$

These can be solved in terms of the initial populations A_o and B_o;

$$A = A_o e^{-\lambda_A t} \qquad (3)$$

$$B = B_o e^{-\lambda_B t} + p_1 A_o \left(\frac{\lambda_A}{\lambda_A - \lambda_B}\right)\left[e^{-\lambda_B t} - e^{-\lambda_A t}\right]. \qquad (4)$$

The decay rate of level B is $B\lambda_B$; from rearrangement of (4) we have

$$B\lambda_B = e^{-\lambda_A t}\left[-p_1 A_o \frac{\lambda_A \lambda_B}{\lambda_A - \lambda_B}\right] + e^{-\lambda_B t}\left[B_o\lambda_B + p_1 A_o \frac{\lambda_A\lambda_B}{\lambda_A - \lambda_B}\right] \qquad (5)$$

$$= A' e^{-\lambda_A t} + B' e^{-\lambda_B t}, \text{ say.} \qquad (6)$$

If the isomer level decays to the ground state and if the half-

lives are of the same order of magnitude it is possible to deduce both A_o and B_o from the decay curve of the ground state activity. Analysis of the decay curve (6) gives A' and B', (one of which may be negative).

Then

$$A_o = A' \left(\frac{\lambda_B - \lambda_A}{p_1 \lambda_A \lambda_B} \right), \tag{7}$$

$$B_o = \frac{B' + A'}{\lambda_B} \quad . \tag{8}$$

Hence $$\frac{B_o}{A_o} = p_1 \left(\frac{\lambda_A}{\lambda_B - \lambda_A} \right) \left(1 + \frac{B'}{A'} \right) \quad . \tag{9}$$

Some care is necessary when (6) is solved by the usual least-squares method using total counts in given time intervals, as this involves an integration over the counting interval. The constants obtained are $A'' = \frac{A'}{\lambda_A}$ and $B'' = \frac{B'}{\lambda_B}$. Substitution in (9) gives

$$\frac{B_o}{A_o} = p_1 \left(\frac{\lambda_A}{\lambda_B - \lambda_A} \right) \left[1 + \frac{B''}{A''} \frac{\lambda_A}{\lambda_B} \right]. \tag{10}$$

In cases in which $p_1 = 0$, i.e. the isomer level does not decay to the ground state, the decay of each level is treated independently.

During the irradiation, if $p_1 \neq 0$, the decay of the isomer level will increase the population of the ground state. Let the rate of production of nuclei in a given level be given by $I_o \sigma$,

where σ is the cross section and I_o includes the X-ray intensity and the number of target atoms. (The σ here has no relation to σ of the spin distribution.) Conditions during the irradiation are described by the equations:

$$\frac{dA}{dt} = I_o \sigma_A - A\lambda_A \tag{11}$$

$$\frac{dB}{dt} = I_o \sigma_B + p_1 A \lambda_A - B\lambda_B . \tag{12}$$

The respective populations after an irradiation of length t_i are then

$$A_o = \frac{I_o \sigma_A}{\lambda_A}\left[1 - e^{-\lambda_A t_i}\right] \tag{13}$$

$$B_o = I_o\left\{\frac{\sigma_B}{\lambda_B}(1 - e^{-\lambda_B t_i}) + p_1\sigma_A\lambda_A\left[\frac{1}{\lambda_A\lambda_B} + \frac{e^{-\lambda_A t_i}}{\lambda_A(\lambda_A-\lambda_B)} - \frac{e^{-\lambda_B t_i}}{\lambda_B(\lambda_A-\lambda_B)}\right]\right\} . \tag{14}$$

Define $$K_1 = \left(\frac{\lambda_B - \lambda_A}{\lambda_A}\right)\left(1 - e^{-\lambda_A t_i}\right) \tag{15}$$

$$K_2 = \left(\frac{\lambda_B - \lambda_A}{\lambda_B}\right)\left(1 - e^{-\lambda_B t_i}\right) \tag{16}$$

$$K_3 = p_1\left[-\frac{\lambda_A}{\lambda_B}(1 - e^{-\lambda_B t_i}) + (1 - e^{-\lambda_A t_i})\right] . \tag{17}$$

Then $$\frac{\sigma_B}{\sigma_A} = \frac{(B_o/A_o)K_1 - K_3}{K_2} \qquad \text{(General case)}. \tag{18}$$

This equation still holds if $p_1 = 0$.

For the useful case in which A_o and B_o can be derived from analysis of the ground state decay curve (equation (6)), we have,

by substitution of (9) into (18),

$$\frac{\sigma_B}{\sigma_A} = p_1 \frac{\lambda_A}{\lambda_B - \lambda_A} \left[1 + \frac{B'}{A'} \frac{(1 - e^{-\lambda_A t_i})}{(1 - e^{-\lambda_B t_i})} \frac{\lambda_B}{\lambda_A} \right] . \qquad (19)$$

This equation was first stated by Katz et al. (Ka 52).

A useful approximation can be found for the case (e.g. Ce^{139}), in which the isomer level is very short-lived and the ground state has a long half-life. For the long irradiation required for measurement on the ground state, we can put

$$\lambda_B << \lambda_A , \quad \lambda_A t >> 1 .$$

Then, from (14),

$$B_o \approx I_o \left[\frac{\sigma_B}{\lambda_B} (1 - e^{-\lambda_B t_i}) + p_1 \frac{\sigma_A}{\lambda_B} (1 - e^{-\lambda_B t_i}) \right]$$

$$= I_o \left[\frac{(1 - e^{-\lambda_B t_i})}{\lambda_B} (\sigma_B + p_1 \sigma_A) \right] .$$

Thus $$\sigma_B + p_1 \sigma_A = \frac{B_o \lambda_B}{I_o (1 - e^{-\lambda_B t_i})} \qquad \text{(Special case).} \qquad (20)$$

A separate measurement gives σ_A in terms of I_o, so that σ_A and σ_B are obtained separately.

4. Experimental Results

In Table 5 are listed the isomer ratios obtained, together with four from other workers. Values of σ were deduced from these results by the methods of section 2, adopting J-values of competing levels as shown in the table.

Table 5

Isomer Ratios from (γ,n) Reactions

Target Nucleus	J_o	Competing Levels g.s.	Competing Levels i.s.	$\frac{\sigma_1}{\sigma_1 + \sigma_2}$	σ
Co^{59}	7/2	2^+	5^+	0.44 ± 0.02	3.2 ± 0.2
Se^{74}	0	$9/2^+$	$\frac{1}{2}$?	0.77	$> \infty$
Ge^{76}	0	$\frac{1}{2}^-$	$7/2^+$	0.48 ± 0.07	$2.8 \pm 0.5 \atop - 0.4$
Br^{81}	3/2	2^- *	5^-	0.32 ± 0.02	$6.4 \pm 1.2 \atop - 1.0$
"	"	1^+ ?	"	" "	3.2 ± 0.3
Sr^{86}	0	$7/2^+$ *	$\frac{1}{2}^-$	0.36 ± 0.07	$2.2 \pm 0.4 \atop - 0.3$
"	"	$9/2^+$?	"	" "	$3.1 \pm 0.8 \atop - 0.6$
Zr^{90}	0	$9/2^+$	$\frac{1}{2}^-$	0.33 ± 0.10	$2.8 \pm 0.8 \atop - 0.6$
Mo^{92}	0	$9/2^+$	$\frac{1}{2}^-$	0.46 ± 0.04	$6 \pm 4 \atop - 2$
"	"	$7/2$?	"	" "	2.7 ± 0.3
Ag^{107}	1/2	1^+	6^+	0.04 ± 0.02	2.0 ± 0.2
In^{113}	9/2	1^+	4^+	0.82 ± 0.1	$3.1 \pm 0.8 \atop - 0.6$
Cd^{116}	0	$\frac{1}{2}^+$	$11/2^-$	$\leqslant 0.2$	$\leqslant 3$
Sb^{121}	5/2	1^+	8 ?	0.084 ± 0.01	2.9 ± 0.2
"	"	1^+	9 ?	" "	3.4 ± 0.3
Te^{122}	0	$3/2^+$ *	$11/2^-$	~ 0.3	$> \infty$
Te^{130}	0	$3/2^+$	$11/2^-$	~ 0.3	$> \infty$
Ce^{140}	0	$3/2^+$	$11/2^-$	0.08 ± 0.01	2.5 ± 0.2
Hg^{198}	0	$5/2^-$	$13/2^+$	0.05 ± 0.01	$3.4 \pm 0.5 \atop 0.4$
Br^{81} (Ka 52)	3/2	2^- *	5^-	0.33	6.4
Se^{82} (Si 56)	0	$\frac{1}{2}^-$	$7/2^+$	$0.5(\pm 0.05?)$	3.0 ± 0.5
Zr^{90} (Ka 53)	0	$9/2^+$	$\frac{1}{2}^-$	0.44 ± 0.06	$4.5 \pm 2 \atop - 1$
In^{115} (Go 53)	9/2	1^+	5^+	0.85	5.0

σ_1 and σ_2 are respectively the cross sections to the high- and low-spin levels

* Intermediate level

Estimation of the uncertainty in a measured ratio was often difficult, as it depended, e.g., on the accuracy of the published decay scheme. Corrections for disturbing gamma-rays were important with Mo^{92} and Ag^{107}. It was usually assumed that a single cross section could be measured to $\pm$ 10% unless some special reason made the accuracy less than this. Higher accuracy was possible with Co^{59} and Br^{80}, each needing only analysis of a single decay curve.

The magnitude of σ and its estimated uncertainty were obtained from plots of $\frac{\sigma_1}{\sigma_1 + \sigma_2}$ such as those shown in figure 24. The quantity σ_1/σ_2, which gives curves of similar shape, was plotted in a few cases. Although such curves naturally gave the same result for σ, its uncertainty was sometimes reduced. The quoted uncertainty in σ contains no allowance for possible inadequacies of the theoretical treatment, which are difficult to estimate.

The shape of the theoretical curves has two effects:

(1) The error bars on σ may be unsymmetrical with the positive one larger;

(2) The uncertainty in σ depends just as much on which portion of the curve the result falls, as on the accuracy of the measurement (compare Ag^{107} and Mo^{92}).

For the nuclei Br^{81}, Sr^{86}, Mo^{92} and Sb^{121} two choices of pairs of competing levels have been treated. These are

discussed in section 5.2.

The results for Se^{74}, Te^{122} and Te^{130} are rather meaningless at present. Little can be done with Se^{74} until the decay scheme is better known, though it might be possible by making irradiations of different lengths to measure p_1 and find out which is the upper level. Measurements on Te and Cd should be repeated with higher activities.

5. Discussion

5.1 Comparison with other Work

Of those nuclei studied here, similar measurements on Mo^{92} and Zr^{90} (Ka 53) and on Br^{81} (Ka 52) have been made previously. Unfortunately, the decay scheme of Mo^{91} was not well known at the time and an incorrect one was adopted; it is therefore not possible to compare the two measurements. For the other two nuclei we find good agreement. Thus Katz obtained $\frac{\sigma_B}{\sigma_A} \simeq 2.0$ for Br^{80}, corresponding to $\frac{\sigma_1}{\sigma_1 + \sigma_2} \simeq 0.33$ (present figure 0.32 ± 0.02); for Zr^{89} the average ratio $\frac{\sigma_B}{\sigma_A}$ between 16 and 26 MeV was 0.8 ± 0.1, or $\frac{\sigma_1}{\sigma_1 + \sigma_2} = 0.44 \pm 0.06$ (present result 0.33 ± 0.1).

There are now two nuclei for which σ has been derived from the isomer ratio after different types of reaction. Vandenbosch and Huizenga (Va 60) showed that the isomer ratios for Hg^{197} formed in six different reactions were consistent with $\sigma = 4 \pm 1$

Figure 25

Measurements of σ

The results for σ from the present experiment and those of other workers are plotted against A. The upper curve indicates roughly where the points would lie if the moment of inertia were always that of a rigid body, and the other curves correspond to respectively one-half and one-quarter of this.

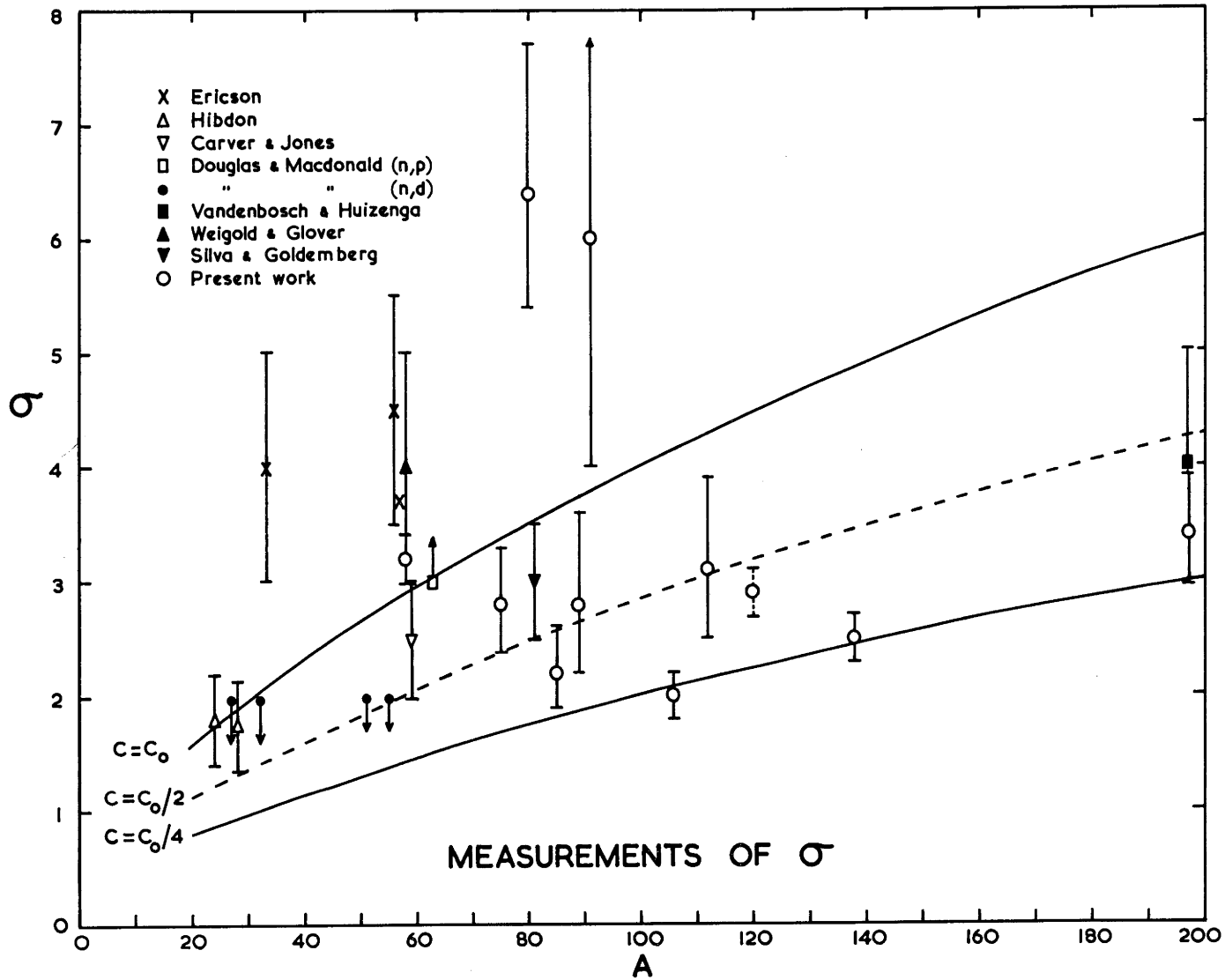
X Ericson
Δ Hibdon
▽ Carver & Jones
□ Douglas & Macdonald (n,p)
● " " (n,d)
■ Vandenbosch & Huizenga
▲ Weigold & Glover
▼ Silva & Goldemberg
○ Present work
C=C₀
C=C₀/2
C=C₀/4
MEASUREMENTS OF σ
σ
A
0
1
2
3
4
5
6
7
8
0
20
40
60
80
100
120
140
160
180
200

(The actual isomer ratios σ_B/σ_A ranged from 0.044 to 1.0.) Weigold and Glover (We 61) found that similar measurements for three reactions producing Co^{58} were consistent with $\sigma \sim 3.5$. The present result is consistent in each case. Such agreement from results of different reactions, for which the isomer ratios often differ remarkably, provides good justification for the assumptions used in the calculations.

5.2 Variation of σ with A

Results for σ are shown in figure 25. As well as from the present work, they come from the following sources:

(1) Hibdon's (Hi 59, Hi 61) assignment of spin values to a number of levels of Na^{24} and Al^{28}. He obtains $\sigma = 1.8$ for Na^{24} and 1.7 for Al^{28}, with uncertainties probably less than 0.5.

(2) Comparison of the number of levels with a given spin with the total number of levels. Ericson (Er 59) finds ~~for~~ $\sigma \sim 4$ for S^{33}, ~ 4.5 for Mn^{56} and ~ 3.7 for Fe^{57}. For Cu^{59}, Carver and Jones (Ca 60b) obtain $\sigma = 2.5 \pm 0.4$.

(3) Analysis of isomeric ratios from particle-induced reactions. Vandenbosch and Huizenga obtained $\sigma = 4 \pm 1$ for Hg^{197}. Weigold and Glover (We 61) analyzed various measurements on Co^{58}. Their own result from $Co^{59}(n,2n)$ is 4 ± 1, but their analysis of other published data favours a result closer to 3.5.

(4) Study of anisotropy of angular distributions from compound nucleus processes. Douglas and Macdonald (Do 59)

obtained the results shown.

(5) The isomer ratio after the $Se^{82}(\gamma,n)Se^{81}$ reaction was measured by Silva and Goldemberg (Si 56). As analysis of the ground state decay curve was all that was required this result should be fairly accurate.

The result for Sb^{120}, assuming competition between spins 1 and 8, has been dotted in. Choice of J = 9 would give σ rather too high.

The curves in the figure show the expected variation of σ corresponding to $C = C_o$, $C_o/2$ and $C_o/4$ respectively. To obtain these it was necessary to adopt some approximation for the temperature t. From Lang and Le Couteur (La 54)

$$U = at^2 - t \ . \qquad (1)$$

Adopting $a \sim \frac{A}{8}$ and $U \sim 4$ MeV, we obtain

$$t \simeq 5.6\ A^{-\frac{1}{2}} \text{ MeV}. \qquad (2)$$

(From equation (4) of section 1.1, it follows that the nuclear temperature τ is given by

$$\tau \simeq 5.6/(A^{\frac{1}{2}} - 1) \text{ MeV}.) \qquad (3)$$

The results give a reasonably consistent picture except for those of Br^{80} and Mo^{91}. Such large discrepancies cannot be attributed to experimental error and it seems likely that the spins of the competing levels are different from those adopted. Table 5 shows that a great improvement is possible if it can be assumed that the competing spins are 1 and 5 for Br^{80} and 1/2 and 7/2 for Mo^{91}. It is difficult to see how this can hold for

Br^{80}, unless for some unknown reason (probably connected with parity conservation), the intermediate $J = 2^-$ level does not compete. For Mo^{91}, it is possible that a level of spin 7/2 lies above the isomeric level, competes with it and decays directly to the ground state. This must remain conjecture at present. A better result for Sr^{85} is obtained if it is again believed that the intermediate level does not compete, but the experimental ratio is here not as well-established.

Examination of figure 25 suggests that the moment of inertia is close to the rigid-sphere result for the lighter nuclei and falls slowly with increasing A to about one quarter of this. However, shell structure effects, which are often substantial, have not yet been included. A more detailed analysis is therefore presented in the next section.

5.3 Effects of Shell Structure

It was shown by Newton (Ne 56) that C is related to $\overline{m^2}$, the mean square magnetic quantum number m of the individual nucleons by

$$C = \overline{m^2}\, g \quad , \tag{1}$$

where g is the density of single-particle states at the Fermi energy. ($g = \frac{6}{\pi^2}\, a$, where a is the usual parameter of level density formulae.) He also showed that g could be well represented by

$$g = K \left(\overline{j_n} + \overline{j_z} + 1 \right) A^{2/3} , \qquad (2)$$

where K is a constant to be determined empirically and $\overline{j_n}$ and $\overline{j_z}$ are means of j-values for neutrons and protons respectively close to the Fermi level. Lang (La 61) gives a revised figure for K of 0.0455, 20% higher than Newton's result. Jensen and Luttinger (Je 52) showed that the sequence of states in the shell model implies that

$$\overline{m^2} \simeq 0.146 A^{2/3} , \qquad (3)$$

with fluctuations about this of $\sim$ 10%. From (1), (2) and (3), taking Lang's value of K, we obtain

$$C = 0.00664 \left(\overline{j_n} + \overline{j_z} + 1 \right) A^{4/3} . \qquad (4)$$

This equation was used in the comparison with experiment, with $\overline{j_n}$ and $\overline{j_z}$ taken from Newton's tables. (The value of C from this equation will be denoted C_s, and the corresponding σ as σ_s.)

An attempt was made to improve on the former rough estimate of t. It was still taken from

$$U = a t^2 - t \qquad (5)$$

but with U (taken as the excitation energy at the beginning of the gamma-ray cascade) calculated separately for each nucleus, and a found from $a = \frac{\pi^2}{6} g$.

The results of this comparison are shown in Table 6. We first see that the ratio C_s/C_o is often much less than 1, reflecting the strong fluctuations of g with mass number (see inset of figure 26). In this figure are plotted the quantities

Figure 26

Comparison of σ from Experiment and Shell Theory

Results for σ/σ_s are plotted against A; the dotted line is to suggest the general trend of the points. For the two results plotted as squares see P. 110. As an inset is shown the quantity g, important in calculation of σ_s. Arrows indicate positions of the nuclei for which results are plotted.

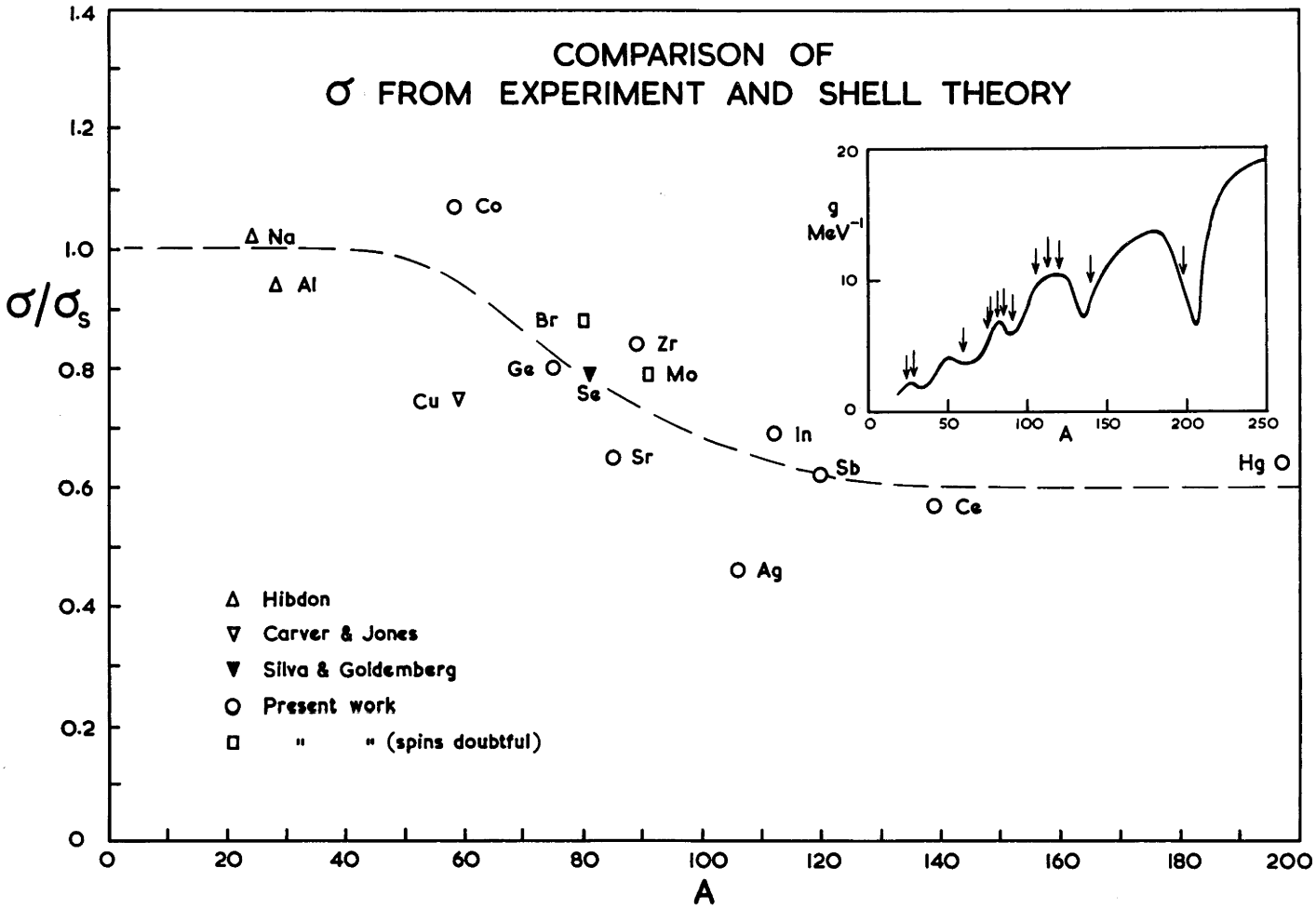
COMPARISON OF
σ FROM EXPERIMENT AND SHELL THEORY
σ/σS
A
Δ Na
Δ Al
O Co
Br □
O Zr
Ge O
Se ▼
□ Mo
Cu ∇
O In
O Sr
Sb O
Hg O
O Ce
O Ag
Δ Hibdon
∇ Carver & Jones
▼ Silva & Goldemberg
O Present work
□ " " (spins doubtful)
g MeV⁻¹
A

Table 6

Comparison of Experimental σ with Shell Theory

Residual Nucleus	J *	C_s (MeV^{-1})	t (MeV)	σ_s	σ/σ_s	C/C_s	C_s/C_o	C/C_o
Na^{24} (Hi 61)	12	2.75	1.18	1.76	1.02	1.04	1.02	1.06
Al^{28} (Hi 59)	$9\frac{1}{3}$	2.63	1.35	1.85	0.94	0.88	0.78	0.69
Co^{58}	12	8.95	0.98	3.0	1.07	1.14	0.78	0.89
Cu^{59} (Ca 60b)	$9\frac{1}{3}$	7.12	1.56	3.3	0.75	0.57	0.62	0.35
Ge^{75}	14.7	15.4	0.80	3.5	0.80	0.64	0.88	0.56
Br^{80}	16	18.4	0.72	3.6	1.8 or 0.88	0.77?	0.94	0.73?
Se^{81} (Si 56)	16	18.6	0.77	3.8	0.79	0.62	0.94	0.58
Sr^{85}	14.7	18.5	0.63	3.4	0.65	0.42	0.88	0.37
Zr^{89}	13.9	18.4	0.61	3.3	0.84	0.70	0.80	0.56
Mo^{91}	19.7	26.9	0.43	3.4	1.8 or 0.79?	0.62?	1.12	0.70?
Ag^{106}	20	33.3	0.58	4.4	0.46	0.21	1.06	0.22
In^{112}	19.6	35.0	0.58	4.5	0.69	0.48	1.03	0.50
Sb^{120}	18.8	37.9	0.58	4.7	0.62	0.38	0.99	0.38
Ce^{139}	12.4	29.6	0.66	4.4	0.57	0.32	0.60	0.19
Hg^{197}	13.2	50.2	0.56	5.3	0.64	0.41	0.57	0.23

* $J = 2\,(\overline{j_n} + \overline{j_z} + 1)$

σ/σ_s. The results indicated by squares are those for Br^{80} and Mo^{91}, assuming that the competing J-values can be modified as suggested in section 5.2. The good fit of both points seems to justify these changes. The points for Sr^{85} and Ag^{106} fall below the general trend, but this could be due to inaccurate measurement in each case.

5.4 Conclusions

The trend of the points in figure 26 is a good deal smoother than in figure 25, showing that for the excitation energies reached here, the shell model moment of inertia is a more natural standard of comparison than the rigid sphere result. The ratio σ/σ_s tends to unity for $A \lesssim 40$ and levels off at about 0.6 for $A \gtrsim 100$, with a transition region in between. Hence the moment of inertia found in the present experiment is close to the shell model prediction for light nuclei and falls to about 35% of it for heavy nuclei. This corresponds to from 0.2 to 0.4 of the rigid body value, as shown in Table 6.

We need to know if the fall in the measured moment of inertia is due to the decrease in E_m with A, leading to lower excitation in the heavy nuclei. Calculation of the excitation energy at the beginning of the gamma-ray cascade yields the following approximate results (in MeV):

Co^{58} 5.3, Ge^{75} 5.7, Se^{81} 6.0, Br^{80} 5.1, Sr^{85} 3.7, Zr^{89} 3.3,
Mo^{91} 2.3, Ag^{106} 5.1, In^{112} 5.3, Sb^{120} 4.9, Ce^{139} 4.7,

$Hg^{197} \sim 4.7$ (S_n for Hg^{198} is not known). The downward trend is small and we conclude that the decrease in $\mathcal{I}$ with A is a real effect.

It is interesting to compare with the conclusions of Lang and Le Couteur (La 59), who calculated pairing-energy effects in excited nuclei. They find that, at low energies, excitation of pairs is more important than excitation of single particles. Most of the angular momentum is carried by excited pairs and the moment of inertia is just half that of a rigid sphere. They therefore expect the rigid body value in the lighter nuclei falling to half this for heavy elements.

In the present work it appears that the excitation energy per nucleon in the heavy nuclei is too small to produce this effect and the moment of inertia is approximately that found near the ground state. However, in the lighter nuclei the moment of inertia is close to that predicted by the shell model.

5.5 Suggestions for Further Work

Both the experimental results and the calculations made in this work could certainly be improved. It is desirable to know if the deviations shown by Sr^{85} and Ag^{106} are real or due to inaccurate measurement. The calculations could be repeated in detail for each nucleus, though the answers would probably not be very different.

Further work would probably relate to the variation of σ

with excitation energy and details of the influence of shell structure. It may be useful to measure the variation of isomer ratio with photon energy in a few more cases. A good one for this purpose would be Co^{59}, as the experiment can be done accurately and σ is defined within narrow limits by a good measurement. It would be interesting to see if the variation of the isomer ratio with energy is similar in a heavy nucleus.

The detailed influence of shell structure on σ could perhaps be investigated by accurate comparison of two isomeric pairs in the same element. This should be possible for Sb, Cd and Te, if sufficiently high activities can be produced.

Theoretical treatment of the whole isomer ratio problem could be improved, probably along the lines of Troubetzkoy (Tr 61).

The study of isomer ratios following (γ,n) reactions appears to have given some useful information on nuclear structure, and the method can probably be developed further.

Figure 27

Geometry for Calculations

This figure illustrates the geometry for the calculations of Appendix A and Appendix C.

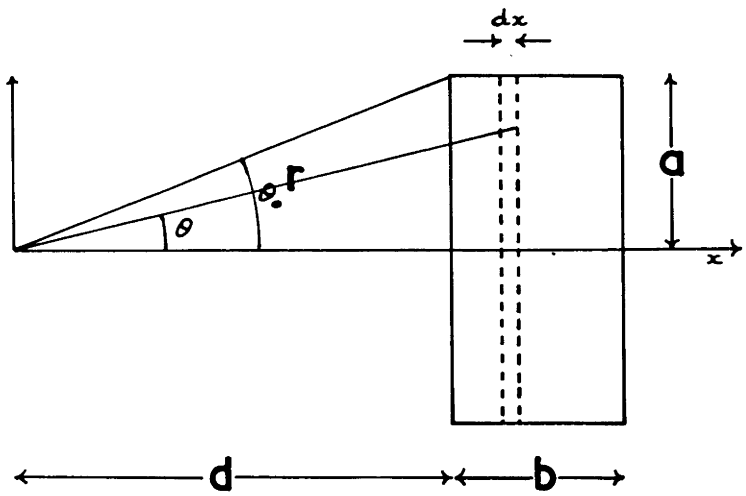

A

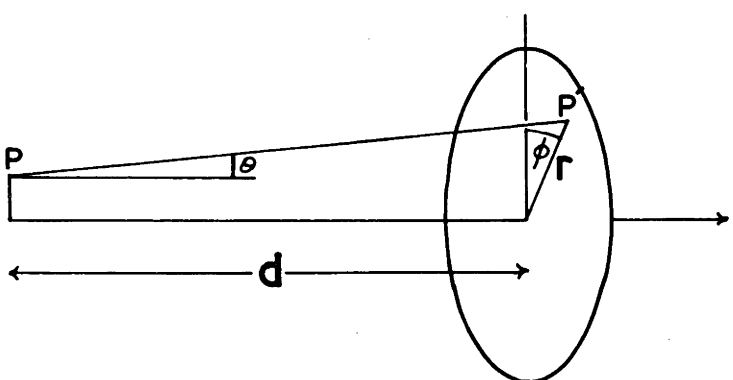

B

APPENDIX A

Activity induced in a disk irradiated near a point source

First calculate the activity induced in a thin slice of thickness dx, at distance x from the target (figure 27 A).

The number of reactions / sec in a ring of radius r sin θ, subtending an angle $d\theta$ at the source, is

δ_n = (Intensity I in photons/(sterad.)(sec)) . (cross section x number of target atoms/cm^3)(= k say) . (solid angle subtended) . (effective thickness)

$$= I \cdot k \cdot 2\pi \sin\theta \, d\theta \cdot dx/\cos\theta \cdot$$

Therefore the total number of reactions/sec in the thin slice is

$$n = \int \delta_n = 2\pi \, k \, I \, dx \int_o^{\theta_o} \tan\theta \, d\theta$$

$$= - 2\pi \, k \, I \, dx \left[\ln \cos\theta \right]_o^{\theta_o}$$

$$= \pi \, k \, I \ln \left(1 + \frac{a^2}{x^2}\right) dx \quad .$$

If $\frac{a^2}{x^2} \ll 1$, this reduces to $\pi \, k \, I \, \frac{a^2}{x^2} \, dx$ as it should.

The number of reactions/sec in the disk is obtained by an integration w.r.t. x. (The absorption of the γ-rays is fairly small and will be neglected.)

$$N = \int n \, dx = \pi \, k \, I \int_d^{d+b} \ln \left(\frac{x^2 + a^2}{x^2}\right) dx$$

$$= \pi \, k \, I \left[x \ln \left(\frac{x^2 + a^2}{x^2}\right) + 2a \tan^{-1} \frac{x}{a} \right]_d^{d+b}$$

/cont.

$$= \pi k I \left\{ \left[(d+b) \ln \left(1 + \frac{a^2}{(d+b)^2} \right) - d \ln \left(1 + \frac{a^2}{d^2} \right) \right. \right.$$

$$\left. \left. + 2a \tan^{-1} \left[\frac{ab}{a^2 + d(d+b)} \right] \right] \right\}$$

$$= \pi k I K_o \text{ , say.}$$

For $b \ll d$ this reduces to $\pi k I b \ln \left(1 + \frac{a^2}{d^2}\right)$, as required.

APPENDIX B

Corrections for Anisotropic Gamma-ray Distribution

Assume the intensity at angle θ is given by

$$I(\theta) = I_o (1 + a \cos\theta + b \cos^2\theta) . \qquad (1)$$

The calculation in Appendix A is to be repeated with inclusion of the additional cosine factors.

(a) $\cos\theta$ term.

Yield from a thin slice:

$$dn = 2\pi k I \, dx \sin\theta \, d\theta$$

$$n = 2\pi k I \, dx (1 - \cos\theta_o)$$

$$= 2\pi k I \, dx \left(1 - \frac{x}{\sqrt{x^2 + a^2}}\right).$$

Yield from disk:

$$N = 2\pi k I \int_d^{d+b} \left(1 - \frac{x}{\sqrt{x^2 + a^2}}\right)$$

$$= \pi k I \cdot 2 \left[b - \sqrt{(d+b)^2 + a^2} + \sqrt{d^2 + a^2}\right]$$

$$= \pi k I \cdot K_1 \text{ say.}$$

(b) $\cos^2\theta$ term.

$$n = 2\pi k I \, dx \int_o^{\theta_o} \sin\theta \cos\theta \, d\theta$$

$$= \pi k I \, dx \left[\frac{a^2}{x^2 + a^2}\right]$$

$$N = \pi k I \int_d^{d+b} \frac{a^2}{x^2 + a^2} \, dx$$

$$= \pi k I \left[a \tan^{-1}\frac{d+b}{a} - a \tan^{-1}\frac{d}{a}\right]$$

$$= \pi k I \cdot K_2 \text{ say.}$$

K_o, K_1 and K_2 are computed from the known geometry, then for the distribution (1) we obtain the correction factor

$$\frac{\text{Yield (anisotropic)}}{\text{Yield (isotropic)}} = \frac{K_o + a\,K_2 + b\,K_3}{(1 + a + b)K_o} \quad .$$

A typical distribution for non-resonant radiation was

$$I(\theta) = I_o\,(1 - 0.02 \cos\theta + 0.22 \cos^2\theta) \quad .$$

For the close-up geometry we have

$$K_o = 0.2663,\ K_1 = 0.2021,\ K_2 = 0.1588 \quad .$$

Then $$\frac{\text{Yield}}{\text{Yield (isotropic)}} = 0.930$$

APPENDIX C

Variation in the Yield from a Disk due to a sideways Displacement of the Target Spot

The previous calculations have assumed that the radiation emanated from a point, whereas the true source was a 3/16 in. diameter disk. We wish to know the magnitude of error introduced by this assumption.

A thin disk of radius a is a distance d from the target, while the point source has been displaced a distance c from the axis (figure 27 B); θ is the angle between P P' and the normal to the disk.

The activity induced in an element of area at P' is proportional to (solid angle subtended at P by the element/cos θ).

Solid angle subtended by element

$$= \frac{r \, d\phi \, dr \cos\theta}{(PP')^2} \, .$$

$$(PP')^2 = (r\cos\phi - c)^2 + (r\sin\phi)^2 + d^2$$

$$= c^2 + d^2 + r^2 - 2cr\cos\phi \, .$$

The total number of reactions/sec in the disk is therefore given by

$$n = k\,I\,dx \int_0^a r\,dr \int_0^{2\pi} \frac{d\phi}{(c^2 + d^2 + r^2 - 2cr\cos\phi)}$$

$$= k\,I\,dx \int_0^a \frac{2\pi r\,dr}{\sqrt{(c^2 + d^2 + r^2)^2 - 4c^2r^2}}$$

$$= \pi\,k\,I\,dx \left[\ln\left(r^2 + d^2 - c^2 + \sqrt{(r^2+d^2-c^2)^2 + 4c^2d^2}\right) \right]_0^a$$

/cont.

$$= \pi k I\, dx \left[\ln(a^2 + d^2 - c^2 + \sqrt{(a^2+d^2-c^2)^2 + 4c^2d^2}) - \ln 2d^2 \right]$$

$$\simeq \pi k I\, dx \ln \left(1 + \frac{a^2 - c^2}{d^2} + \frac{c^2}{a^2 + d^2} \right)$$

neglecting terms of $O\left(\frac{c^4}{(a^2 + d^2)^2} \right)$.

For $c = 0$, this gives $\pi k I\, dx \ln \left(1 + \frac{a^2}{d^2}\right)$ as required (Appendix A).

For the close-up geometry:

$a = 0.375$ in, $d = 0.163$ in; let $c = 1/16$ in $= 0.062$ in, say.

Then $\frac{n\ (c = 0)}{n\ (c = 0.062)} = \frac{\ln 6.2928}{\ln 6.1715} = 1.011$.

Hence a quite significant change in the beam position makes only a 1% change in the yield, even in the poor geometry position.

For the good geometry arrangement,

$d = 0.620$ in; let c be again 0.062 in.

Then $\frac{n\ (c = 0)}{n\ (c = 0.062)} = 1.004$.

This gives good justification for treating the target as a point source in the Cu^{63} absolute measurement.

APPENDIX D

Unfolding of Bremsstrahlung Yield Curves

The yield $A(k_o)$, measured as a function of the bremsstrahlung peak energy k_o, is related to the reaction cross section $\sigma(k)$ by the Volterra integral equation

$$A(k_o) = \int_T^{k_o} \sigma(k)\, P(k, k_o)\, dk \quad , \tag{1}$$

where T is the reaction threshold and $P(k,k_o)$ the X-ray intensity function.

The R.H.S. of (1) is partially integrated, to give

$$A(k_o) = P(k_o,k_o)\int_T^{k_o} \sigma(k)dk - \int_T^{k_o}\left[P'(k_1,k_o)\int_T^{k_1} \sigma(k)dk\right]dk_1 \tag{2}$$

where $P'(k,k_o) = \frac{d}{dk} P(k,k_o)$.

If the integral over dk_1 is replaced by a summation, successive values of the integral over dk may be found from the corresponding quantities $A(k_o)$ by induction, since all terms except the last in the summation are composed of known quantities. The Euler-McLaurin formula was used to evaluate the integral. Denote

$$\int_T^{k} \sigma(k_1)\, dk_1 \quad \text{by} \quad S(k),$$

then

$$S(k_o) = \frac{A(k_o) + \frac{13}{12}hP'(k_o-h,k_o)S(k_o-h) + hP'(k_o-2h,k_o)S(k_o-2h)\cdots}{P(k_o,k_o) + \frac{5}{12}hP'(k_o,k_o)} \tag{3}$$

where h is the interval for k_o.

The Schiff (Sc 46) formula for $P(k,k_o)$ was adopted.

$$P(k,k_o) = \frac{1}{k}\left\{\left[1 + (1-z)^2\right] 2 \ln a - (2-z)^2\right\}$$

where $z = k / (k_o + \mu)$.

$$\frac{1}{a^2} = \frac{1}{a_1^2} + \frac{1}{a_2^2}$$

$$a_1 = 2 (k_o + \mu) (1 - z) / \mu z$$

$$a_2 = 111 / Z^{1/3} , \quad = C / Z^{1/3}$$

μ is the mass of the electron in MeV and Z is the atomic number of the bremsstrahlung radiator. The constant C in the formula for a_2 is the screening constant.

The integrated cross section is obtained as a function of k_o, and $\sigma(k)$ is derived by differentiation.

This method of unfolding bremsstrahlung yield curves was developed in this laboratory by Dr. D. W. Lang, who programmed the calculation for the electronic computer Silliac at the University of Sydney.

APPENDIX E

Gamma-ray Cascade in the Nucleus

These tables have been calculated by the method described in section 2.3, ch. 5. They give $P(J_f)$, the probability distribution of the spins J_f after a cascade beginning on a level with spin J_i, for n = 1, 2, 3 and 4 steps in the cascade.

They are used as follows. The competing spins are first decided; say they are 1 and 5. The spin distribution is assumed to split midway between them, so that half the levels with $J_f = 3$ and all with $J_f > 3$ will decay to the J = 5 level. The fraction which do this after n = 1, 2, 3 or 4 steps is obtained from the table for $J_i = 0$, say. These fractions are then averaged over the calculated distribution of n (e.g. Table 2, ch. 5). A further weighted average is then formed over $P(J_i)$ (see section 2.5).

The tables for integral J are carried to higher values as the target nucleus may already have a high spin.

$P(J_f)$ as a function of σ, J_i and n

$\sigma = 2$

J_i	n \ J_f	0	1	2	3	4	5	6
0	1	0	1.00					
	2	0.18	0.41	0.41				
	3	0.07	0.50	0.33	0.10			
	4	0.09	0.40	0.38	0.12	0.02		
1	1	0.18	0.41	0.41				
	2	0.07	0.50	0.33	0.10			
	3	0.09	0.40	0.38	0.12	0.01		
	4	0.07	0.39	0.37	0.15	0.02		
2	1		0.37	0.38	0.25			
	2	0.07	0.29	0.42	0.18	0.04		
	3	0.05	0.34	0.37	0.19	0.04	0.01	
	4	0.06	0.33	0.38	0.18	0.04	0.01	
3	1			0.51	0.33	0.16		
	2		0.19	0.36	0.34	0.10	0.02	
	3	0.03	0.21	0.39	0.26	0.10	0.01	
	4	0.04	0.26	0.37	0.24	0.08	0.01	
4	1				0.61	0.29	0.10	
	2			0.31	0.38	0.26	0.05	
	3		0.11	0.31	0.36	0.17	0.05	
	4	0.02	0.16	0.35	0.30	0.14	0.03	
5	1					0.71	0.24	0.05
	2				0.43	0.38	0.17	0.02
	3			0.22	0.38	0.30	0.09	0.01
	4		0.08	0.27	0.36	0.22	0.06	0.01
6	1						0.83	0.17
	2					0.60	0.34	0.07
	3				0.36	0.41	0.20	0.03
	4			0.18	0.37	0.32	0.11	0.01

$\sigma = 3$

J_i	n \ J_f	0	1	2	3	4	5	6	7	8
0	1	0	1.00							
	2	0.14	0.37	0.49						
	3	0.05	0.41	0.36	0.18					
	4	0.06	0.30	0.40	0.19	0.05				
1	1	0.14	0.37	0.49						
	2	0.05	0.41	0.36	0.18					
	3	0.06	0.30	0.40	0.19	0.05				
	4	0.04	0.28	0.36	0.24	0.07	0.01			
2	1		0.27	0.36	0.37					
	2	0.04	0.20	0.39	0.26	0.11				
	3	0.03	0.22	0.33	0.28	0.11	0.03			
	4	0.03	0.20	0.33	0.27	0.13	0.04			
3	1			0.35	0.36	0.29				
	2		0.10	0.25	0.38	0.20	0.07			
	3	0.01	0.10	0.27	0.32	0.21	0.07	0.02		
	4	0.01	0.13	0.26	0.30	0.20	0.08	0.02		
4	1				0.42	0.34	0.24			
	2			0.15	0.29	0.35	0.16	0.05		
	3		0.04	0.16	0.30	0.28	0.16	0.05	0.01	
	4	0.01	0.06	0.18	0.29	0.26	0.14	0.05	0.01	
5	1					0.47	0.33	0.20		
	2				0.19	0.32	0.33	0.13	0.03	
	3			0.07	0.20	0.32	0.25	0.13	0.03	
	4		0.02	0.09	0.22	0.28	0.23	0.11	0.03	
6	1						0.52	0.32	0.16	
	2					0.24	0.34	0.30	0.10	0.02
	3				0.10	0.24	0.32	0.22	0.09	0.02
	4			0.04	0.14	0.26	0.28	0.19	0.08	0.02

$\sigma = 4$

J_i	n \ J_f	0	1	2	3	4	5	6	7	8	9
0	1		1.00								
	2	0.13	0.35	0.52							
	3	0.04	0.38	0.37	0.21						
	4	0.05	0.26	0.39	0.23	0.07					
1	1	0.13	0.35	0.52							
	2	0.04	0.38	0.37	0.21						
	3	0.05	0.26	0.39	0.23	0.07					
	4	0.03	0.24	0.34	0.26	0.11	0.02				
2	1		0.24	0.35	0.41						
	2	0.03	0.17	0.37	0.29	0.14					
	3	0.02	0.18	0.31	0.30	0.15	0.04				
	4	0.02	0.16	0.29	0.28	0.18	0.06	0.01			
3	1			0.30	0.35	0.35					
	2		0.07	0.21	0.37	0.24	0.11				
	3	0.01	0.07	0.22	0.30	0.26	0.11	0.03			
	4	0.01	0.09	0.21	0.28	0.24	0.13	0.04			
4	1				0.35	0.35	0.30				
	2			0.10	0.24	0.36	0.21	0.09			
	3		0.02	0.11	0.25	0.29	0.22	0.09	0.02		
	4		0.04	0.13	0.23	0.27	0.20	0.10	0.03		
5	1					0.38	0.34	0.28			
	2				0.13	0.26	0.35	0.19	0.07		
	3			0.04	0.14	0.27	0.28	0.19	0.07	0.01	
	4		0.01	0.06	0.16	0.25	0.25	0.17	0.08	0.02	
6	1						0.41	0.34	0.25		
	2					0.16	0.28	0.34	0.17	0.06	
	3				0.06	0.16	0.28	0.26	0.17	0.06	0.01
	4			0.02	0.08	0.18	0.25	0.24	0.15	0.06	0.02

$\sigma = 5$

J_i	n \ J_f	0	1	2	3	4	5	6	7	8	9
0	1	0	1.00								
	2	0.12	0.35	0.53							
	3	0.04	0.36	0.37	0.23						
	4	0.04	0.25	0.38	0.24	0.09					
1	1	0.12	0.35	0.53							
	2	0.04	0.36	0.37	0.23						
	3	0.04	0.25	0.38	0.24	0.09					
	4	0.03	0.22	0.33	0.27	0.12	0.03				
2	1		0.23	0.34	0.43						
	2	0.03	0.16	0.36	0.29	0.16					
	3	0.02	0.16	0.29	0.31	0.17	0.06				
	4	0.02	0.14	0.27	0.28	0.19	0.08	0.02			
3	1			0.28	0.34	0.38					
	2		0.06	0.19	0.36	0.26	0.13				
	3	0.01	0.06	0.20	0.29	0.27	0.13	0.04			
	4	0.01	0.07	0.18	0.27	0.25	0.15	0.06	0.01		
4	1				0.31	0.34	0.35				
	2			0.09	0.21	0.35	0.24	0.11			
	3		0.02	0.09	0.22	0.28	0.24	0.11	0.03		
	4		0.03	0.10	0.20	0.26	0.22	0.13	0.04	0.01	
5	1					0.34	0.34	0.32			
	2				0.11	0.23	0.35	0.22	0.09		
	3			0.03	0.11	0.24	0.28	0.22	0.10	0.02	
	4			0.04	0.12	0.22	0.26	0.20	0.11	0.03	0.01
6	1						0.37	0.34	0.29		
	2					0.12	0.25	0.35	0.20	0.08	
	3				0.04	0.13	0.26	0.27	0.20	0.08	0.02
	4			0.01	0.05	0.15	0.23	0.25	0.18	0.09	0.04

$\sigma = \infty$

J_i	n \ J_f	0	1	2	3	4	5	6	7	8	9
0	1	0	1.00								
	2	0.11	0.33	0.56							
	3	0.04	0.33	0.37	0.26						
	4	0.04	0.22	0.37	0.26	0.11					
1	1	0.11	0.33	0.56							
	2	0.04	0.33	0.37	0.26						
	3	0.04	0.22	0.37	0.26	0.11					
	4	0.02	0.19	0.31	0.29	0.15	0.04				
2	1		0.20	0.33	0.47						
	2	0.02	0.14	0.33	0.31	0.20					
	3	0.02	0.13	0.26	0.31	0.20	0.08				
	4	0.02	0.11	0.23	0.28	0.22	0.11	0.03			
3	1			0.24	0.33	0.43					
	2		0.05	0.16	0.33	0.29	0.17				
	3		0.05	0.16	0.26	0.29	0.17	0.07			
	4	0.01	0.05	0.14	0.23	0.26	0.19	0.09	0.03		
4	1				0.26	0.33	0.41				
	2			0.06	0.17	0.33	0.27	0.16			
	3			0.06	0.17	0.26	0.27	0.16	0.06		
	4			0.07	0.15	0.24	0.24	0.18	0.08	0.02	
5	1					0.27	0.34	0.39			
	2				0.07	0.18	0.33	0.26	0.15		
	3			0.02	0.07	0.18	0.26	0.26	0.15	0.06	
	4			0.02	0.08	0.16	0.24	0.23	0.17	0.08	0.02
6	1						0.28	0.33	0.39		
	2					0.08	0.19	0.33	0.26	0.14	
	3				0.02	0.08	0.19	0.26	0.26	0.15	0.05
	4				0.03	0.09	0.17	0.23	0.23	0.16	0.09

$\sigma = 2$

J_i	n \ J_f	1/2	3/2	5/2	7/2	9/2	11/2	13/2	15/2
1/2	1	0.43	0.57						
	2	0.36	0.47	0.17					
	3	0.30	0.47	0.20	0.03				
	4	0.27	0.44	0.23	0.06				
3/2	1	0.30	0.40	0.30					
	2	0.25	0.47	0.22	0.06				
	3	0.25	0.43	0.25	0.06	0.01			
	4	0.24	0.42	0.25	0.08	0.01			
5/2	1		0.46	0.34	0.20				
	2	0.14	0.34	0.36	0.13	0.03			
	3	0.16	0.38	0.30	0.13	0.03			
	4	0.18	0.38	0.29	0.12	0.03			
7/2	1			0.54	0.32	0.14			
	2		0.25	0.36	0.30	0.09			
	3	0.08	0.26	0.36	0.22	0.08			
	4	0.11	0.31	0.33	0.19	0.06			
9/2	1				0.65	0.29	0.06		
	2			0.35	0.39	0.23	0.03		
	3		0.16	0.33	0.34	0.15	0.02		
	4	0.02	0.20	0.31	0.33	0.13	0.01		

$\sigma = 3$

J_i	n \ J_f	1/2	3/2	5/2	7/2	9/2	11/2	13/2	15/2
1/2	1	0.39	0.61						
	2	0.29	0.45	0.26					
	3	0.22	0.42	0.28	0.08				
	4	0.18	0.37	0.31	0.12	0.02			
3/2	1	0.23	0.35	0.42					
	2	0.17	0.39	0.30	0.14				
	3	0.15	0.33	0.33	0.15	0.04			
	4	0.14	0.31	0.32	0.17	0.06			
5/2	1		0.30	0.37	0.33				
	2	0.07	0.22	0.39	0.25	0.07			
	3	0.08	0.24	0.33	0.25	0.09	0.01		
	4	0.08	0.23	0.32	0.23	0.11	0.03		
7/2	1			0.39	0.35	0.26			
	2		0.12	0.28	0.36	0.18	0.06		
	3	0.03	0.13	0.29	0.30	0.18	0.06	0.01	
	4	0.04	0.15	0.28	0.28	0.17	0.06	0.02	
9/2	1				0.44	0.34	0.22		
	2			0.17	0.31	0.34	0.14	0.04	
	3		0.05	0.18	0.31	0.27	0.14	0.04	0.01
	4		0.06	0.19	0.30	0.25	0.13	0.04	0.02

$\sigma = 4$

J_i	n \ J_f	1/2	3/2	5/2	7/2	9/2	11/2	13/2	15/2
1/2	1	0.36	0.64						
	2	0.26	0.45	0.29					
	3	0.19	0.40	0.30	0.11				
	4	0.15	0.34	0.32	0.16	0.03			
3/2	1	0.20	0.35	0.45					
	2	0.14	0.37	0.32	0.17				
	3	0.13	0.30	0.33	0.18	0.06			
	4	0.11	0.28	0.31	0.21	0.08	0.01		
5/2	1		0.27	0.35	0.38				
	2	0.05	0.19	0.36	0.27	0.13			
	3	0.06	0.20	0.30	0.28	0.13	0.03		
	4	0.06	0.19	0.28	0.26	0.15	0.05	0.01	
7/2	1			0.32	0.35	0.33			
	2		0.09	0.22	0.37	0.23	0.09		
	3	0.02	0.09	0.23	0.30	0.24	0.10	0.02	
	4	0.02	0.11	0.22	0.28	0.22	0.11	0.04	
9/2	1				0.37	0.34	0.29		
	2			0.12	0.26	0.35	0.20	0.07	
	3		0.03	0.12	0.27	0.28	0.20	0.08	0.02
	4		0.04	0.12	0.26	0.26	0.22	0.08	0.02

$\sigma = 5$

J_i	n \ J_f	1/2	3/2	5/2	7/2	9/2	11/2	13/2	15/2
1/2	1	0.35	0.65						
	2	0.25	0.45	0.30					
	3	0.17	0.39	0.32	0.12				
	4	0.13	0.33	0.33	0.17	0.04			
3/2	1	0.19	0.35	0.46					
	2	0.13	0.36	0.32	0.19				
	3	0.11	0.29	0.34	0.19	0.07			
	4	0.10	0.26	0.31	0.22	0.09	0.02		
5/2	1		0.26	0.35	0.40				
	2	0.05	0.17	0.36	0.27	0.15			
	3	0.05	0.18	0.29	0.28	0.15	0.05		
	4	0.05	0.17	0.27	0.26	0.17	0.07	0.01	
7/2	1			0.29	0.34	0.37			
	2		0.08	0.20	0.35	0.25	0.12		
	3	0.01	0.08	0.21	0.28	0.26	0.12	0.04	
	4	0.02	0.09	0.19	0.26	0.24	0.14	0.05	0.01
9/2	1				0.32	0.35	0.33		
	2			0.09	0.22	0.36	0.23	0.10	
	3		0.02	0.10	0.23	0.29	0.23	0.10	0.03
	4		0.03	0.11	0.23	0.27	0.21	0.11	0.04

$\sigma = \infty$

J_i	n \ J_f	1/2	3/2	5/2	7/2	9/2	11/2	13/2	15/2
1/2	1	0.33	0.67						
	2	0.22	0.45	0.33					
	3	0.15	0.37	0.33	0.15				
	4	0.11	0.30	0.33	0.20	0.06			
3/2	1	0.17	0.33	0.50					
	2	0.11	0.33	0.34	0.02				
	3	0.09	0.26	0.34	0.22	0.09			
	4	0.07	0.22	0.30	0.25	0.12	0.04		
5/2	1		0.22	0.33	0.45				
	2	0.04	0.15	0.33	0.30	0.18			
	3	0.04	0.15	0.26	0.30	0.18	0.07		
	4	0.04	0.13	0.23	0.26	0.21	0.10	0.03	
7/2	1			0.25	0.33	0.42			
	2		0.05	0.17	0.33	0.28	0.17		
	3	0.01	0.05	0.17	0.26	0.28	0.17	0.06	
	4	0.01	0.06	0.15	0.23	0.25	0.19	0.09	0.02
9/2	1				0.27	0.33	0.40		
	2			0.07	0.18	0.33	0.27	0.15	
	3		0.02	0.07	0.18	0.26	0.27	0.16	0.06
	4		0.02	0.08	0.15	0.24	0.28	0.17	0.06

REFERENCES

As 60	R. F. Askew and A. P. Batson	Nucl. Phys. 20, 408, 1960
Au 59	L. B. Aull, G. C. Reinhardt and W. D. Whitehead	Nucl. Phys. 13 292, 1959
Ba 53	R. G. Baker and L. Katz	Nucleonics 11, No. 2, 14, 1953
Ba 60	W. C. Barber and V. J. Vanhuyse	Nucl. Phys. 16, 381, 1960
Be 54	A. I. Berman and K. L. Brown	Phys. Rev. 96, 83, 1954
Bl 52	J. M. Blatt and V. F. Weisskopf	"Theoretical Nuclear Physics", 1952
Bl 54	C. Bloch	Phys. Rev. 93, 1094, 1954
Bo 53	A. Bohr and B. R. Mottelson	Mat.Fys.Medd.Dan.Vid. Selsk. 27, No. 16, 1953
Br 57	D. M. Brink	Nucl. Phys. 4, 215, 1957
Br 58	G. E. Brown and J. S. Levinger	Proc. Phys. Soc. A71 733, 1958
Br 59	G. E. Brown and M. Bolsterli	Phys. Rev. Letters 3, 472, 1959
Br 60	K. A. Brueckner and R. Thieberger	Phys. Rev. Letters 4, 466, 1960
Br 60a	G. E. Brown and D. J. Thouless	Physica 26, Supplement, S145, 1960
Br 61	W. Brenig	Nucl. Phys. 22, 14, 1961
Br 61a	G. E. Brown, L. Castillejo and J. A. Evans	Nucl. Phys. 22, 1, 1961
By 51	P. R. Byerly and W. E. Stephens	Phys. Rev. 83, 54, 1951
Ca 53	J. G. Campbell and A. J. F. Boyle	Aust. J. Phys. 6, 171, 1953
Ca 54	J. H. Carver and E. Kondaiah	Phil. Mag. 45, 988, 1954
Ca 58	J. H. Carver and W. Turchinetz	Proc. Phys. Soc. A71, 613, 1958
Ca 58a	J. H. Carver and W. Turchinetz	Proc. Phys. Soc. A73, 69, 1959
Ca 59	J. H. Carver and W. Turchinetz	Proc. Phys. Soc. A73, 110, 1959
Ca 59a	J. H. Carver and W. Turchinetz	Proc. Phys. Soc. A73, 585, 1959

Ca 60	J. H. Carver and D. C. Peaslee	Phys. Rev. 120, 2155, 1960
Ca 60a	E. E. Carroll and W. E. Stephens	Phys. Rev. 118, 1256, 1960
Ca 60b	J. H. Carver and G. A. Jones	Nucl. Phys. 19, 184, 1960
Ca 60c	J. H. Carver	Proc. Phys. Soc. 77, 417, 1961
Ca 61	J. H. Carver, D. C. Peaslee and R. B. Taylor	Phys. Rev. (to be published)
Cl 61	J. W. Clark	Can. J. Phys. 39, 385, 1961
Co 59	C. S. Cook	Nucl. Instr. 4, 103, 1959
Co 60	B. L. Cohen and R. E. Price	Nucl. Phys. 17, 129, 1960
Da 58	M. Danos	Nucl. Phys. 5, 23, 1958
De 50	S. Devons and G. R. Lindsay	Proc. Phys. Soc. A63, 1202, 1950
Di 50	B. C. Diven and C. M. Almy	Phys. Rev. 80, 407, 1950
Do 59	A. C. Douglas and N. Macdonald	Nucl. Phys. 13, 382, 1959
Du 59	J. Dular et al.	Nucl. Phys. 14, 131, 1959
El 57	J. P. Elliott and B. H. Flowers	Proc. Phys. Soc. A242, 57, 1957
Er 58	T. Ericson and V. M. Scrutinski	Nucl. Phys. 8, 284, 1958
Er 59	T. Ericson	Nucl. Phys. 11, 481, 1959
Er 60	T. Ericson	Adv. Phys. 9, 425, 1960
Er 60a	T. Ericson	Proc.Int.Conf.Nucl. Structure 1960, P.697
Fe 51	B. T. Feld et al.	NYO-636, 1951
Fe 59	F. Ferrero et al.	Nucl. Phys. 10, 423, 1959
Fl 52	B. H. Flowers, J. D. Lawson and E. B. Fossey	Proc. Phys. Soc. B65, 286, 1952
Fu 56	J. Fujita	Prog. Theor. Phys. 16, 112, 1956
Fu 58	E. G. Fuller and M. S. Weiss	Phys. Rev. 112, 560, 1958

Fu 60	E. G. Fuller and E. Hayward	Proc.Inst.Conf.Nucl. Structure 1960, P.760
Fu 61	E. G. Fuller and E. Hayward	To be published in "Nucl. Reactions" Vol.II
Ga 57	B. I. Gravrilov and L. E. Lazareva	Soviet Physics J.E.T.P. 3, 871, 1957
Ga 60	S. B. Garfinkel, private communication from the National Bureau of Standards, Washington	
Ge 54	M. Gell Mann, M. L. Goldberger and W. E. Thirring	Phys. Rev. 95, 1612, 1954
Gl 52	H. Glattli, O. Seippel and P. Stoll	Helv. Phys. Acta 25, 491, 1952
Go 48	M. Goldhaber and E. Teller	Phys. Rev. 74, 1046, 1948
Go 53	J. Goldemberg and L. Katz	Phys. Rev. 90, 308, 1953
Go 55	H. E. Gove and E. Paul	Phys. Rev. 97, 104, 1955
Gr 36	L. H. Gray	Proc. Roy. Soc. A 156, 578, 1936
Gr 57	G. W. Grodstein	Nat. Bur. Stds. Circular 583, 1957
Ha 52	J. A. Halpern, A. K. Mann and R. Nathans	Rev. Sci. Instr. 23, 678, 1952
Ha 56	W. H. Hartley, W. E. Stephens and E. J. Winhold	Phys. Rev. 104, 178, 1956
Ha 61	R. N. H. Haslam	Private communication, 1961
He 58	R. A. Heferlin and W. Kreger	Nucl. Instr. 3, 149, 1958
Hi 47	O. Hirzel and H. Wäffler	Helv. Phys. Acta. 20, 373, 1947
Hi 59	C. T. Hibdon	Phys. Rev. 114, 179, 1959
Hi 61	C. T. Hibdon	Phys. Rev. 122, 1235, 1961
Ho 50	P. V. C. Hough	Phys. Rev. 80, 1069, 1950
Hu 60	J. R. Huizenga and R. Vandenbosch	Phys. Rev. 120, 1305, 1960
Je 52	J. H. Jensen and J. M. Luttinger	Phys. Rev. 86, 907, 1952
Jo 50	H. E. Johns, L. Katz, R. A. Douglas and R. N. H. Haslam	Phys. Rev. 80, 1062 1950
Ka 51	L. Katz and A. G. W. Cameron	Can. J. Phys. 29, 518, 1951

Ka 52	L. Katz, L. Pease and H. Moody	Can. J. Phys. 30, 476, 1952
Ka 53	L. Katz, R. G. Baker and R. Montalbetti	Can. J. Phys. 31, 250, 1953
Ka 59	M. Kawai and T. Terasawa	Prog. Theor. Phys. 22, 513, 1959
Ka 60	L. Katz	Proc.Int.Conf. Nucl. Structure 1960, P.710
Ka 60a	T. M. Kavanagh	Can. J. Phys. 38, 1438, 1960
Ki 59	H. King and L. Katz	Can. J. Phys. 37, 1357, 1959
Ki 60	J. D. King, R. N. H. Haslam and R. W. Parsons	Can. J. Phys. 38, 231, 1960
Ko 56	H. W. Koch and J. M. Wyckoff	J.Res.Nat.Bur.Stds. 56, 319, 1956
Ko 58	H. W. Koch and J. M. Wyckoff	I.R.E. Trans. Nucl. Sci. NS-5, 127, 1958
Ko 59	J. Kockum and N. Starfelt	Nucl. Instr. 4, 171, 1959
Ko 59a	J. Kockum and N. Starfelt	Nucl. Instr. 5, 37, 1959
Kr 52	V. F. Krohn and E. F. Shrader	Phys. Rev. 87, 685, 1952
Kr 58	S. P. Kruglov	Sov. Phys. J.E.T.P. 6, 817, 1958
La 54	J. M. B. Lang and K. J. Le Couteur	Proc. Phys. Soc. A67 585, 1954
La 59	D. W. Lang and K. J. Le Couteur	Nucl. Phys. 14, 21, 1959
La 61	D. W. Lang	Nucl. Phys. (to be published)
Le 50	J. S. Levinger and H. A. Bethe	Phys. Rev. 78, 115, 1950
Le 59	K. J. Le Couteur	in "Nuclear Reactions" Vol. I, 1959
Le 60	J. S. Levinger	"Nuclear Photodisintegration", 1960
Ma 54	G. G. Manov	Ann. Revs. Nucl. Sci. 4, 1954
Ma 57	R. L. Mather	J. Appl. Phys. 28, 1200, 1957
Ma 60	B. Mainsbridge	Aust. J. Phys. 13, 204, 1960
Mc 50	B. D. McDaniel, R. L. Walker and M. B. Stearns	Phys. Rev. 80, 807, 1950
Mi 58	W. F. Miller, J. Reynolds and W. J. Snow	ANL - 5902, 1958
Mi 61	W. F. Miller and W. J. Snow	ANL - 6318, 1961

Mo 53	R. Montalbetti, L. Katz and J. Goldemberg	Phys. Rev. 91, 659, 1953
Mu 50	C. O. Muehlhause	Phys. Rev. 79, 277, 1950
Mu 59	N. Mutsuro et al.	J. Phys. Soc. Japan 14, 1457, 1959
Na 59	T. Nakamura et al.	J. Phys. Soc. Japan 14, 693, 1959
Na 61	I. C. Nascimento, G. Moscati and J. Goldemberg	Nucl. Phys. 22, 484, 1961
N.D.S.	59, 60 Nuclear Data Sheets, 1959 and 1960	
Ne 56	T. D. Newton	Can. J. Phys. 34, 804, 1956
Ne 61	V. G. Neudachin, V. G. Shevchenko and N. P. Yudin	Sov. Phys. J.E.T.P. 12, 79, 1961
Ok 58	K. Okamoto	Phys. Rev. 110, 143, 1958
Pe 57	D. H. Perkel	Nucleonics 15, No. 6, 103, 1957
Pe 58	A. S. Penfold and J. E. Leiss	University of Illinois Report, 1958
Pe 61	D. C. Peaslee	Phys. Rev. (to be published)
Ri 60	R. A. Ricci, R. Van Lieshout and H. J. Van Den Bold	Physica 26, 1014, 1960
Ro 58	M. E. Rose	"Internal Conversion Coefficients" 1958
Ro 59	J. P. Roalsvig, R. N. H. Haslam and D. J. McKenzie	Can. J. Phys. 37, 607 1959
Ro 60	J. P. Roalsvig, R. N. H. Haslam and J. Bergsteinsson	Can. J. Phys. 38, 320, 1960
Ro 60a	R. L. Robinson, F. K. McGowan and W. G. Smith	Phys. Rev. 119, 1692, 1960
Ry 58	T. W. Rybka and L. Katz	Phys. Rev. 110, 1123, 1958
Sc 46	L. I. Schiff	Phys. Rev. 70, 87, 1946
Sc 51	L. I. Schiff	Phys. Rev. 83, 252, 1951
Sc 55	M. B. Scott, A. O. Hanson and D. W. Kerst	Phys. Rev. 100, 209, 1955
Sc 59	J. P. Schiffer, L. L. Lee and B. Zeidman	Phys. Rev. 115, 427, 1959
Se 60	F. D. Seward, S. C. Fultz, C. P. Jupiter and R. E. Shafer	UCRL - 6177, 1960
Sh 49	S. Shimizu	Mem.Coll.Sci.Kyoto, A25, 193, 1949

SHS 58	D. Strominger, J. M. Hollander and G. T. Seaborg	Revs. Mod. Phys. 30, 585, 1958
Si 56	E. Silva and J. Goldemberg	An. Acad. Brasil. Cience. 28, 275, 1956
Si 58	E. Silva, J. Goldemberg and P. B. Smith	Nuovo Cim. 9, 17, 1958
Sp 58	B. M. Spicer	Aust. J. Phys. 11, 490, 1958
St 50	H. Steinwedel and J. H. Jensen	Z. Naturforsch, 5a, 413, 1950
St 51	M. B. Stearns and B. D. McDaniel	Phys. Rev. 82, 450, 1951
St 58	E. Storm, E. Gilbert and H. Israel	LA - 2237, 1958
Ta 59	N. W. Tanner, G. C. Thomas and W. E. Meyerhof	Nuovo Cim. 14, 257, 1959
Ta 60	R. B. Taylor	Nucl. Phys. 19, 453, 1960
Th 60	H. H. Thies and B. M. Spicer	Aust. J. Phys. 13, 505, 1960
Th 61	I. M. Thorson and L. Katz	Proc. Phys. Soc. A77, 166, 1961
To 57	F. M. Tomnovec and R. L. Mather	J. Appl. Phys. 28, 1208, 1957
Tr 61	E. S. Troubetzkoy	Phys. Rev. 122, 212, 1961
Va 60	R. Vandenbosch and J. R. Huizenga	Phys. Rev. 120, 1313, 1960
Ve 58	S. H. Vegors, L. L. Marsden and R. L. Heath	I.D.O. - 16370, 1958
Wa 48	H. Wäffler and O. Hirzel	Helv. Phys. Acta. 21, 200, 1948
Wa 58	A. H. Wapstra	Handbuch der Physik, Vol. 38/1. 1958
We 61	E. Weigold and R. N. Glover	Nucl. Phys. (to be published)
Wi 53	R. R. Wilson	Proc. Phys. Soc. A66, 638, 1953
Wi 56	D. H. Wilkinson	Physica 22, 1039, 1956
Wi 58	D. H. Wilkinson	Phil. Mag. 3, No. 30, 567, 1958
Wi 59	D. H. Wilkinson	Ann. Revs. Nucl. Sci. 9, 1959
Ya 60	S. Yasumi et al.	J. Phys. Soc. Japan 15, 1913, 1960
Ye 56	P. F. Yergin and B. F. Fabricand	Phys. Rev. 104, 1334, 1956
Zi 60	B. Ziegler	Nucl. Phys. 17, 238, 1960